Experimental and theoretical analysis of polarization-maintaining fibre for sensing applications

By:

Mohammad Karimi

Thesis submitted for the degree of Doctor of Philosophy

City University
School of Engineering and Mathematical Sciences
London EC1V 0HB

September 2014

TABLE OF CONTENTS

List of Figures iv

List of Tables vii

List of Abbreviations viii

List of Symbols ix

Acknowledgements x

Abstract 1

CHAPTER 1 3

1.1 Introduction 4
1.2 Motivation 4
1.3 Aims and objectives of the work 7
1.4 Structure of the thesis 7

Chapter 2 9

2.1 Introduction 10
2.2 Conventional pressure sensors 12
2.2.1 Liquid manometer 12
2.2.2 Mechanical pressure gauges and pressure transducers manometer 12
2.2.3 Electrochemical transducers 14
2.2.4 Piezoresistive transducers 16
2.2.5 Piezoelectric transducers 17
2.3 Fibre optic pressure sensors 18
2.3.1 Introduction 18
2.3.2 Advantage and disadvantages of optical fibre pressure sensors 21
2.3.3 Review of optical pressure sensor technologies 22
2.3.3.1 Introduction 22
2.3.3.2 Intensity-Modulated pressure sensors 23
Phase Modulated pressure sensors 30
2.3.3.3 Wavelength Modulation Sensors 39
2.3.3.4 Polarization & refractive index sensors 45
2.4 Summary 47

CHAPTER 3 48

3.1 Introduction 49
3.2 Light propagation 49
3.3 Light propagating in optical fibres 54

3.4 Modes of optical fibres 56
3.5 Birefringence 57
3.6 Analysis of the birefringence in a non-symmetric side-hole fibre with one hole 60
3.7 Mode coupling in Hi-Bi fibres 72
3.8 Lateral pressure effect on Hi-Bi fibres 76
3.9 Evaluation of a high birefringence single mode optical fibre as a pressure sensor 79
3.10 Summary 84

CHAPTER 4 86

4.1 Transverse force sensitivity of one and two side hole(s) fibres 87
4.1.1 Sensor configuration 88
4.1.2 Evaluation of the side-hole fibre-based sensor performance 91
4.2 Transverse force sensitivity of photonic crystal fibres 94
4.2.1 Sensor fabrication 96
4.2.2 Sensor configuration 97
4.2.3 Evaluation of the PCF-based sensor performance 99
4.3 Transverse force sensitivity of Joint PCFs 106
4.3.1 Sensor configuration 109
4.3.2 Evaluation of the joint PCF-based sensor performance 111
4.4 Summary 113

Chapter 5 115

5.1 Introduction 116
5.2 Principle, fabrication and instrumentation 117
5.3 Accelerated corrosion tests 119
5.4 Results and discussion 121
5.5 Summary 124

CHAPTER 6 125

6.1 Summary and Conclusions 126
6.2 Future work 127

References 129

Publications 150

List of Figures

Figure 1.1 The value of fibre-optic sensor systems will grow at an average annual rate of 20.5%.[2] .. 5
Figure 2.1 Mercury-filled U-shaped sensor for measuring gas pressure [9]. 12
Figure 2.2 Elastic pressure-sensing elements.[9] 13
Figure 2.3 Potentiometer pressure transducer [27] 15
Figure 2.4 Pressure transducer that uses a Bourdon tube as sensing element and LVDT [26]. 15
Figure 2.5 Capacitive pressure transducer [25] 16
Figure 2.6 Structure of a semiconductor pressure sensor [38] 17
Figure 2.7 Piezoelectric pressure transducer using a diaphragm as a force-summing device (a) Schematic of pressure transducer (b) incorporating the diaphragm in the housing [42] 18
Figure 2.8 Transmissive fibre optic pressure sensor using a shutter to modulate the intensity [98]. 24
Figure 2.9 Transmissive fibre optic pressure sensor using a moving grating to modulate the intensity [98] 25
Figure 2.10. Schematic of an intensity based sensor system with a transmission gap [102] 25
Figure 2.11 Illustration of a fiber optic intensity sensor for distance measurements. (a) Two-fiber sensor, showing the object and the operational principle (b) Various geometries for fiber bundle sensor heads, [106] 26
Figure 2.12 shows the detected light intensity versus distance from the target [100]. 26
Figure 2.13 Frustrated-total-internal-reflection mode sensor [109] 27
Figure 2.14. Fibre optic microbend pressure sensor 28
Figure 2.15 Evanescent coupler sensor [128] 29
Figure 2.16. Schematic of Mach Zehnder pressure sensor [137] 31
Figure 2.17. Configuration of various types of MZIs; the methods of using (a) a pair of LPGs, (b) core mismatch, (c) air-hole collapsing of PCF, (d) MMF segment, (e) small core SMF, and (f) fibre tapering.[153] 32
Figure 2.18. (a) Basic configuration of a Michelson interferometer and (b) schematic of an in-line Michelson interferometer. [155] 33
Figure 2.19. Schematic of a sensor based on a Sagnac interferometer. [162] 34
Figure 2.20. Fabry-Perot configuration 36
Figure. 2.21: Schematic description of the F-P absolute measurement signal conditioner from FISO Technologies using patented white-light interferometry (left) and detail of F-P sensing interferometer showing ray traces obtained from a selected incident angle light beam propagating in the optical fibre core (right).[77] 37
Figure 2.21 Intrinsic Fabry-Perot Interferometer Sensors [178] 38
Figure 2.22. Extrinsic Fabry-Perot Interferometer Sensor; a) reflective diaphragm sensor; b) transparent sensor; c) two opposite fibres sensor; and d) hollow core fibre sensor [178] 39
Figure 2.23. Bragg grating schematic and its response to a broadband wavelength source. 41
Figure 2.24 Schematic diagram of FBG (a) hydrostatic and (b) transvers pressure sensor.[206] 42
Figure 2.25 Schematic diagram of FBG-based pressure sensors.[61] 42
Figure 2.26. Schematic diagram of FBG-based pressure sensors mounted on a cylinder. [209] 43
Figure 2.27. An illustration of fluorescent light emission. 44
Figure 2.28 Fluorescent Decay-based Pressure Sensor [215] 45
Figure 2.29 Schematic diagram of a polarization modulation-based pressure sensor [220] 46
Figure 2.30 Fibre sensor using critical angle properties of a fibre for pressure measurement via measurements of the light reflected back into the fibre.[101] 47
Figure 3.1 Schematic diagram of wave propagation of electric and magnetic fields in z direction (they are not in scale) 52
Figure 3.2 polarization states described by equation (3.22) for various values of $\boldsymbol{\delta}$ *[227].* 53
Figure 3.6 schematical diagram of wave function components 55

Figure 3.7. Cross sections of conventional polarization maintaining fibres with (a) Elliptical Core;(b) Elliptical Cladding;(c) Elliptical Jacket; cross-sections of (d) bow-tie; (e) PANDA and (f) D-type [233]..... 58
Figure 3.8 Visual determination of the beat length, $\boldsymbol{LB}$, with the optical phase difference between the two orthogonal polarization states[233]. 59
Figure 3.9: One-hole PM fibre which has a core diameter 2a of 8.7 µm and hole diameter 2h of 30 µm. The distance between the right edge of the core to the left edge of the hole, d-a-h, is 9 µm..... 60
Figure 3.10. Radial stress distribution in one-hole fibre as a function of radial distance r; (a) radial stress distribution within the fibre cross-section with a hole, i.e. when θ varies from 0° to 30° (b) radial stress distribution within the fibre cross-section outside the hole region when θ varies from 30° to 90° 66
Figure 3.11. Circumferential stress distribution in a one-hole fibre as a function of radial distance. (a) circumferential stress distribution within the fibre cross-section with a hole, i.e. when θ varies from 0° to 30° (b) circumferential stress distribution within the fibre cross-section outside the hole region when θ varies from 33° to 90°..... 67
Figure 3.12 Expanded view of (a) Radial (b) Circumferential stress in core region of Figures 3.10 and 3.11..... 69
Figure 3.13.Stress distribution across the cladding..... 70
Figure 3.14.Stress distribution across the core..... 70
Figure 3.15.Birefringence distribution in a one-hole fibre core as a function of angles θ . (a) Edge of the core. (b) Cross section of the core 71
Figure 3.16 a non-symmetric side-hole fibre under pressure 77
Figure. 3.17 Schematic of the experimental setup used in this investigation. 80
Figure 3.18 Transmission spectra of the fibre when it is exposed to a different transverse force ranging from 0 to 10 N..... 83
Figure 3.19. Wavelength shifts from a base wavelength around 1550nm as a function of fibre length when a constant load is applied on to two different types of Hi-Bi PCF and Panda fibres with $\boldsymbol{B = 3.80 \times 10 - 4}$ and $\boldsymbol{B = 1.45 \times 10 - 3}$ respectively and the overall PM fibre length is varied from 0 to 5 m. The applied weight was 2N over a fibre length of 45 mm 84
Figure 4.1 (a) One-hole high-birefringence fibre that has a hole diameter of 30 μm and the distance between the right edge of the core to the left edge of the hole d d_1 is 9 μm. (b) Two-hole high-birefringence fibre that has two holes with the same diameter of 27 μm and the distance between the right edge of the core to the left edge of the hole on the right d_2 is 14 μm. 87
Figure 4.2 Schematic diagram of the experimental set-up of the PM fibre with force applied (θ) is the angle between the applied force and the slow axis x of the fibre) 89
Figure 4.3 Comparison of experimental and theoretical phase differences of the PM fibres when force is applied at different angles in relation to the slow axis of the(a) one-hole fibre, (b) two-hole fibre. 92
Figure 4.4: Sensitivity as a function of rotational angle for (a) one-hole and (b) two-hole fibres 94
Figure 4.5. Schematic of the experimental setup used in this investigation. PCF is the photonic crystal fibre used and PC is the polarization controller. SLED is the superluminescent LED source and OSA is the Optical Spectrum Analyzer used. The force, F, is applied as shown. 98
Figure 4.6 Experimental set-up for the evaluation of PCF-based pressure/force sensors..... 100
Figure 4.8 Wavelength shift versus fibre orientation (force direction) for angles from $\mathbf{0}$° to $\mathbf{180}$°. Points are obtained from the experimental work and the solid line results from the theoretical analysis 103
Figure 4.9. Wavelength shift versus fibre orientation (force direction) for angles from 0 to 180 deg for the four fibre types considered. 104
Figure 4.10. Wavelength shift versus external load for applied forces of up to 10 N, in steps of 1N for four different fibres (Type numbers shown and described in detail in the text) 105
Figure. 4.11. Interference pattern obtained using the OSA showing the effects seen from the Low birefringence PCF (Type 090329Pb) and the High Birefringence PCF (Type 070107P20), illustrating

the comparative wavelength spacing between the peaks. (In each case the vertical axis is an arbitrary intensity and the horizontal axis shows the wavelength range from 1450 to 1650 nm) 107
Figure 4.12: Interference pattern snapshots of (a) Low birefringence and (b) High Birefringence PCFs 108
Figure 4.13. Schematic of the experimental setup used in this investigation. PCF1 and PCF2 are photonic crystal fibres and PC1 and PC2 are polarization controllers. SLED is the superluminescent LED source and OSA is the Optical Spectrum Analyzer used. The force, F, is applied as shown. 109
Figure 4.14. Wavelength shift versus external load for different combinations of PCFs for forces (loads) up to 10 N. The direction of the load applied to each PCF fibre combination used corresponds to the maximum sensitivity, as shown in Fig. 2. (Fibre types making up the combinations are shown in the inset.)..... 111
Figure 4.15. Wavelength shift versus external load for different individual fibres shown: types 090329p, 070107p2, 391b3, 478b2 and the combination 478b2 and 090329p, for applied forces (loads) of up to 10N. The direction the load was applied on each PCF corresponds to the maximum sensitivity illustrated in Figure 4.13...... 112
Figure 5.1 Schematic of the alignment rig used in this paper...... 118
Figure 5.2 (a) Sensor alignment at a constant load of 5 N before mounting on the rebar. (b) Sensor response to 5 N after mounting to rebar. 118
Figure 5.3 (a) Instrumated rebar with unprotected sensor. (b) Instrumented rebar with sensor protected by a thin layer of silicone. 119
Figure 5.4 Accelerated corrosion test setup...... 120
Figure 5.5. Validation of sensing concept using the accelerated corrosion test (Rebar 1)...... 122
Figure 5.6. Behaviour of bare and silicone-protected PCFs under accelerated corrosion (Rebar 2). 122
Figure 5.7. Photo of corroding cylinder. 123

List of Tables

Table 4.1 Summary of fibres parameters 88
Table 4.2 Parameters of the photonic crystal fibres used in these experiments. In the table, MFD is the Mode Field Diameter, d the small hole diameter, D the large hole diameter in the case of the Hi-Bi fibre, Λ the distance between adjacent holes, B(1550) the birefringence at 1550 nm, and S the sensitivity around 1550 nm at the most-sensitive direction. 97
Table 4.3 shows the pictures of fusion splices of various types of PCFs to single mode fibres 99
Table 4.4 Experimental data showing the sensitivity dependence of PM fibres on the fibre length, with reference to the theoretical prediction 102
Table 4.5 Experimental data showing the sensitivity dependence of PM fibres on the fibre orientation, with reference to the theoretical prediction 103
Table 4.6 Experimental data showing the sensitivity dependence of PM fibres on the birefringence of the fibres, with reference to the theoretical prediction 105
Table 4.7summarizes the sensitivity of the fibres when they are joint together 113

List of Abbreviations

Compound Annual Growth Rate (CAGR)
Electromagnetic interference (EMI)
Fabry-Perot (FP)
Fibre Bragg Grating (FBG)
Fibre Loop Mirror (FLM)
Frustrated Total Internal Reflection (FTlR)
High Birefringence (Hi-Bi)
Linear Variable Differential Transformer (LVDT)
Long Period Grating (LPG)
Mach-Zehnder Interferometer (MZI),
Michelson Interferometer (MI)
Micro-Electro-Mechanical Systems (MEMs)
Mode Field Diameter (MFD)
Multimod Fibre (MMF)
Near Total Internal Reflection (NTIR)
Numerical aperture (NA)
Optical Fibre Sensors (OFSs)
Optical Spectrum Analyser (OSA).
Polarization Controller (PC)
Photonic Crystal Fibre (PCF)
Polarization maintaining (PM)
Sagnac Interferometer (SI)
Single Mode (SM)
State of polarization (SOP)
Structural health monitoring (SHM)
Super Light Emitted Diode (SLED)

List of Symbols

P	Pressure
F	Force
E	Electric field
D	Electric displacement
B	Magnetic induction
H	**M**agnetic field
ε	Dielectric permittivity
ε_0	Electric permittivity in vacuum
μ	Magnetic permeability
σ	Conductivity of the medium
ρ	Electric Charge density
J	Current density
ψ	Wave equation in three dimension
v	Light speed
k	Wave vector
r	Wavefront position
ω	Angular frequency
δ	Phase angles
n	Refractive index
υ	Azimuthal mode index
J_υ	First (ordinary) Bessel functions of the υ th order
K_υ	Second (hyperbolic or modified) Bessel functions of the υ th order
V	Normalized frequency
NA	Numerical aperture
B	Birefringent
n_s	Refractive index in slow axis
n_f	Refractive index in fast axis
L_B	Beat length
C	Stress-optic coefficient
σ_r	Stress components in radial axis (polar coordinates)
σ_θ	Stress components in polar coordinates
$\sigma_{r\theta}$	Shear stress
E	Young's modulus
υ	Poisson’s ratio
A	Airy stress function
φ	Thermo-elastic displacement potential
ξ	Sum of a total thermo-elastic displacement potential and Airy stress function
T	Glass melting temperature
α	Thermal expansion coefficient
$[\delta\varepsilon]$	Perturbation tensor
$[\varepsilon_i]$	Dielectric tensor
β	Propagation constant
F	Force
f	Force per meter
A	Jones matrices
I_0	Total electric intensity

Acknowledgements

I would like to express my sincere gratitude to Professors Tong Sun and Ken Grattan for their encouragement, support and enthusiasm over the past four years, the sincerest tanks for their excellent supervision, reviewing my academic publications, given invaluable feedback and for their help day by day throughout the whole period of this work.

Thanks are also due to Dr. Fredderic Surre for his help during the early stage of my work. Especial thanks are due to Dr. Matthias Fabian and Dr Martin Ams for their help during the field tests in the laboratory.

Thanks are particularly due to my fellow researchers, Jie Chao, Shuying Chen, Hien Nguyen, Tu Hu, Shanika Alwis, Nahid Roufi, and Kort Bremer for their suggestions, ideas, help and most importantly all the cheerful chat!

I also would like to say a special thanks to my parents who I am greatly indebted to them for all supporting.

Finally, I would like to say a very special thanks to my lovely wife Elham for being so supportive over the years and encouraging me to complete my PhD.

Abstract

Fibre optic sensors have been developed extensively over the past several decades, showing their potential and suitability for real-time measurement and thus meeting various industrial challenges. This has been achieved through the continuous innovation both in the fibre structural design and in the exploration of a variety of sensing mechanisms employed. Optical fibre sensors have shown advantages over conventional electrical counterparts by being of small size, immunity to electromagnetic interference and resistance to chemical attack, thus revealing their potential for a range of industrial applications. High-birefringence (Hi-Bi) optical fibres represent an important type of specialist fibres that have been explored widely by researchers. The focus of this thesis is to explore their potential for different sensing applications as the birefringence of these polarization maintaining (PM) fibres varies in response to the change in the surrounding environment, such as force and pressure.

Extensive evaluation of high-birefringence optical fibres, such as those with an elliptical core or elliptical inner cladding, Bow-Tie, Panda and Hi-Bi Photonic Crystal Fibres (PCFs), has been made both experimentally and theoretically, using numerical or analytical techniques.

In this thesis, the material birefringence of Polarization-Maintaining fibres, e.g. PM side hole fibre(s) with one or two hole(s) located in its cladding, is calculated using a thermo-elastic displacement potential method through the superposition of sectional displacement potentials. These PM fibres have shown the potential for pressure/force measurement based on their birefringence characteristics when exposed to a transverse force. The methodology used is generic and thus applicable to any one-hole fibre structures, should the hole diameter or position vary in the fibre cladding, or the fibre hole be empty or filled in with any material. This enables the analysis to be applied more widely in a range of optical fibre sensor applications.

Direct measurement of transverse force through the interrogation of induced birefringence variation has also been investigated in this thesis by using two specialist single mode Polarisation-Maintaining (PM) side-hole(s) fibres and four different types of Hi-Bi and low-Bi PCFs. The variation in the pressure sensitivity of these PM fibres has been investigated both theoretically and experimentally and it was confirmed that they are dependent upon several key parameters of the system, including the fibre structure, the magnitude and the direction of the applied external force, the fibre length used and the birefringence of the fibre. The theoretical data obtained have shown a good agreement with those from experiments, confirming the suitability of the use of such PM fibres for the measurement of pressure, force and mass of an object, applied in different directions, over a wide range and in real time.

It is concluded based on the theoretical and experimental data obtained that PCFs of low birefringence are more sensitive than those of high birefringence (Hi-Bi) although the former require a longer length to achieve a similar level of birefringence. Compared to conventional Hi-Bi fibres (e.g. Panda and Bow-Tie fibres), PCFs have demonstrated much lower temperature sensitivity and this suggests that they are well suited to measure pressure, force, and mass in real time when temperature varies by using a fibre loop mirror (FLM) configuration. To solve the length problem in the low birefringence PCFs, a joint PCF approach can be used by fusion-splicing a short length of Low-Bi with a short section of a Hi-Bi PCF and their sensitivity to lateral pressure has been investigated and reported in detail in this thesis.

CHAPTER 1

Introduction

1.1 Introduction

The world has benefited enormously from the advancement of both electronic and optical technologies, in particular in the development of electrical and optical sensors. Electrical sensors have shown some limitations in terms of ultimate speed of function and environmental impact on their performance. Optical technologies offer the capacity of faster speeds and the ability to operate under harsher conditions with a higher sensitivity [1].

Fibre Optic Sensor (FOS) technologies have been widely applied in optical devices and systems, have found extensive implementation in telecommunications, defence and aerospace and for measurement in bio-medical, automotive, chemical, manufacturing, energy, structural, petrochemicals, electronics, construction, civil infrastructure and medical industries. The technological advancement over the years has made FOSs an attractive alternative to conventional sensors for measuring pressure, temperature, humidity, vibration, viscosity, rotation, acceleration, strain, magnetic field, electric field etc.

1.2 Motivation

According to the sensing element, optical fibre sensors can be sub-classified into extrinsic and intrinsic sensors [1]. In extrinsic sensors, the optical fibres are only used to guide light to in and out of the fibre transducer and the optical signal is modulated by an external sensing part.

In intrinsic sensors a part of the fibre is used as the sensing part, when the optical signal travels through this part, one of light characteristics is modulated by changes in the measurand.

According to a report given by ElectroniCast (http://optics.org/news/3/6/27/SENSORSM) the value of FOSs systems will grow at an average annual rate of 20.5%. The consumption value of fibre optic point sensors and distributed fibre optic sensor system links will grow at an average annual rate of 20.5% from $1.34 billion to $3.39 billion per year between 2011 and 2016. (Figure1.1) [2]

Another report by BBC research [3] confirms that given a Compound Annual Growth Rate (CAGR) of 10.5%, the global market value of fibre optic sensors is calculated to increase to more than $2.5 billion in 2017. In the 5-year period between 2012 and 2017, the global market value for intrinsic sensors, as indicated in Figure 1.2, is calculated to increase at a moderate CAGR of 8.8% to more than $2.2 billion. The growth of the market value for extrinsic FOSs worldwide is expected to be stronger, with new products projected for the medical market. In 2012, total market value was estimated to be $72

million. In the 5-year period between 2012 and 2017, the global market value for extrinsic FOSs is calculated to increase at a CAGR of 33.3% to $302.9 million.

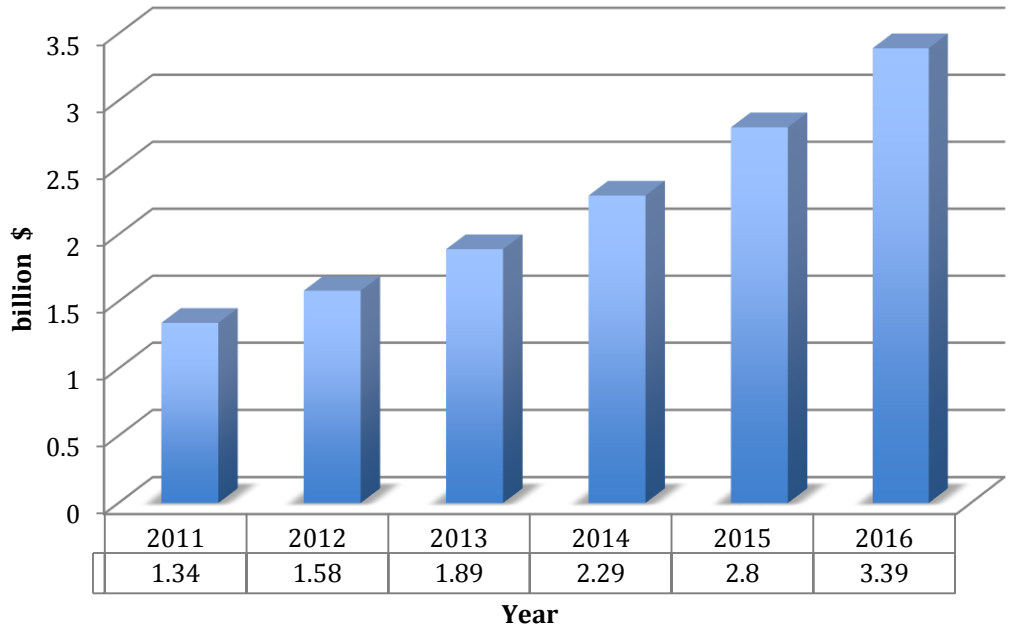

Figure 1.1 The value of fibre-optic sensor systems will grow at an average annual rate of 20.5%.[2]

Figure 1.3 shows the global market classified based on the applications of sensors from 2009 to 2016 and it is noticeable that the market for temperature and pressure sensors ranked to be the second based on the market data obtained from 2009 to 2011. This sector is expected to be worth $14 billion in 2011 and $20 billion in 2016 [3].

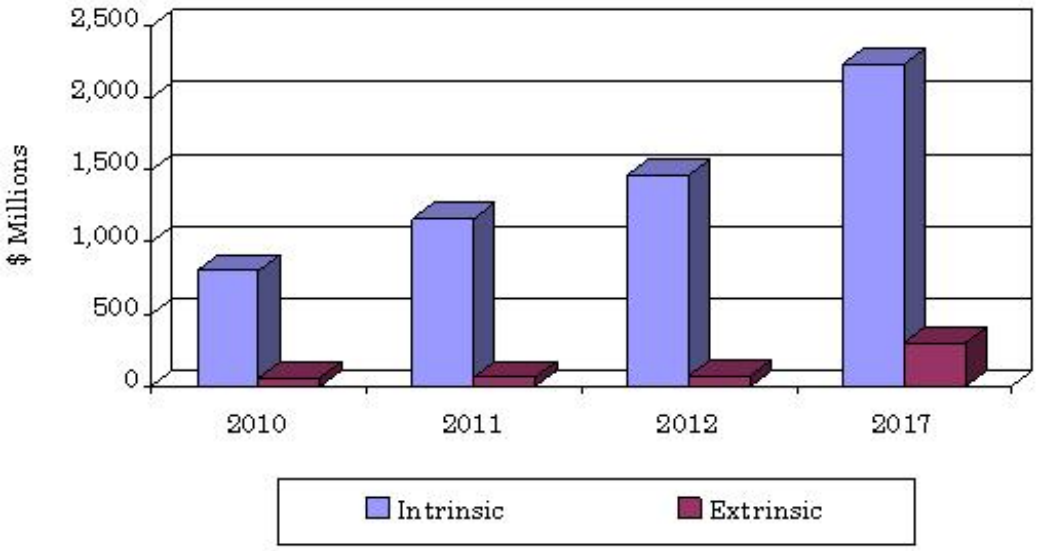

Figure 1.2 Global values for FOSs by type, 2010-2017 ($ Millions)[3]

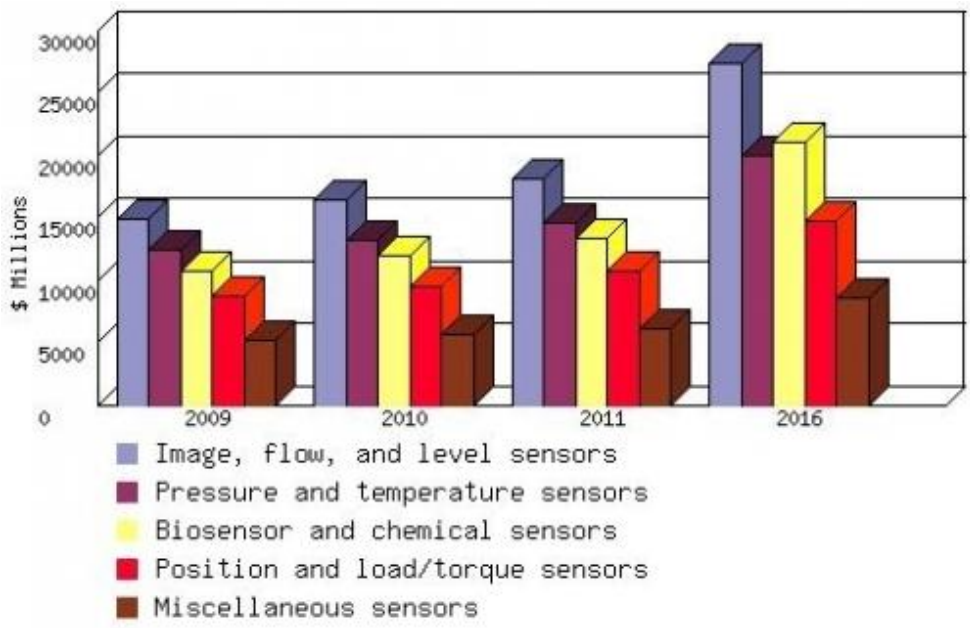

Figure 1.3 Global market for sensors, 2009-2016 ($ Millions [3]

All the above statistics confirms that there is a strong industrial demand for temperature and pressure sensors and that the FOS market is growing rapidly. Therefore the focus of this project is to

develop advanced optical fibre based temperature/pressure sensors, based on the technological advancement in the field of optical fibre sensors. This will be achieved by incorporating novelty both in fibre structural design and in the sensing mechanisms used.

1.3 Aims and objectives of the work

The aims and objectives of the work are to develop fibre optic lateral pressure sensors, either point or distributed, based on the birefringence characteristics of polarizing maintaining fibres. The research involves both theoretical analysis and experimental implementation and validation. Several types of High, Medium and Low birefringence optical fibres, including conventional fibre such as Panda, two special side hole with one-hole that has a hole diameter of 30 μm and Two-hole that has two holes with the same diameter of 27 μm and also four different Photonic Crystal Fibres (PCFs) such as two standard hexagonal PCFs (Types 391b3 and 090329P), a Hi-Bi PCF (Type 070107P2), and a six-hole PCF (Type 478b2) have been analyzed and evaluated extensively for various potential applications. Thus the main focus of the research in this dissertation includes:

- Theoretical analysis of a non-symmetric polarization-maintaining single mode fibre for sensor applications
- Investigation of single mode polarization-maintaining fibres for directional transverse force measurement
- Evaluation of high birefringence single mode optical fibre-based pressure sensors for potential structural condition monitoring
- Transverse pressure sensitivity of birefringent photonic crystal fibres
- Transverse force sensitivity of joint photonic crystal fibres

1.4 Structure of the thesis

Chapter 2 includes more detailed background information about both conventional and optical fibre pressure sensors.

Chapter 3 starts with theoretical discussions in relation to light wave propagation in fibres and mode coupling theory. The theoretical analysis of polarization maintaining fibres under lateral force is also discussed extensively in this Chapter.

Chapter 4 details the fabrication process of optical fibre pressure sensors and their subsequent performance evaluation, coupled with the underpinning theoretical analysis

Chapter 5 summarizes the major achievements made throughout the project period in response to the aims and objectives set out in Chapter 1 and puts forward some ideas for future work.

Chapter 2

Background and review of pressure sensor technologies

2.1 Introduction

The first attempts in history to measure pressure were made a long time ago [4]. In 1594 Galileo Galilei filed a patent for the design of a machine to pump water from a river for the irrigation of land. In his design a syringe was used as a pump and he reported that 10 meters was the maximum to which the water would rise in the suction pump [5], but there was no explanation for this phenomenon. Many years later and during the 17th century the first attempts, which involved the contributions from the famous scientists Torricelli and Pascal, were made to measure the pressure and this led to the birth of first prototypes of the barometer [6]. After that in 1643 Evangelista Torricelli, filled a one-meter long tube, hermetically sealed at one end, with mercury and set it vertically with the open end in a basin of mercury. The column of mercury invariably fell to about 760 mm, leaving an empty space above its level. Torricelli attributed the cause of the phenomenon to a force on the surface of the earth, without knowing where it came from. He also concluded that the space on top of the tube was empty, that nothing was there and called it a "vacuum"[7].

In 1647 Blaise Pascal heard about the experiments of Torricelli and was searching for the reasons of Galileo's and Torricelli's findings [8]. He came to a conclusion that the force, which keeps the column at 760 mm, is the weight of the air above. Thus, on a mountain, the force must be reduced by the weight of the air between the valley and the mountain. He predicted that the height of the column would decrease and this was subsequently proved with his experiments at the mountain Puy de Dome in central France [8] and from the decrease he could calculate the weight of the air. Pascal also formulated that this force, he called it "pressure", is acting uniformly in all directions [9]. Otto von Guericke in 1656 developed new air pumps to evacuate larger volume of air and staged a dramatic experiment in Magdeburg by pumping the air out of two metal hemispheres, which had been fitted together with nothing more than grease [10]. Eight horses at each hemisphere were not strong enough to separate them [11]. In 1660, Robert Boyle used "J"-shaped tubes closed at one end to study the relationship between the pressure and volume of trapped gas and the conclusion was made through Boyle’s law named after him: The product of the measures of pressure and volume is constant for a given mass of air at a fixed temperature [12] [13]. In 1738, Daniel Bernoulli developed an impact theory which was able to deduce Boyle’s law analytically. In 1820, Joseph Louis Gay-Lussac, a French physicist and chemist, verified Charles Gay Lussac law through experiments, confirming that the pressure increase of a trapped gas at a constant volume is proportional to the temperature [4]. 20 years later, William Thomson (Lord Kelvin) defined the absolute temperature [14]

In the 19th century, mechanical measurement technologies came to the forefront. In 1843 Lucien Vidie, invented and built the aneroid barometer, which uses a spring balance instead of a liquid to measure atmospheric pressure [15]. The spring extension under pressure is mechanically amplified through an indicator system. Employing the indicator method of Vidie, Eugene Bourdon (founder of the Bourdon Sedeme Company) patented the Bourdon tube pressure gauge for higher pressure measurement [16]. This was certainly a positive step in a new area and after that the early pressure measurement methods were replaced by pressure transducers and transmitters. In the case of pressure measurement, a transducer is a device that converts the energy of applied pressure to another form of energy such as electric, magnetic, mechanic and so on and a gauge is an instrument used to measure pressure.

The first electrical pressure transducers introduced in 1930 were capacitance-based [17]. The pressure change is reflected in the movements of diaphragms, springs or Bourdon tubes which form a part of a capacitor. E. E. Simmons from the California Institute of Technology and AC. Ruge from Massachusetts Institute of Technology independently developed the bonded strain gauges in 1938 [18]. The first foil strain gauges came up in 1955 with an integrated full resistor Wheatstone bridge, which was bonded on a diaphragm. The bonding connection of the gauges to the diaphragm was always the cause for hysteresis and instability. In the 1960's, Statham introduced the first thin-film transducers with good stability and low hysteresis [19]. Until today this technology still plays an important role in modern sensor designs for high pressure measurement.

However, the above thin-film based transducers have shown limitations for low pressure measurement. To address this problem, William R. Poyle first produced a capacitive transducer based on glass or quartz and a few years later in 1979 Bob Bell produced similar capacitive transducers based on ceramic. Through the change in sensor substrate material lower pressure measurement can thus be achieved [17].

Modern sensor development started in 1967 at the Honeywell Research Center when Art R. Zias and John Egan applied for patents for the design of an edge-constrained silicon diaphragm [17]. Subsequently Hans W. Keller filed a patent for the batch-fabricated silicon-based sensor which has benefited significantly from the enormous progresses made in the IC industry starting from 1969 [17].

All the pressure sensors discussed above have included an important displacement or deformation element, which has a defined surface area and deforms as pressure changes. Thus, the pressure measurement can be translated to a measurement of a displacement or force. The device, which measure the displacement, are called transducers

2.2 Conventional pressure sensors

2.2.1 Liquid manometer

The liquid Manometer or Mercury Pressure Sensor is one of the oldest devices used for pressure measurement yet is simple and efficient. The sensor design is based on the hydrostatic balance principle. Figure 2.1 shows a liquid manometer pressure sensor in which a U-shaped wire is immersed into mercury with its resistance being changed in proportion with the height of mercury in each column [12]. The resistors are connected into a Wheatstone bridge circuit, which remains in balance as long as the differential pressure in the tube is zero. If additional pressure is applied to one of the arms of the tube and misbalances the bridge, this results in an output electrical signal. The higher the pressure in the left tube, the higher the resistance of the corresponding arm is and the lower the resistance of the opposite arm is. The output voltage is proportional to a difference in resistances of the wire arms.

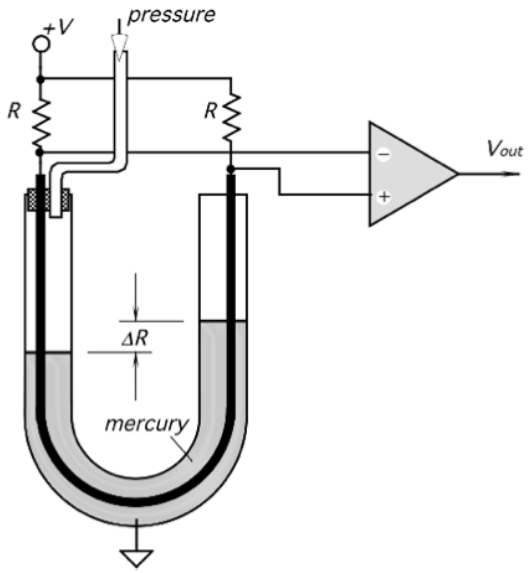

Figure 2.1 Mercury-filled U-shaped sensor for measuring gas pressure [9].

2.2.2 Mechanical pressure gauges and pressure transducers manometer

In most conventional pressure sensors, the sensing element is a transducer, which is a mechanical device and undergoes structural changes under strain. In fact a conventional pressure

transducer is a device that converts an applied force or pressure into an electrical or mechanical signal. [20]-[23]

In general, two steps are involved in measuring the force or pressure. The first step is to sense the pressure, which is usually associated with the elastic deformation of a flexible membrane such as a Bourdon tube, bellows or a diaphragm [24], as discussed in Section 2.1, with its deflection being directly related to the pressure variation. The second step is to convert the deflection into a more convenient form for display or recording or both [22][23].

Figure 2.2 shows a number of Bellows and Bourdon tubes which have been widely used as pressure sensitive elements. Despite the fact that they are in different shapes, including C, spiral, helix, and twisted, they are all made of metal.

Bellows generally consist of a cylinder with flexible sides and rigid ends which can deflect under pressure. Bellows can be used as a sensing part of some transducers such as potentiometers and differential transformers [25]

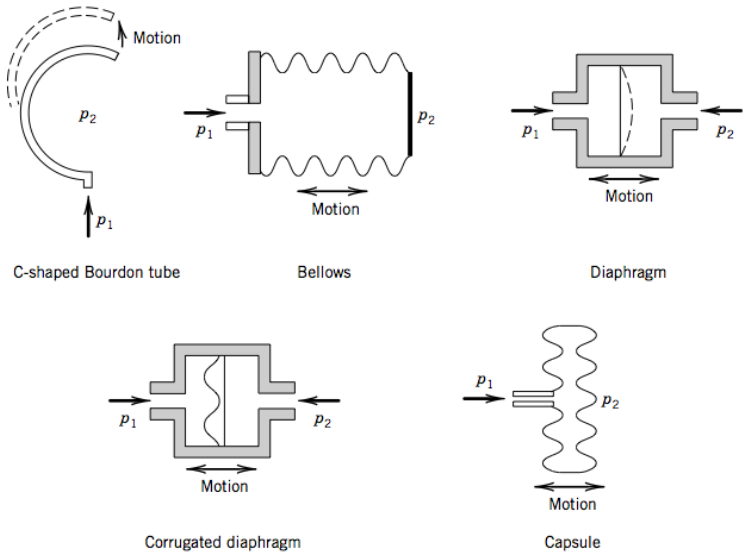

Figure 2.2 Elastic pressure-sensing elements.[9]

Diaphragms are another type of widely used pressure sensing elements which can be configured in single or capsule arrangements [26]. As shown in Figure 2.2, diaphragm deflection is related to the difference between the pressures applied on either side, so this design can measure either absolute or relative pressure depending on the reference used. When the diaphragms are configured to be a capsule

by welding two or an array of diaphragms together [26], as shown in Figure 2.2, internal pressure can thus be measured. A capsule diaphragm usually has a higher pressure sensitivity than that of a single diaphragm of the same size but with a longer response time. Further enhancement of sensitivity can be achieved by increasing the number of diaphragms welded together, i.e. an array of diaphragms demonstrates a higher sensitivity than a capsule with two diaphragms.

2.2.3 Electrochemical transducers

Some metals have also been used as transducers as their resistance changes with strain. The two most widely used forms of variable resistance transducers are potentiometers and strain gauges.

Potentiometers are the simplest and cheapest transducers and Figure 2.3 shows a typical arrangement. It includes a linear or angular wiper (or connecting rod as shown in the diagram) connected to a sensing element. The movement of the wiper arm, which is connected to an electrical resistance, changes the output voltage and thereby indicates the pressure applied on the sensing element. This type of arrangement is usually used for static or quasi-static measurements [27]

The strain sensitivity of metals was first observed in copper and iron by Lord Kelvin in 1856 [28]. The strain gauge is a device that changes electrical resistance due to stress. Strain gauges can be directly bonded to a flat or corrugated metal diaphragm [25][29]. An applied pressure changes the diaphragm strain and thus strain gauge resistance, which is usually detected in the form of a voltage from a suitable Wheatstone bridge arrangement.

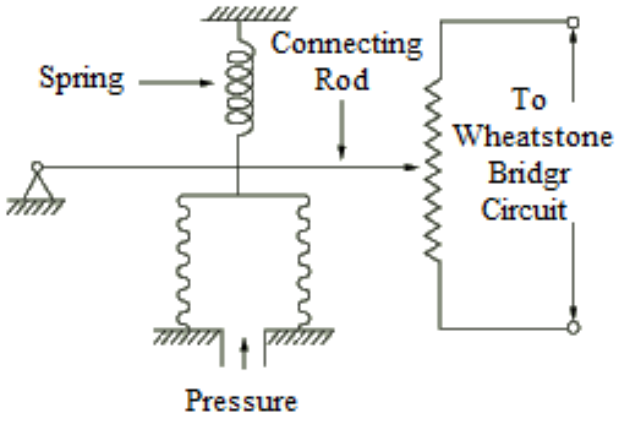

Figure 2.3 Potentiometer pressure transducer [27]

Another type of transducers is magnetic transducers in which the inductance characterizes the ability of a coil to resist any change in the current passing through it. Reluctance characterizes the capacity to induce a signal in a second coil [30][31]. Inductance and reluctance vary when an iron core move either inside a coil or between two coils. Figure 2.4 shows a Linear Variable Differential Transformer (LVDT) coupled to a Bourdon gauge as the sensing element [32]. The iron core can be coupled to a sensing element and therefore a change of pressure, which moves the iron core, can be detected when a current is passed through the primary coil.

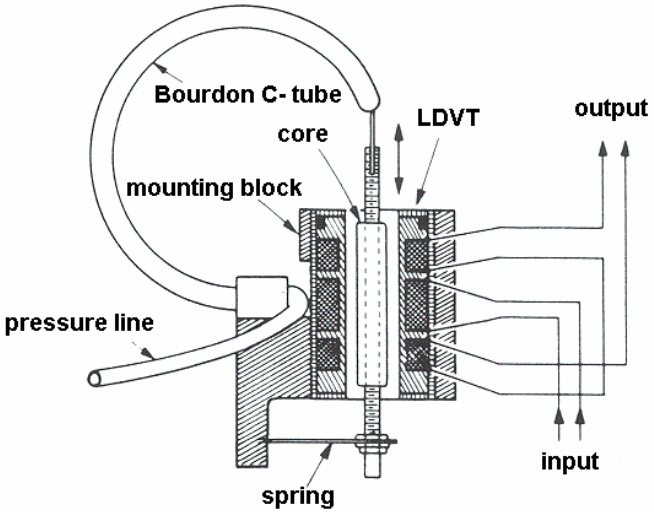

Figure 2.4 Pressure transducer that uses a Bourdon tube as sensing element and LVDT [26].

LVDT is one of the most popular magnetic transducers. Due to the lack of contact between core and coils, the working life of an LVDT is long and friction and hysteresis are due to mechanical coupling eliminated.

Capacitive transducers are another type of electromechanical pressure transducers as the capacitance between two plates depends on the distance between them and the distance can be altered through pressure variation. In this type of configuration, one plate of the capacitor can be employed as a diaphragm [24]. Capacitive transducers have demonstrated extreme ruggedness, long life, and can work under harsh conditions such as with temperatures up to 1100℃ [30], [34].

Figure 2.5 shows some key features of a typical capacitive pressure transducer, which can be made very small if silicon technology is used [25],[33]. Disadvantages of capacitance transducers include their temperature sensitivity [22], small output signals, and the influence of cable capacitance [32][34].

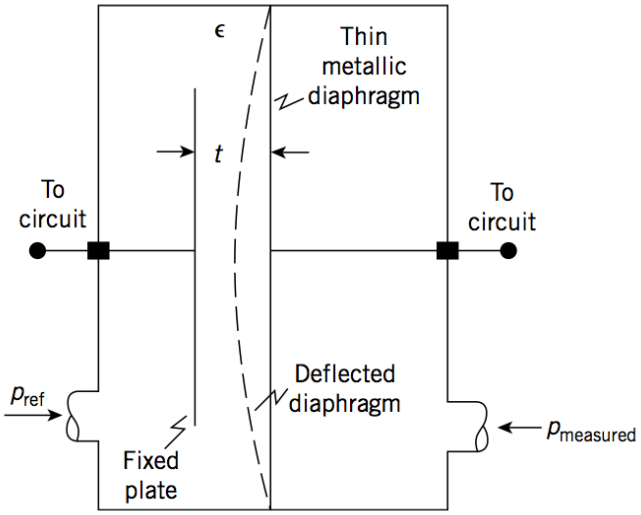

Figure 2.5 Capacitive pressure transducer [25].

2.2.4 Piezoresistive transducers

Piezoresistive transducers are based on the idea that a mechanical input such as pressure, force applied to a mechanical structure, e.g. diaphragms, beams or plates, causes the structure to experience mechanical strain [35]

As discussed above, two essential components are required to make a pressure sensor. They are a sensing element, such as a diaphragm, and a detector, which responds to deformation of the diaphragm, both of these components can be fabricated in silicon.

A silicon- diaphragm pressure sensor consists of a thin silicon diaphragm as an elastic material and a piezoresistive gauge resistors made by diffusing impurities into the diaphragm [36]. They can be made as a strain gauge and bonded to a diaphragm, or they can be formed as an integral strain gauge diaphragm device. Piezoresistive strain gauges show a higher sensitivity than that of conventional metallic strain gauges [37], and furthermore, silicon has lower thermoelastic and creep effects. Their usual working pressure range is between 0.1 kPa to 100 MPa [34],[36]. These transducers are required to be protected from aggressive materials and their maximum operating temperature is about 120°C. They break easily if the pressure exceeds the maximum working pressure [22] and are not suitable for operating in wet conditions [22],[26]. Figure 2.6 shows the design of a typical piezoresistive diaphragm pressure transducer.

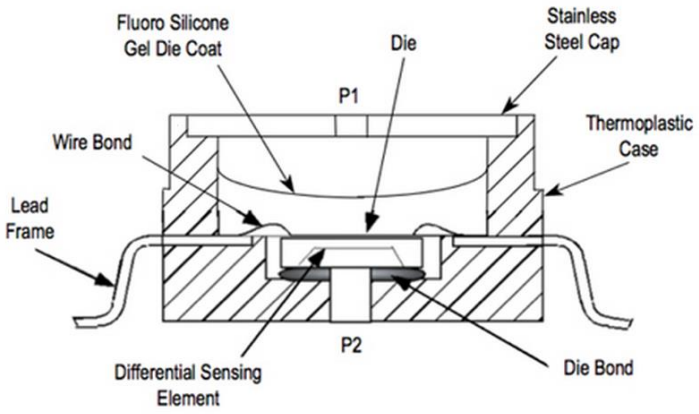

Figure 2.6 Structure of a semiconductor pressure sensor [38]

2.2.5 Piezoelectric transducers

The piezoelectric effect was initially observed in 1880 by the Curie brothers [39][40]. Some materials, such as quartz, tourmaline, Rochelle salt, and barium titanate, do not have a centre of symmetry and they can produce an electric charge when they are subjected to a sudden change of pressure [30],[40].

Quartz is the most common material used in piezoelectric pressure transducers due to their capability of withstanding against strain, low hysteresis, linearity [21],[26],[41].

Figure 2.7 illustrates such a piezoelectric pressure transducer. Piezoelectric pressure transducers have been widely used for transient pressure measurement due to their high natural frequency [23][26]. They do not show sensitivity to slow changes of pressure and therefore, they cannot be employed for static pressure measurements.

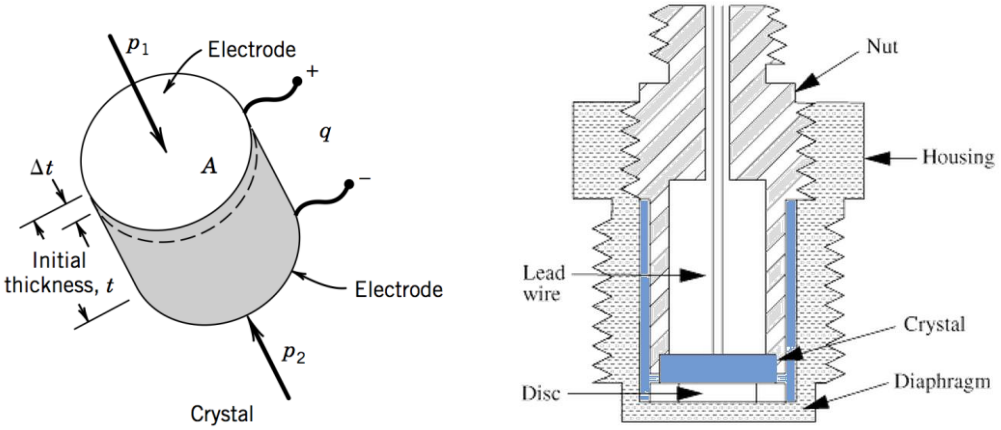

(a) *(b)*

Figure 2.7 Piezoelectric pressure transducer using a diaphragm as a force-summing device (a) Schematic of pressure transducer (b) incorporating the diaphragm in the housing [42]

2.3 Fibre optic pressure sensors

2.3.1 Introduction

Light guiding and bending studies go back to mid 19th century when D. Collodon and J. Babinet for the first time showed that the light could be guided in jets of water in 1841 [43], then in 1854 the British physicist J. Tyndall demonstrated this effect in his popular lectures on science. In 1880 [44], W. Wheeler patented a scheme for piping light through buildings [45] which included a net of pipes with reflective linings and diffusing optics to carry light through a building but this project was not successful. However the idea of light piping was finally converted into the design of optical fibres. During the 1920s,

J. L. Baird in England and C. W. Hansell in the United States patented the idea of image transmission through arrays of hollow pipes or transparent rods [45]. In 1930, H. Lamm, used a bundle of unclad optical fibres for image transmission although the quality of image was poor [45].

Modern optical fibres technology began in 1953 when A. van Heel of the Technical University of Delft in Holland published his first report of clad fibre in Dutch-language weekly De Ingeneur [46]. He introduced the concept of a bare fibre of glass with a transparent cladding of lower refractive index, which was not just to protect the reflection surface from contamination, but also to greatly reduce crosstalk between fibres.

The invention of the laser in 1957 provided a suitable light source for the research in optical fibres. In 1966 Kao and Hockman pointed out that purifying glass could dramatically improve its transmission properties [45].

A year later, the first patent on fibre optic sensing had been filed by Menadier, C. Kissinger, and H. Adkins [47]. In 1970 the scientists from Corning Glass reported the revolutionary success that fibres made from extremely pure fused silica had shown losses below 20 dB/km at 633 nm. Over the next few years, fibre losses dropped dramatically and this triggered the beginning of using fibres for many applications, for example as a sensor. After Menadier's patent was published, Eli Snitzer used fibre optics for phase modulation in 1971 [48] and during the following years this technique was improved and has become one of the most important modulation techniques in fibre optic telecommunications and sensing.

Extensive research in optical fibre sensing began in the late 1970s when J.H. Cole *et al.* [49] and J.A. Bucaro *et al*. [50] at the Naval Research Laboratory published a paper, for the first time, discussing the sensitivity of fibre optic acoustic sensors in the Journal of the Acoustical Society of America (JASA). This was followed by a large volume of research focused on the design, interrogation and application of these sensors, enabling them being one of the most well developed fibre-optic sensors [51]-[53]

Coupled with the technological advancement in sensing, applications of Optical Fibre Sensors (OFSs) have grown rapidly in different areas for measurement of a number of physical and chemical parameters, such as Temperature, Humidity, Strain, PH, curvature, displacement, rotation and pressure [54][60].

Over the past three decades, research on optical fibre pressure sensors has been buoyant as pressure has been recognized as the second most important physical parameter after temperature that is

required to be measured for various applications. Pressure can be measured over a very broad range from 10^{-12} Pa, in extreme vacuum up to 10^{+12} Pa, in explosions [61].

G. B. Hocker [62] was the first to measure pressure in 1979 using a fibre-optic Mach-Zehnder interferometer. Fiels *et al*. [63] were the first to measure hydrostatic pressure in 1980 using optical fibre micro-bend technique. In 1982, Spillman [64] demonstrated the success of an extrinsic fibre optic pressure sensor based on the photoelastic effect. The appearance of High Birefringence (Hi-Bi) fibres in the sensing area created a new generation of fibre-optic sensors that are known as polarimetric fibre sensors, which relate polarization or phase modulation to various external perturbations.

The first study on polarimetric (PM) pressure sensors was undertaken by Xi *et al*. [65] in 1986. This was followed by more extensive research in the field using a variety of polarimetric (PM) fibres with cores and claddings in different shapes, sizes and configurations.

Since Photonic Crystal Fibres (PCFs) were first introduced by Knight *et al.* [66] in 1996, there has been a wide spectrum of research undertaken, exploring the potential of using these micro-structured optical fibres as sensors for various measurement applications [67], such as strain and temperature sensors [68][69] and hydrostatic pressure sensors [70][71]. Clowes *et al.* [72] reported a pressure sensitivity of a side-hole optical fibre sensor for downhole monitoring in oil wells. Polarimetric interferometric schemes have been investigated to interrogate the output of Hi-Bi fibre sensors. This method is highly accurate for measurement of deformation in short optical fibres, and it is very suitable for analysis of polarization-mode dispersion in Hi-Bi fibres. R. Passy *et al.* [73] have reported the effects of pressure on mode propagation by measuring the group delays with an all-fibre Michelson interferometer. Bock *et al*. [74] reported a fibre-optic polarization-sensitive intermodal interferometer for simultaneous measurement of pressure and temperature. Also they reported [75] a white light multiplexed pressure, strain, and temperature sensors by using Hi-Bi fibres as sensing elements for which their cross-sensitivities could be compensated. A number of extrinsic fibre-optic pressure sensors have also been developed, including those based on Fabry–Pérot interferometers (FPI) [76] Fizeau interferometer [77], as well as Micro-Electro-Mechanical Systems (MEMs) based sensors [78].

Research on PM fibres has also been undertaken, exploring their potential as lateral force/pressure sensors based on their birefringence characteristics. Zhang *et al*. [79] have theoretically investigated the birefringence properties of a Panda-type PCF and shown that there is a dependence on the direction of the force being applied. Liu et. al. [80] reported a similar dependence on the direction of force for a simulated grapefruit-structured PCF. In order to improve the detection sensitivity of the PCFs to lateral pressure variation, various interrogation schemes, such as using fibre gratings [81] or an

interferometric configuration [82][83] were reported. The work reported by Peng *et al.* [84] shows that when a standard hexagonal (low birefringent) PCF is used as a transverse load sensor, an (unspecified) offset load is required to introduce the desired birefringence for measurement and the highest sensitivity to transverse load reported in literature using PCFs is around 0.5 nm/N·mm [83][85].

2.3.2 Advantage and disadvantages of optical fibre pressure sensors

Optical fibre-based sensors, compared to conventional electrical pressure sensors, have shown both technical and economical advantages and disadvantages as summarized below:

- Optical fibre pressure sensors are made from a very durable material (e.g. silica) [85] that is corrosion resistant and can withstand high tensile loading (can withstand up to 5% elongation) [86]
- Optical fibre pressure sensors can work over a wide range of temperatures from -200°C to 800 °C for silica, 2000 °C for sapphire fibres [87],
- Low mass and small diameter of fibres offer a significant flexibility for optical fibre pressure sensors to fit for complex surfaces or access areas which are difficult to reach for conventional sensors.
- Point, quasi-distributed or fully-distributed sensing is made possible over the length of an optical fibre (<1 mm to kms).
- The low loss of optical fibres make them suitable for remote sensing
- The immunity to electromagnetic interference (EMI) enables optical fibre pressure sensors to operate in electrically noisy environments, therefore they are intrinsically safe and suitable for use in hazardous areas
- The inert nature of optical fibres offers electrical isolation (they are non-conductive).
- Optical fibre pressure sensors can offer a higher sensitivity as the optical signal analysis can be based on phase change of light instead of the intensity change.
- Multi-point and multi-parameter monitoring, thus reducing system cost and complexity.
- Possibility to create a fibre optic sensor network
- Mechanically rugged.
- Possible low cost for multi-point sensors, high performance.

The major disadvantages associated with fibre optic sensors are:

- Cross-sensitivities are required to be addressed and compensated when necessary.

- Cost and availability of suitable instrumentation.
- Low general awareness of fibre optic sensor technology.

2.3.3 Review of optical pressure sensor technologies

2.3.3.1 Introduction

It was in early 1970s that researchers realized that physical perturbation can modulate guided light in fibre optics. After that, various sensors have been developed taking the advantage of the technological advancement in optical fibres manufacturing and the availability of detectors and optical sources.

In a fibre optic sensor, different characteristics or properties of the transmitted light such as intensity, polarization direction, wavelength and phase can be modulated to carry information about the measured variable. Using this approach, fibre optic sensor designs can be separated into four major categories based on the parameters being modulated. These include:

- Intensity
- Phase
- Polarization
- Frequency or Wavelength

By measuring the change of these parameters resulting from the interaction between the optical fibre and the measurand, fibre optic sensors can be designed to measure a broad diversity of physical and chemical parameters.

For intensity-modulated sensors, which are known as intensity-type sensors, the measurand affects only the brightness or intensity of the light that is transmitted along an optical fibre. However, for phase-modulated or interferometric sensors, the measurand variation is encoded in the phase difference between the light returning from a sensing optical path and the light from a reference optical path. Other sensor types can modulate the frequency or wavelength of the light signal or use an optical phenomenon known as fluorescence.

2.3.3.2 Intensity-Modulated pressure sensors

Intensity-based pressure sensors were one of the first OFSs to be commercialized [61]. These sensors were analogue, as the light intensity detected is proportional to the measured variable.

The advantages of these technologies include:

- Robustness,
- Simple configuration with no requirement for the use of expensive optical devices.
- Low fabrication cost
- Flexibility

The main limitation of intensity-based sensors is the intensity fluctuation which can be caused by perturbation irrelevant to the measurand, such as the fluctuation of the light source or the deterioration of optical fibres.

Intensity-modulated sensors are usually configured to accentuate the following modulation mechanisms:

- Signal intensity change due to the loss in transmission and/or reflection
- Signal intensity change due to the loss resulting from the fibre microbending
- Evanescent wave modulation
- Signal intensity change due to the polarization variation as a result of the Refractive Index change in the surrounding environment

Intensity modulated OFSs can be configured as transmissive or reflective in their physical design, here are described below:

Transmissive sensors are extrinsic sensors which include two fibres with one being connected to a light source and the other connected to a detector [88]. The light beam propagating through the optical sensor is modulated either directly by the transverse or longitudinal displacement of two fibres or a change, in this case can be angles between two fibres [90] [91]. In either case, the intensity change detected by the sensor system is directly related to a variation of the physical quantity of interest [92]-[96].

Figure 2.8 shows a simple design of a transmissive fibre optic pressure sensor using a shutter to modulate the intensity of pressure sensors [97][98]. In this design, the movable shutter is mechanically connected to a diaphragm and the light beam travels from a fixed fibre into the other fibre. The amount of light that reaches the second fibre is dependent on the amount of shutter displacement.

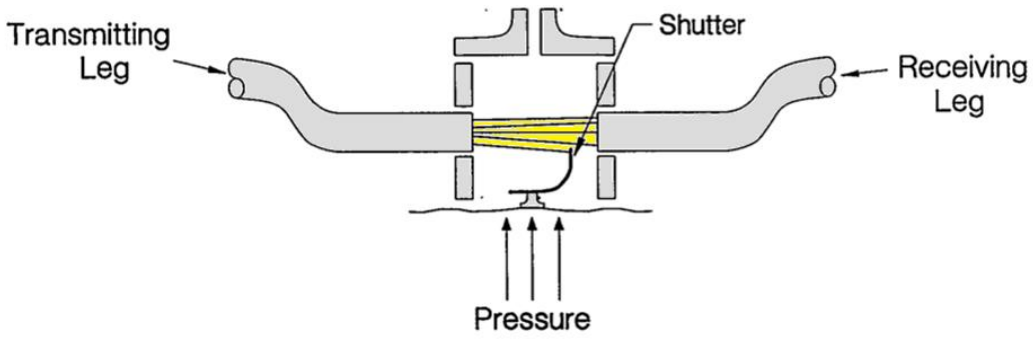

Figure 2.8 Transmissive fibre optic pressure sensor using a shutter to modulate the intensity [98].

A similar design is shown in Figure 2.9. In this pressure sensor the shutter is replaced by two diffraction gratings with one being fixed and the other movable and connected to a diaphragm. Both fibres are fixed and the movable diffraction grating modulates the light intensity [98][99].

When pressure is applied on the diaphragm, the movable grating is displaced, resulting in the change in the intensity of the transmitted light. The sensitivity of the sensor can be enhanced by reducing the grating pitch.

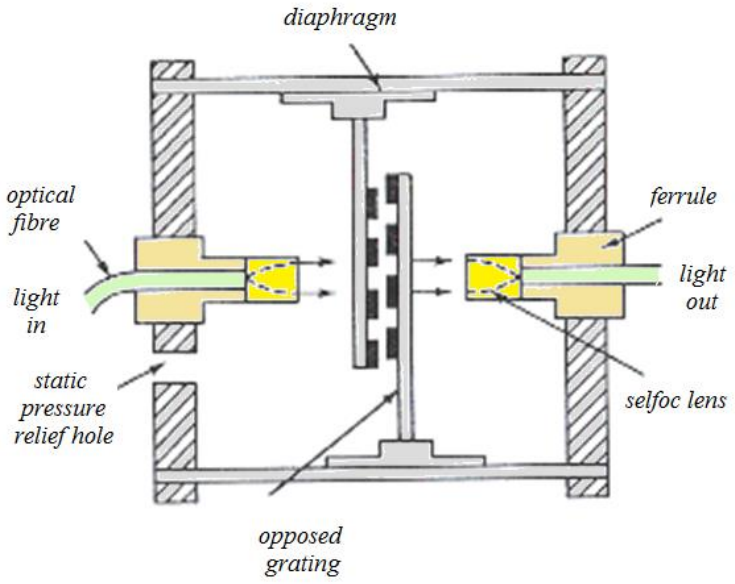

Figure 2.9 Transmissive fibre optic pressure sensor using a moving grating to modulate the intensity [98]

Another transmissive fibre sensor, as shown in Figure 2.10, is based on the modulation of the optical signal through transverse displacement caused by the deflection of a diaphragm. In this design, two optical fibres are properly aligned to ensure a maximum amount of light from the light source being transmitted through to the detector. The amount of energy captured by the receiving fibre, however, depends on its numerical aperture (NA) and the axial separation between the two optical fibres. When the separation is modulated, it in turn results in an intensity modulation of the light captured [98][100][102]

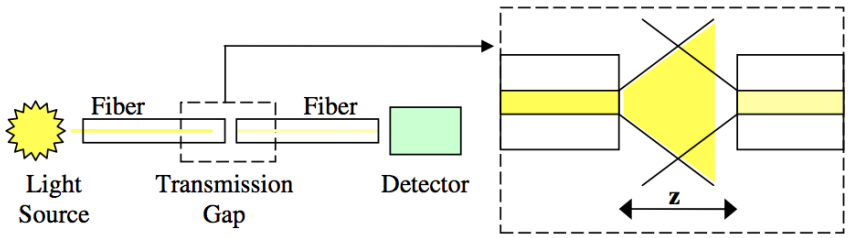

Figure 2.10. Schematic of an intensity based sensor system with a transmission gap [102].

Different from the above transmission gap configuration, Figure 2.11 shows a reflective gap configuration, which consists of an external reflecting element and two bundles of fibres or pair of single fibres. The light is reflected by the external mirror that is connected to a diaphragm [104][105]. The

sensitivity of the sensor is dependent on the distance between the fibre surface and the external mirror [105]-[106]

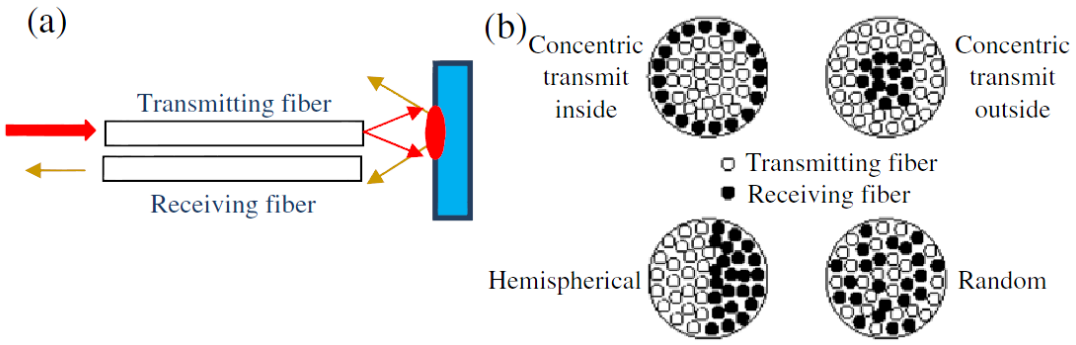

Figure 2.11 Illustration of a fiber optic intensity sensor for distance measurements. (a) Two-fiber sensor, showing the object and the operational principle (b) Various geometries for fiber bundle sensor heads, [106]

Figure 2.12 shows the relationship between the detected light intensity and the distance between the fibre sensor to the target (mirror) when different configurations of fibre bundles are used. [100][106]

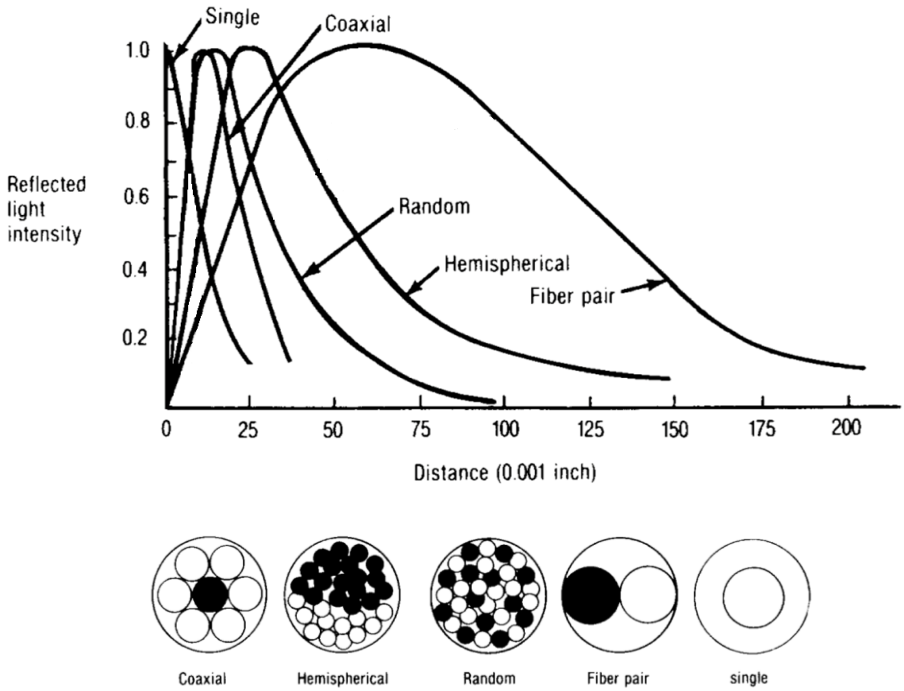

Figure 2.12 shows the detected light intensity versus distance from the target [100].

The problems associated with intensity-based sensors are random changes of transmissivity of optical path and variations of the output power of the optical source, which directly affects the accuracy of the sensor [108]. Intensity sensors therefore need a mechanism that compensates for those changes. In addition, this type of sensor can only be used to measure an absolute pressure as it is impossible to distinguish between positive and negative pressures across the diaphragm.

W. B. Spillman *el al.* [109] were the first to design a Frustrated Total Internal Reflection (FTlR)-based sensor which was a modification of the transmissive sensor. As shown in Figure 2.13, a typical FTIR sensor consists of two fibres, each with their ends being polished and being parallel to each other at an angle to the fibre axis. One of the fibres is fixed and the other is attached to a diaphragm. As pressure is applied to the diaphragm, the movable fibre is displaced radially with respect to the fixed segment [110][111]]. Due to the interaction between the incident and reflected light in the movable fibre, some light energy may be coupled into the fixed segment. The amount of light coupled into the fixed fibre is dependent on its distance from the movable fibre. This type of sensor is one of the most sensitive sensors based on transmissive intensity modulation.

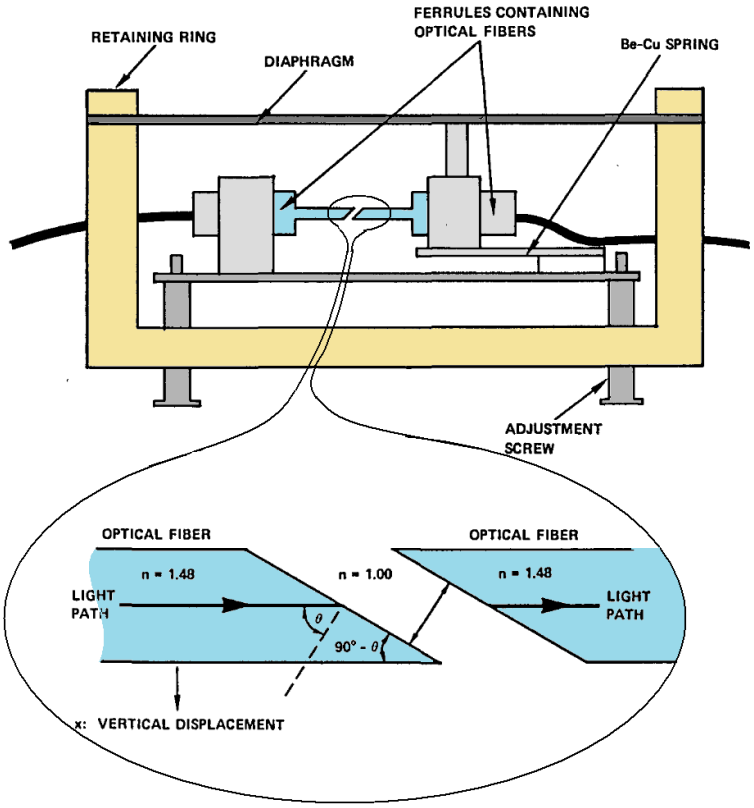

Figure 2.13 Frustrated-total-internal-reflection mode sensor [109]

Microbending Sensors

Fields *et.al.* [63][112]. were the first to propose and demonstrate a sensor based on microbending in optical fibres More research has been undertaken to understand better micro-bend sensors and to investigate how to increase dynamic range and improve the sensitivity to the parameter of interest while reducing the sensitivity to unwanted variables. The early interest in micro-bend sensors was primarily for hydrophone applications [113]-[114].

As illustrated in Figure 2.14 a typical microbend sensor consists of a multimode step index optical fibre, which is squeezed between grooved or corrugated surfaces [113]-[115]. One of the surfaces is attached to the diaphragm, and as the diaphragm is displaced, the fibre is squeezed and bent. As the fibre is bent, an amount of light proportional to the pressure applied to the diaphragm is lost due to microbending attenuation [116]-[118]. The higher order modes of light are the ones most affected by a microbend since they encounter the core to cladding interface at angles only slightly greater than the critical angle.

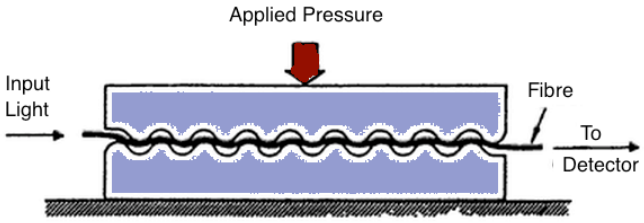

Figure 2.14. Fibre optic microbend pressure sensor

Microbend sensors have demonstrated unique advantages [119], which include higher mechanical and optical efficiency that leads to low parts count and low cost, easy mechanical assembly that does not require fibre bonding to the other components, thus avoiding differential thermal expansion problems, and failure-safe which either produces a calibrated output signal or fails to a state with no light output. In addition, microbend sensors can be used in aggressive environment such as under high-temperature and hazardous conditions [120].

Lagakos, *et al*. [121] showed that in a microbender, light is lost from the fibre core via coupling between guided modes and radiation modes. In addition, upon encountering a microbend, lower order

light modes may be transformed into higher order modes which can be refracted into the cladding at the next microbend. A series of microbends can therefore lead to significant light losses.

In general, as the number of bending points on the corrugated surfaces is increased, and as the spacing between the corrugations is decreased, the sensitivity of the sensor is enhanced. Work done by Horsthuis [119], Diemer [120], and Lagakos, *et al.* [121] provides a guideline for microbend sensor designs, showing how best to select the corrugated spacing in order to achieve the highest sensitivity. On the other hand Yao, *et al.* [122] have shown how the radiation modes in the cladding of a microbend sensor can re-enter the core and reduce the sensitivity.

The fibre optic cable in microbend pressure sensors is usually protected by a metallic or polymer buffer coating both to extend its mechanical lifetime and to avoid interference of stresses arising from the other sources, such as high temperature and the other environmental perturbation.

Evanescent Wave Sensor

Another type of intensity based fibre optic sensors is the evanescent wave sensor that utilizes the light energy, which leaks from the core into the cladding. These sensors have been widely used as chemical sensors [123] but some are used as pressure sensors [124]-[128].

The light guided within an optical fibre is not totally confined within the core of the single mode fibre, with a portion penetrating inside the cladding layer, which is termed as *evanescent wave*. When light passes through a coupler, as shown in Figure 2.15, a fraction of light is transferred from one fibre to the other and the amount transferred is dependent on the distance between the two cores [128]. When the distance is modulated by pressure, the coupler becomes an evanescent-wave based pressure sensor.

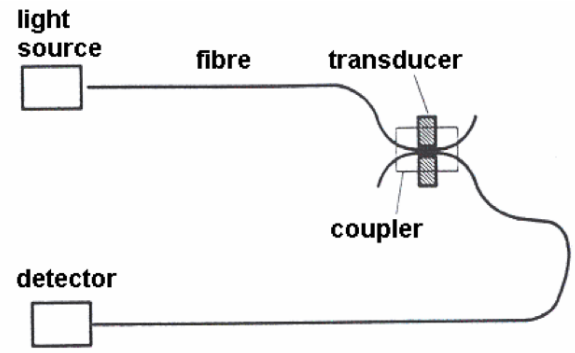

Figure 2.15 Evanescent coupler sensor [128]

Phase Modulated pressure sensors

The most sensitive fibre optic sensing method is based on the optical phase modulation [57]. In the phase modulation sensors, light from a coherent source is split into two and coupled into two single mode fibres. When the two beams recombine, interference occurs. If a physical or chemical parameter perturbs one of the fibres relative to the other, the phase difference between the modulated light and a reference light shifts accordingly.

The phase shift can be detected using an interferometric configuration in order to convert the phase variation into a signal intensity variation. Various interferometers can be used and they are:

- Mach-Zehnder Interferometer (MZI),
- Michelson Interferometer (MI)
- Sagnac Interferometer (SI)
- Fabry-Perot (FP) Interferometer

These are considered below

Mach–Zehnder Interferometer

Several papers have been published describing pressure sensors utilizing Mach- Zehnder interferometers [129]-[133], A fibre Mach-Zehnder interferometer can be realized using either a conventional setup including two-fibre arms or an in-line one-fibre configuration [134]-[136].

Figure 2.16 shows a schematic diagram of a pressure MZI sensor [137] using the conventional layout. The input light is split into two beams using a 50:50 fibre optic coupler and transmitted through two fibres, one being used as reference and the other the sensing fibre. When light guided by the two fibres is recombined by another coupler, interference occurs and the output signal can thus be detected by a detector.

Generally, the sensing arm is fabricated on a diaphragm. Pressure applied on the diaphragm can deform the fibre, thus change the refractive index of the fibre due to the photoelastic effect and this causes the phase shift in output, which can be detected.

J. A. Bucaro *et al*. [134] used this interferometer for acoustic sensing in 1977 but G. B. Hocker [62], was the first to use this technique for pressure measurement in1978

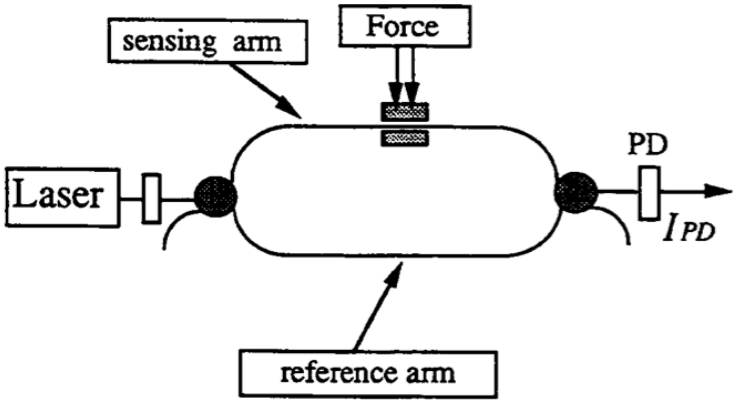

Figure 2.16. Schematic of Mach Zehnder pressure sensor [137]

As indicated above, Mach-zehnder interferometer can also be configured using one fibre, yet with a high sensitivity [138]. Figure 2.17 shows some of such in-line configurations using (a) a pair of LPGs, (b) core mismatch, (c) air-hole collapsing of PCF, (d) MMF segment, (e) small core SMF, and (f) fibre tapering. In these in-line one-fibre Mach Zehnders, the two light beams, split and coupled, are respectively the fundamental core mode and the cladding modes along a single optical fibre. This can be achieved by various means in addition to those shown in Figure 2.17, for example, by mechanically induced two identical long-period fibre gratings (LPGs) inscribed in a photonic crystal fibre (PCF) [140]; by a fibre-taper section between a Long period Grating (LPG) pair [141]; by spliced two pieces of a fibre with a small lateral offset or collapsed air-holes of a single PCF [142]; by two points on a single-mode fibre by CO_2 laser irradiations [143]; by a non-adiabatic taper cascaded with a LPG [144]; two core-offset attenuators on a single-mode fibre [145]; two tandem fibre tapers by fusion splicing [146][147]]; by interaction of a misaligned fusion-spliced point with a LPG on a single-mode fibre [148] and combination of a fibre taper and an ultrafast laser microfabricated spot [149]. In addition, a biconical fibre taper [150], a double-pass Mach-Zehnder interferometer with a gold-coated mirror at the output port of a fibre taper pair [151] and three cascaded single-mode fibre tapers have also been reported [152][153].

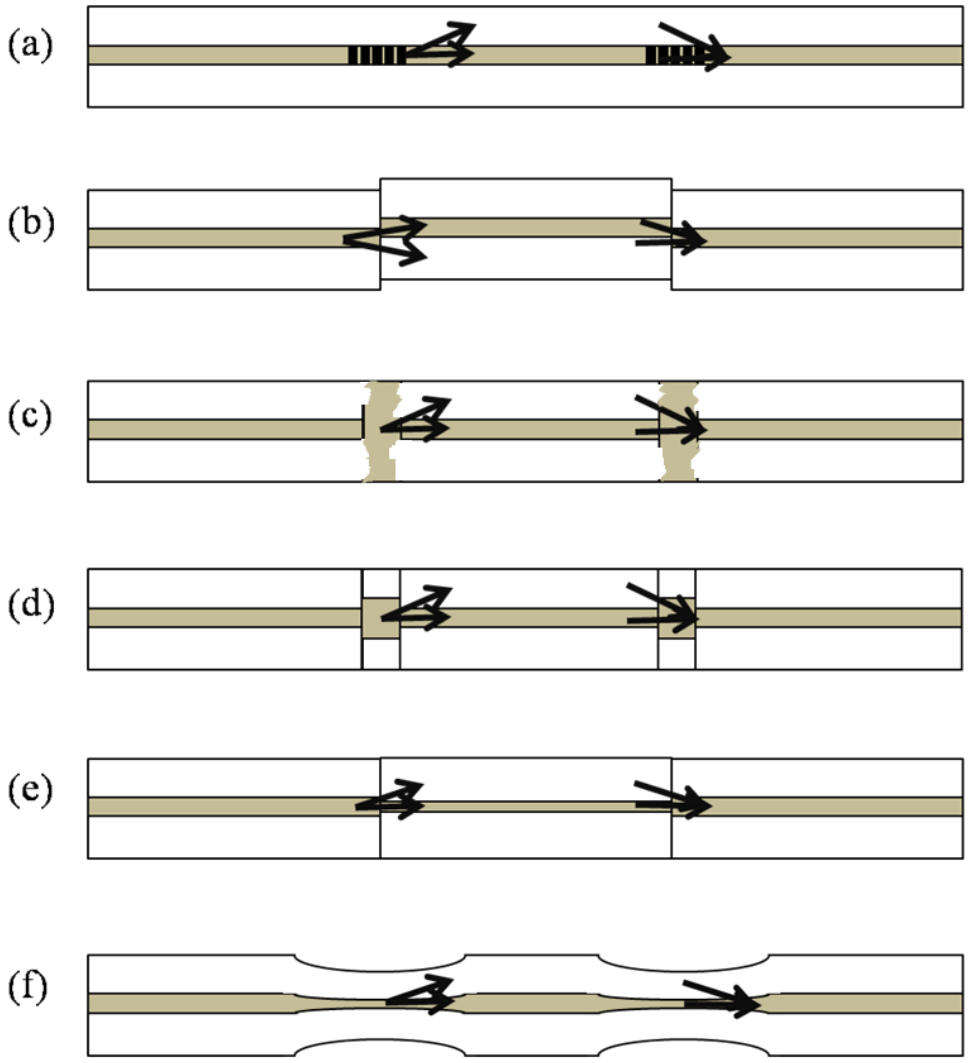

Figure 2.17. Configuration of various types of MZIs; the methods of using (a) a pair of LPGs, (b) core mismatch, (c) air-hole collapsing of PCF, (d) MMF segment, (e) small core SMF, and (f) fibre tapering.[153]

Michelson Interferometer

Another phase modulation configuration for a pressure sensor is the Michelson interferometer (MI). Passy *et.al.* [154] reported the use of an all-fibre MI in which the effects of pressure on mode propagation could be captured through the measurement of the group delays. Bock *et al.* [155] reported on a fibre-optic polarization-sensitive intermodal interferometer for simultaneous measurement of pressure and temperature.

Michelson interferometer pressure sensor configurations are similar to Mach Zehnder Interferometer (MZI) [156]. Figure 2.18 (a) shows a basic configuration of a MI, in which light is split and then combined by a single 1x2 fibre coupler. The light travelling from the source is split into the sensing and reference arms. The light, after traversing the length of the arms, is then reflected back through the same arms by reflectors. The initial coupler then recombines the light from the two arms [156]. Figure 2.18 (b) shows an in-line MI, in which the long period grating acts as a coupler to split and then recombine the core and cladding modes reflected.

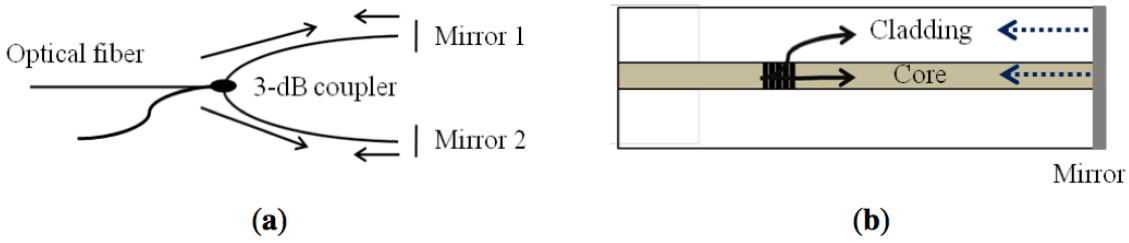

Figure 2.18. (a) Basic configuration of a Michelson interferometer and (b) schematic of an in-line Michelson interferometer. [155]

There are some differences between the Michelson and Mach–Zehnder configurations. The MZI configuration requires two optical fibre couplers while a MI just needs one coupler, but the light passes though both the sensing and reference fibres twice, therefore the optical phase shift per unit length of fibre is doubled [156] for a MI compared to a MZI.

From the practical point of view the physical configuration of the Michelson interferometer is usually easier for sensor packaging due to fewer components needed. However the disadvantage is that the MI sensor configuration is reflective, therefore there is a considerable amount of light reflected back to the input, introducing a significant amount of noise and potential damage of the light source if an isolator is not used [157]. Overall both the simpler configuration (one coupler, fewer splices, etc) and the doubling of the sensitivity per unit length of the fibre make the Michelson interferometer desirable as long as the reflections in the system can be managed properly [156].

MI has also demonstrated the potential of multiplexing multiple sensors through parallel connections of several MI sensors. However, it is essential to adjust the fibre length difference between

the reference arm and the sensing arm of an MI within the coherence length of the light source [158]. An in-line configuration of MI is also possible, with a typical example shown in Figure 2.18 (b).

Sagnac Interferometer

Many researchers recently have paid great attention to Sagnac interferometers (SIs) and their wide range of applications as physical and chemical sensors. They have shown a number of advantages, such as simple ~~in~~ structure, easy fabrication, and environmental robustness [158]-[167]. In general, birefringence fibres such as, high birefringent (Hi-Bi) or polarization maintaining (PM) fibres are chosen as the sensing fibres to increase the sensitivity based on phase-modulation. These fibres are asymmetric and have different refractive index in two axes.

The Sagnac Interferometer is a Fibre Loop Mirror (FLM), which is formed by splicing a birefringent fibre between the two output ports of an optical coupler. As shown in Figure 2.19, the input light is split into two waves that travel with identical optical paths in opposite directions and interference occurs when the two waves re-enter the coupler. This is because two orthogonal polarization modes travel with different speed due to different refractive index.

When an external pressure is applied on the fibre, the phase difference between the two orthogonal polarization modes which are propagating along the birefringent fibre changes. This is due to the change in the propagation constants of polarization modes over a fibre length.

This type has been used in this thesis to monitor the force.

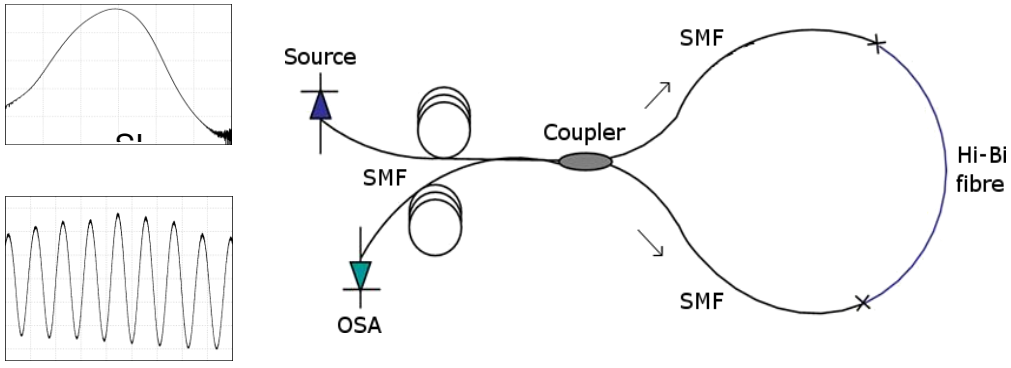

Figure 2.19. Schematic of a sensor based on a Sagnac interferometer. [162]

Sagnac Interferometer has been used for hydrostatic [163][165] and lateral pressure [166][167] measurement with a high sensitivity. Unlike the other fibre optic interferometers discussed, the optical path difference of the Sagnac Interferometer is determined by the difference in the polarization dependent propagating speed of the mode guided along the loop [158]. The mode polarization can be adjusted by a polarization controller (PC) connected to the loop at the beginning of the sensing fibre. The signal at the output port of the fibre coupler is governed by the interference between the beams polarized along the slow axis and the fast axis. However, the sensor is independent of the polarization of the input light [168] and the output signal is periodic with its periodicity being determined only by the length of the birefringence fibre but not the total length of the fibre loop mirror [158]

Conventional birefringence fibres have shown high sensitivities to temperature [169], therefore when they are used for pressure measurement, temperature compensation is required to be taken into account [170]-[175]. In order to overcome this limitation, polarization-maintaining photonic crystal fibres have been considered as an alternative due to their insensitivity to temperature variation. The pure silica-based PCF has already demonstrated thermal robustness and through the optimization of the air-hole configuration in a PCF, a high birefringence can also be achieved [174]-[175].

Fabry-Perot interferometer

One of most widely used fibre optic pressure sensor technologies for pressure measurement is Fabry-Perot (F-P) interferometer [176]-[183]. The first report on fibre Fabry–Perot interferometers appeared in the early 1980s [177]. These sensors have demonstrated the high flexibility due to the small sizes of fibres used and given the pressure ranges concerned [184]. As the Fabry-Perot configuration only needs one fibre, it is usually insensitive to the intensity variation between the measurement and reference fibres.

As shown in Figure 2.20, Fabry-Perot interferometric pressure sensors always include a resonance cavity, consisting of two partial reflectors positioned on either side of a transparent medium. One of the reflectors, or mirrors, is attached to a diaphragm, and the cavity length is allowed to vary with the applied pressure [185]. Interference occurs due to the multiple superposition of both reflected and transmitted beams at two parallel surfaces [186].

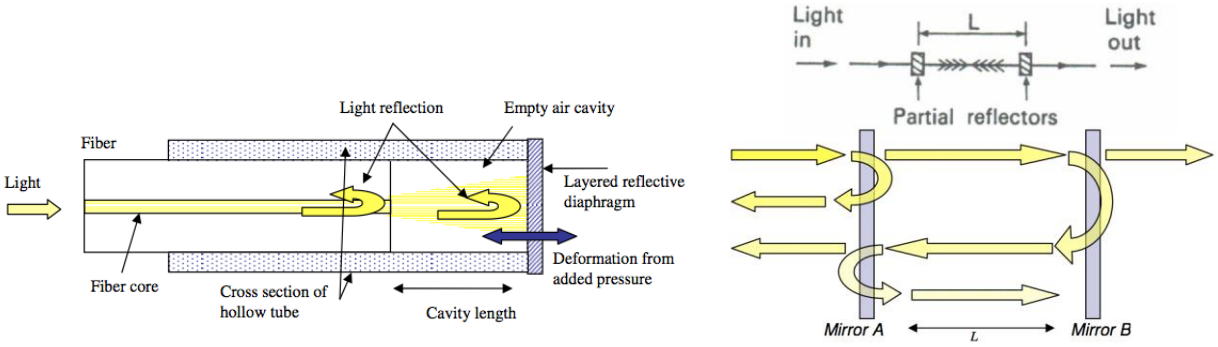

Figure 2.20. Fabry-Perot configuration

Different F-P interrogation techniques are commercially available [177] and differ mainly on the light source: single wavelength or narrow-band light sources produce a periodic pattern shifting with pressure. Although applicable only for relative pressure measurements (since the sensor has to be referenced each time), the interrogation technique [187] patented and commercialized by FISO Technologies [77], is shown to be the best fit for monitoring very fast occurring events such as explosions or blasts [188][189].

FISO Technologies compared to other fibre optic sensing technologies requiring costly optical source or spectral analysis equipment.

The principle behind this patented technology is using white-light interferometry and sketched in Figure 2.21. A continuous broadband light source is first injected and guided into a multimode optical fibre and then into an input of a coupler. Then, the output the light travels through the optical fibre until it reaches its tip, where the F-P is assembled.

The light emerging from the F-P travels back to the interrogator through the optical fibre where, it is redirected to an optical analyser and spread over a Fizeau wedge that reconstructs the interference pattern which is physically recorded using a charge coupled device Charge-coupled device (CCD). Due to the fact that white-light is used, all wavelengths are present, and thus destructive interferences occur except for the zero order where all wavelengths are actually constructive.

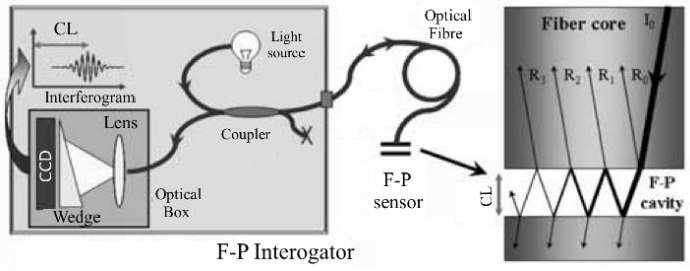

Figure. 2.21: Schematic description of the F-P absolute measurement signal conditioner from FISO Technologies using patented white-light interferometry (left) and detail of F-P sensing interferometer showing ray traces obtained from a selected incident angle light beam propagating in the optical fibre core (right).[77]

The wedge that creates a linear variation of thicknesses can make an interference. This interference pattern has a maximum intensity at the exact position when the optical path difference equals the one created at the F-P sensor, and few lower intensity peaks symmetrically disposed around the central peak (as given by the interferometer cross-correlation function). Thus finding the sensor optical path difference related to the physical parameter to be measured simply consists of finding the position of the maximum peak in the CCD interference pattern. This robust interferometric method allows accurate and precise F-P cavity length measurement with nanometer range precision over several decades of micrometer span, thus giving a very interesting flexible dynamic range.

Intrinsic Fabry-Perot Interferometer Sensor

In intrinsic FPI fibre sensors, reflecting components are contained with the fibre itself [190]. Figure 2.21 shows various intrinsic FPI sensors with their local cavities being formed using various methods such as micro machining [190][194], fibre Bragg gratings (FBGs) [195][196]], chemical etching [197][198], and thin film deposition [199][200]. However, they usually require expensive fabrication facility for the cavity formation.

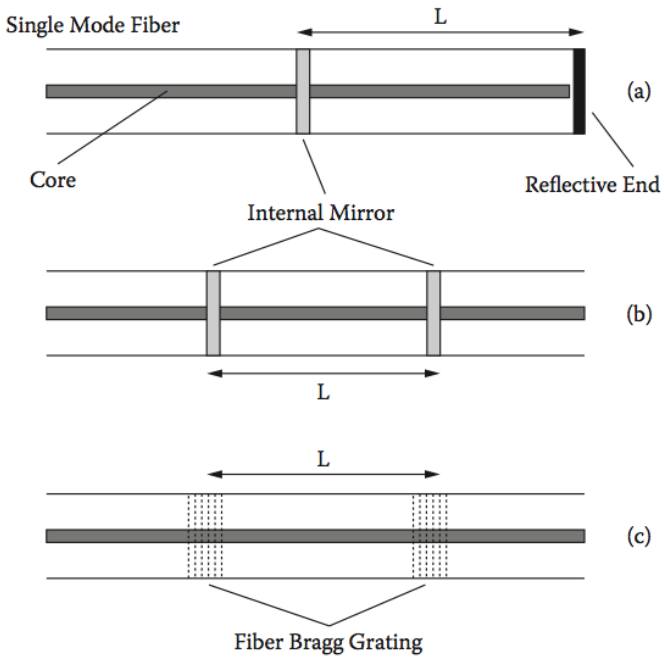

Figure 2.21 Intrinsic Fabry-Perot Interferometer Sensors [178]

Extrinsic Fabry-Perot Interferometer Sensor

Optical fibre Extrinsic Fabry-Perot interferometers (EFPIs) have been widely used as pressure sensors [177]-[181], [201]. Compared to the Mach-Zehnder and Michelson sensors, the EFPI sensor has advantages such as high sensitivity, small size, simple structure, polarization independence, and great design flexibility. Figure 2.22 shows some typical examples of extrinsic Fabry Perot Interferometry sensors.

A typical extrinsic Fabry-Perot interferometer (EFPI) includes a cavity which consists of an air gap between one polished end of a single/multi-mode fibre and the other polished end of a multi-mode fibre or a diaphragm [202]. Both polished ends act as reflectors and the gap between them can be modulated by the pressure applied on one of the reflectors, thus inducing a modulation of the phase difference between the reflected light beams.

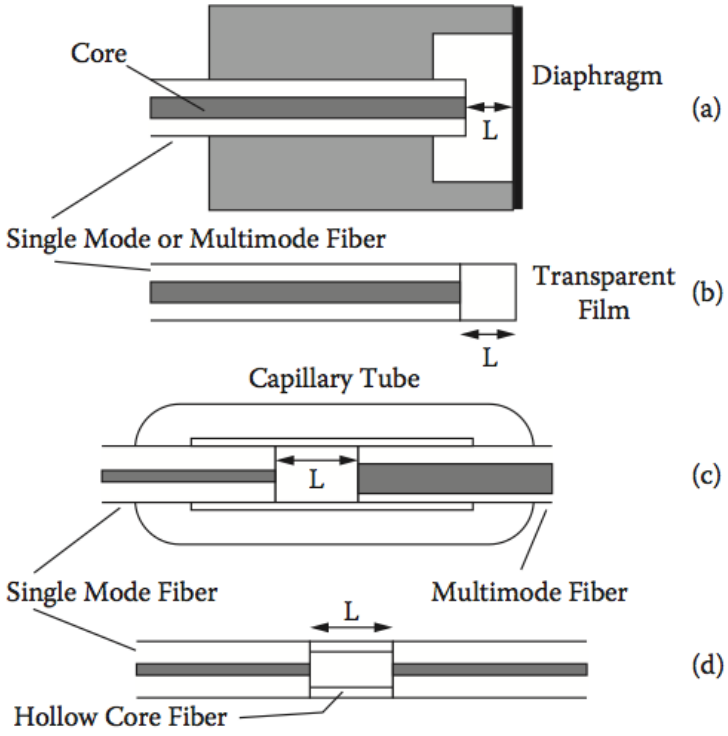

Figure 2.22. Extrinsic Fabry-Perot Interferometer Sensor; a) reflective diaphragm sensor; b) transparent sensor; c) two opposite fibres sensor; and d) hollow core fibre sensor [178]

2.3.3.3 Wavelength Modulation Sensors

In wavelength modulation sensors, the light wavelength is shifted by a perturbation including pressure. The key advantage of this technique is that it is intensity-independent and thus insensitive to environmental perturbation, for example, the source fluctuation, fibre bending, fibre aging etc. Optical fibre wavelength-based sensors include:

- Fibre Bragg Grating
- Fluorescent

These are considered below

Fibre Bragg Grating-based pressure sensors

The most popular and widely used wavelength based sensor is the Fibre Bragg Grating (FBG) sensor [203]. FBGs are formed by periodically modulating the refractive index in the core of a single mode optical fibre. This periodic change in refractive index is normally created by exposing the fibre core to an intense interference pattern of UV light. The variation in refractive index can produce an interference pattern, which acts as a wavelength filter [204]

As shown in Figure 2.23, in the FBG sensor operation the light from a broadband source whose centre wavelength is close to the Bragg wavelength is launched into the fibre. The light propagates through the grating, and part of the signal is reflected at the Bragg wavelength [123]. In fact at the Bragg wavelength, all reflected signals are in phase and add constructively and centred about the Bragg wavelength. Reflected contributions from light at other wavelengths does not add constructively and are cancelled out and as results these wavelengths are transmitted through the grating.

Bragg wavelength is defined by the relationship

$$\lambda_B = 2n_e\Lambda \tag{2.1}$$

where n_e is the effective refractive index of the grating in the fiber core and Λ is the grating period. The effective refractive index depends not only on the wavelength but also (for multimode waveguides) on the mode in which the light propagates.

A perturbation cause shift of Bragg wavelength by changing the effective refractive index and/or the grating period. So FBGs have the capability to measure a number of parameters such as strain, temperature, pressure and chemical parameters [160].

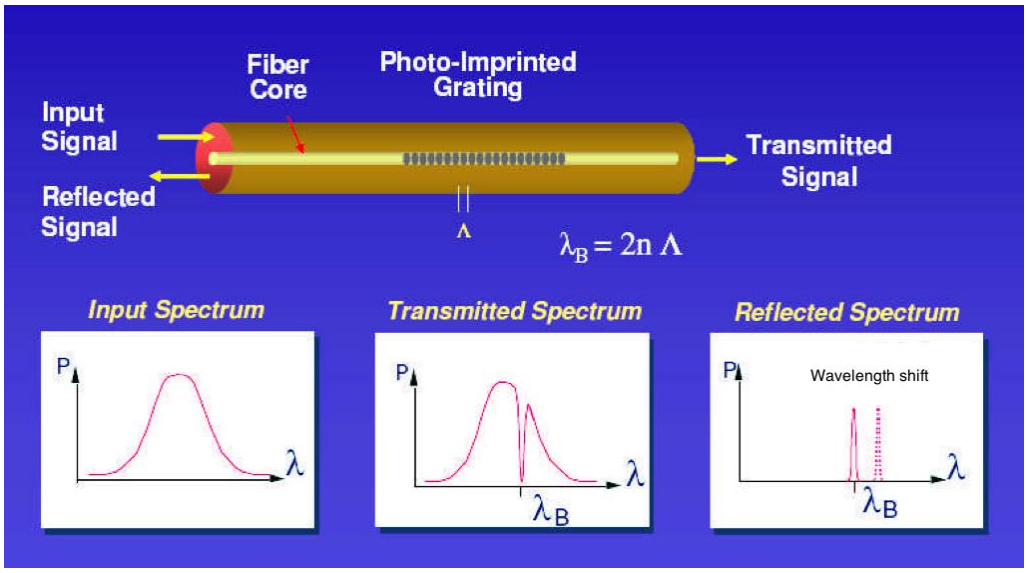

Figure 2.23. Bragg grating schematic and its response to a broadband wavelength source.

FBG was first made in 1978 by Canadian researchers Ken Hill *et al* when they used photosensitive Ge-doped fibre [204] and subsequently by researchers at the Canadian Research Center, United technologies, 3M and several others [205]. Extensive research has been undertaken to explore the sensing capabilities of fibre Bragg grating (FBG) sensors, including their potential for pressure measurement [203]-[213].

M. G.Xu *et al.* [206] were the first to report the use of an optical fibre-grating for pressure measurement using the experimental setup shown in Figure 2.24. In their work, the wavelength of the peak reflection from an in-fibre grating showed a negative shift of 0.22 nm when the FBG was under hydrostatic pressure at 70 MPa.

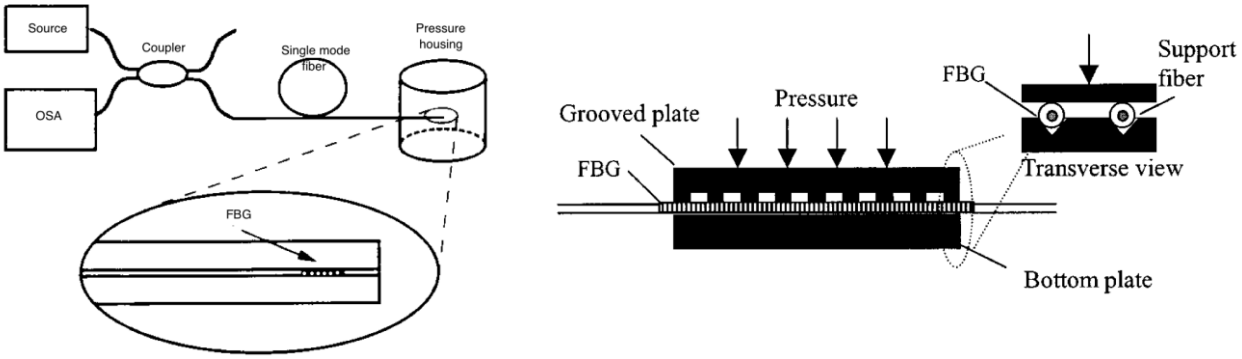

(a) (b)

Figure 2.24 Schematic diagram of FBG (a) hydrostatic and (b) transvers pressure sensor.[206]

In general, the intrinsic pressure sensitivity of a FBG in not very high, as the pressure measurement is undertaken indirectly through the strain measurement along the fibre axis [61]. Two approaches have been used to turn a FBG into a pressure sensor:

a) Attaching the FBG fibre to a flexible diaphragm, as shown in Figure 2.25, either orthogonally or in the diaphragm plane in areas where the strain is maximal [61][208]. In both cases, such designs are always limited to high pressure ranges.

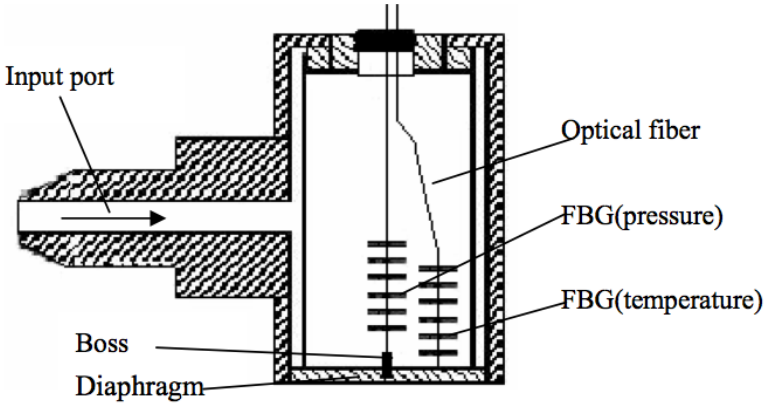

Figure 2.25 Schematic diagram of FBG-based pressure sensors.[61]

b) Another interesting approach is to integrate the FBG sensor into cylindrical assemblies, as shown in Figure 2.26, so that an increased pressure sensitivity can be achieved through mechanical amplification schemes [61][209].

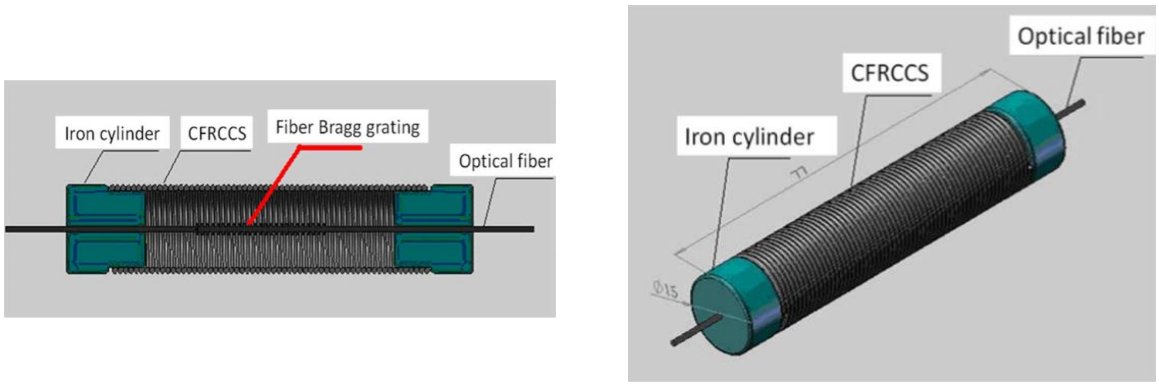

Figure 2.26. Schematic diagram of FBG-based pressure sensors mounted on a cylinder. [209]

FBG pressure sensors have their own advantages and disadvantage. The advantages of this type of pressure sensors include their multiplexing capability, offering the flexibility in sensor design either for single point or multi-point sensing arrays, low cost and the capability in meeting various sensing needs [203][214]. The disadvantages of FBGs are their cross-sensitivities to various parameters, including pressure, strain and temperature.

Fluorescent decay based pressure sensor

Fluorescence occurs when molecules absorb light at one wavelength and then emit light at a longer wavelength [215], as illustrated in Figure 2.27. Since the excitation and emission occur only at distinct energy levels, each fluorescent molecule has a unique fluorescence spectral fingerprint, which is very important for sensor applications .

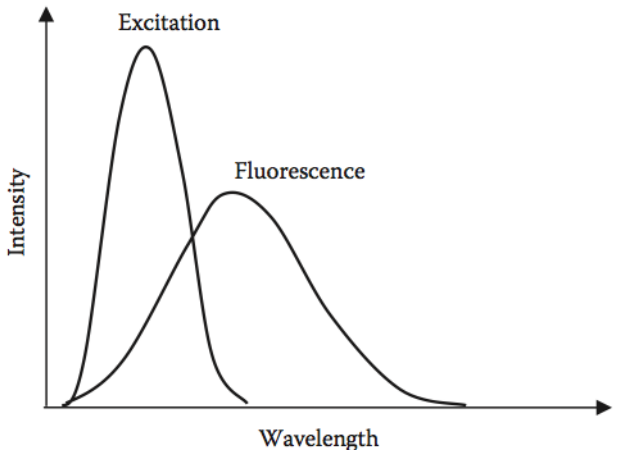

Figure 2.27. An illustration of fluorescent light emission.

Figure 2.28 shows a schematic diagram of a fluorescence decay-based fibre optic pressure sensor. The sensor consists of a single multimode optical fibre which is attached to a diaphragm and two different neodymium-doped glass fluorescent discs characterized by distinct fluorescent decay rates [216].

The end of the fibre is attached to a diaphragm causing the fibre tip to move vertically from one fluorescent disc to another when the diaphragm is deflected with the applied pressure [217].

As the fibre tip is displaced, the relative intensity contribution of each fluorescent disc changes. Phase-sensitive detection methods are then used to determine the relative contributions of each disc, which are proportional to the process variable. The dynamic response of a fluorescent decay-rate sensor is dominated by the fluorescent decay rates of the discs rather than mechanical limits imposed by the diaphragm. Improvements in dynamic response may be possible with the use of other fluorescing material combinations [217],[218]].

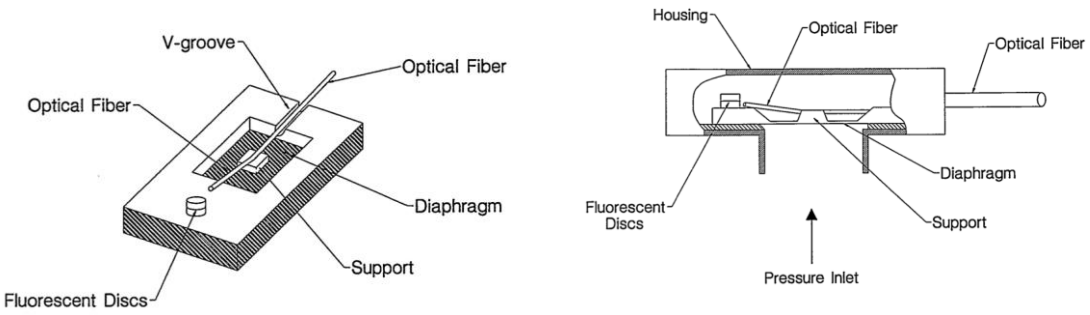

Figure 2.28 Fluorescent Decay-based Pressure Sensor [215]

2.3.3.4 Polarization & refractive index sensors

The development of polarization-modulated fibre optic sensors is based on two different physical effects: the Faraday effect [52] and the photoelastic effect [52][64][219]. Sensors based on the Faraday effect are mainly used to measure electrical or magnetic field with a typical application of the measurement of the electrical current [52][78]

On the other hand, pressure sensor development can be easily based on the photoelastic effect as this directly transfers the applied pressure into the change of the polarization property in an optical medium [60][220]. Although silica glass fibre itself exhibits a very weak photoelastic effect, polarization maintaining (PM) fibres are often used to increase photoelastic effects.

When a transverse pressure is applied on an ordinary single mode optical fibre or a PM fibre, an external birefringence is introduced in them [219],[220]. This induced external birefringence breaks the circular symmetry in ordinary single mode fibres and produces an anisotropic refractive index distribution in the fibre core. On the other hand, there is an initial birefringence in PM fibres, so that the induced birefringence can increase or decrease the overall birefringence, depending on the direction of the transverse pressure applied [220].

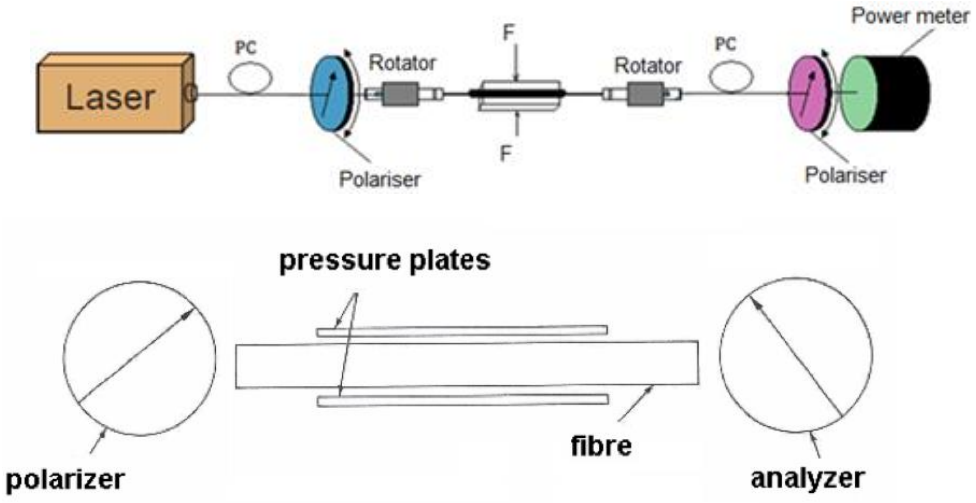

Figure 2.29 Schematic diagram of a polarization modulation-based pressure sensor [220]

Figure 2.29 shows a schematic diagram a typical pressure sensor system using a polarization modulation. The initial polarization state of the light can be rotated as a result of the applied transverse pressure and the change can be captured by the detection system shown in the diagram.

Near Total Internal Reflection (NTIR)

Another polarization modulation-based pressure sensor is the near total internal reflection (NTIR) sensor [101][110]. This sensor, as shown in Figure 2.30, requires only one single-mode fibre, the end of which is polished at an angle slightly smaller than the critical angle. The tip of the fibre is the sensor element, which is subjected to the process pressure. Light travels along the fibre, strikes the polished end, reflects to the mirrored surface, reflects back to the polished end, and is transmitted back along the fibre [221][222]. Process pressure variations cause unequal changes in the refractive indices of the fibre and the surrounding medium. As the refractive indices change, the critical angle shifts. These shifts in the critical angle result in variations in the amount of light reflected back. This sensor configuration possesses the advantage of being very small.

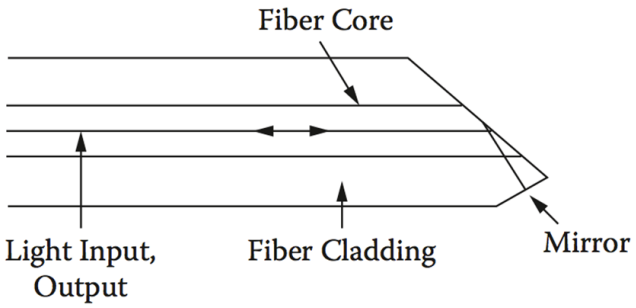

Figure 2.30 Fibre sensor using critical angle properties of a fibre for pressure measurement via measurements of the light reflected back into the fibre.[101]

2.4 Summary

This chapter contains a historical review of the background and basic introduction to conventional and optical fibre pressure sensors. The techniques, designs, advantages and disadvantages of pressure sensors have been reviewed. Also a cross compression has been made between conventional and novel optical fibre pressure sensors.

This chapter will be followed by the theoretical background of transverse pressure sensors in birefringent fibres based on a mode coupling theory in next chapter.

CHAPTER 3

Theoretical background of transverse pressure sensors in birefringent fibres

3.1 Introduction

This Chapter provides a theoretical background for the transverse pressure sensors in birefringent fibres based on mode coupling theory. The Chapter starts with Maxwell's equations which are used to explain fundamental issues such as light propagation and polarization of light and this leads to a simplified geometrical and analytical description of the propagation of light and modes of propagation in optical fibres.

In order to verify the above theoretical description, a detailed calculation of the birefringence of a new non-Symmetric Polarization-Maintaining side-hole fibre with one hole in its cladding is made by using a thermo-elastic displacement potential method through the superposition of sectional displacement potentials. When the birefringent fibre is subjected to transverse pressure, its pressure sensitivity is thus determined theoretically based on its birefringence variation as a function of rotation angles and magnitudes of the applied external force. An interrogation approach using fibre loop mirror is also introduced in this Chapter to measure the phase modulation as a result of the birefringence variation caused by the lateral pressure change.

3.2 Light propagation

Maxwell's equations state the fundamentals of electricity and magnetism and have been used widely to describe all electromagnetic phenomena including light propagation and polarization of light [223].

Maxwell's equations are given by the following equations [224]:

$$\nabla \cdot \mathbf{D} = \rho \tag{3.1}$$

$$\nabla \cdot \mathbf{B} = 0 \tag{3.2}$$

$$\nabla \times \mathbf{E} = -\frac{\partial \mathbf{B}}{\partial t} \tag{3.3}$$

$$\nabla \times \mathbf{H} = \frac{\partial \mathbf{D}}{\partial t} + \mathbf{J} \tag{3.4}$$

where ρ represents the charge density, **J** the current density, and **E**, **D**, **B**, and **H** represent the electric field, electric displacement, magnetic induction, and magnetic field, respectively. The preceding

equations can be solved only if the constitutive relations that relate **D** to **E**, **B** to **H**, and **J** to **E** are known. Normal optical medium is isotropic which means **D** is in the same direction as E. In this case, the constitutive relations are given by [224][225]

$$\mathbf{D} = \varepsilon\mathbf{E} \tag{3.5}$$

$$\mathbf{B} = \mu\mathbf{H} \tag{3.6}$$

$$\mathbf{J} = \sigma\mathbf{E} \tag{3.7}$$

Where ε, μ and σ are as the dielectric permittivity, magnetic permeability, and conductivity of the medium respectively.

If fibres are assumed to be dielectric (charge-free), $\rho = 0$ and $\sigma = 0$ hence, $\mathbf{J} = 0$

After the above simplification of Maxwell's equations, equations (3.5)-(3.7) can thus be expressed as follows

$$\boldsymbol{\nabla}^2\mathbf{E} = \varepsilon\mu\frac{\partial^2\mathbf{E}}{\partial t^2} \tag{3.8}$$

$$\boldsymbol{\nabla}^2\mathbf{H} = \varepsilon\mu\frac{\partial^2\mathbf{H}}{\partial t^2} \tag{3.9}$$

or in general

$$\boldsymbol{\nabla}^2\boldsymbol{\psi} = \frac{1}{v^2}\frac{\partial^2\boldsymbol{\psi}}{\partial t^2} \tag{3.10}$$

where

$$v = \frac{1}{\sqrt{\varepsilon\mu}} \tag{3.11}$$

and ψ is a wave equation in three dimension.

The general solution to equations (3.8) and (3.9) describes a sinusoid of angular frequency:

$$\mathbf{E} = \mathbf{E_0} e^{i(\mathbf{k}.\mathbf{r}-\omega t)} \tag{3.12}$$

$$\mathbf{H} = \mathbf{H_0} e^{i(\mathbf{k}.\mathbf{r}-\omega t)} \tag{3.13}$$

where k and r are wave vector and wavefront position vector respectively, and $\mathbf{E_0}$ and $\mathbf{H_0}$ are complex vectors.

Assume the wave propagation is along z direction, then $\mathbf{k} = \hat{z}k$, where $\hat{z}$ represents the unit vector along the z direction. Thus, $\mathbf{k}.\mathbf{r} = kz$ and

$$e^{i(\mathbf{k}.\mathbf{r}-\omega t)} = e^{i(kz-\omega t)} \tag{3.14}$$

The electric and magnetic field are orthogonal, so equations (3.13) and (3.14) can be expressed as follows.

$$\mathbf{E_x} = \hat{x}E_{0x} e^{-i(kz-\omega t)} \tag{3.15}$$

$$\mathbf{H_y} = \hat{y}H_{0y} e^{-i(kz-\omega t)} \tag{3.16}$$

where

$$H_{0y} = \frac{k}{\omega\mu} E_{0x} \tag{3.17}$$

Figure 3.1 shows a schematic diagram of wave propagation of electric and magnetic fields along z direction.

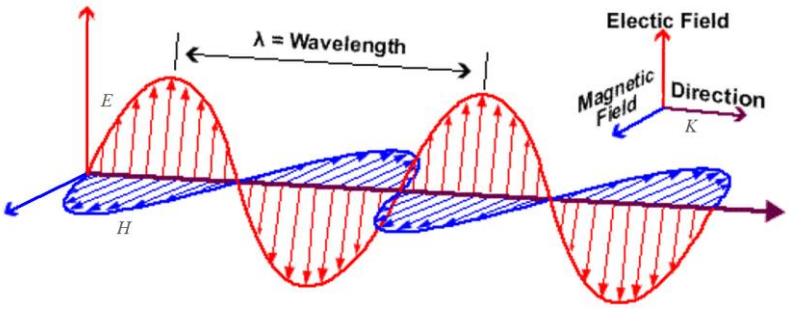

Figure 3.1 Schematic diagram of wave propagation of electric and magnetic fields in z direction (they are not in scale)

The actual electric and magnetic fields are the real parts of the exponentials shown on the right-hand side of equations (3.15) and (3.16) respectively and they can be written as [226]:

$$\mathbf{E_x} = \hat{x}\, E_{0x} \cos(kz - \omega t - \delta_x) \tag{3.18}$$

$$\mathbf{H_y} = \hat{y}\, H_{0y} \cos(kz - \omega t - \delta_y) \tag{3.19}$$

where δ_x and δ_y are arbitrary phase angles. Thus, it is possible to describe this solution completely by means of two waves: one in which the electric field lies entirely in the xz-plane, and the other in which it lies entirely in the yz-plane. If these waves are observed at a particular value of z, say z_0 they take the oscillatory form:

$$\mathbf{E_x} = \hat{x}\, E_{0x} \cos(\omega t + \delta'_x) \qquad \delta'_x = \delta_x - kz_0 \tag{3.20}$$

$$\mathbf{H_y} = \hat{y}\, H_{0y} \cos(\omega t + \delta'_y) \qquad \delta'_y = \delta_y - kz_0 \tag{3.21}$$

and the tip of each vector appears to oscillate sinusoidally with time along z direction. E_x is said to be linearly polarized in the direction x, and E_y is said to be linearly polarized in the direction y.

The tip of the vector, which is the sum of E_x and E_y, describes a generic ellipse whose Cartesian equation in the xy-plane at the chosen z_0 can be given by [226].

$$\frac{E_x^2}{E_{0x}^2} + \frac{E_y^2}{E_{0y}^2} + 2\frac{E_x E_y}{E_{0x}E_{0y}}\cos\delta = \sin^2\delta \tag{3.22}$$

where .

$$\delta = \delta_y' - \delta_x' \tag{3.23}$$

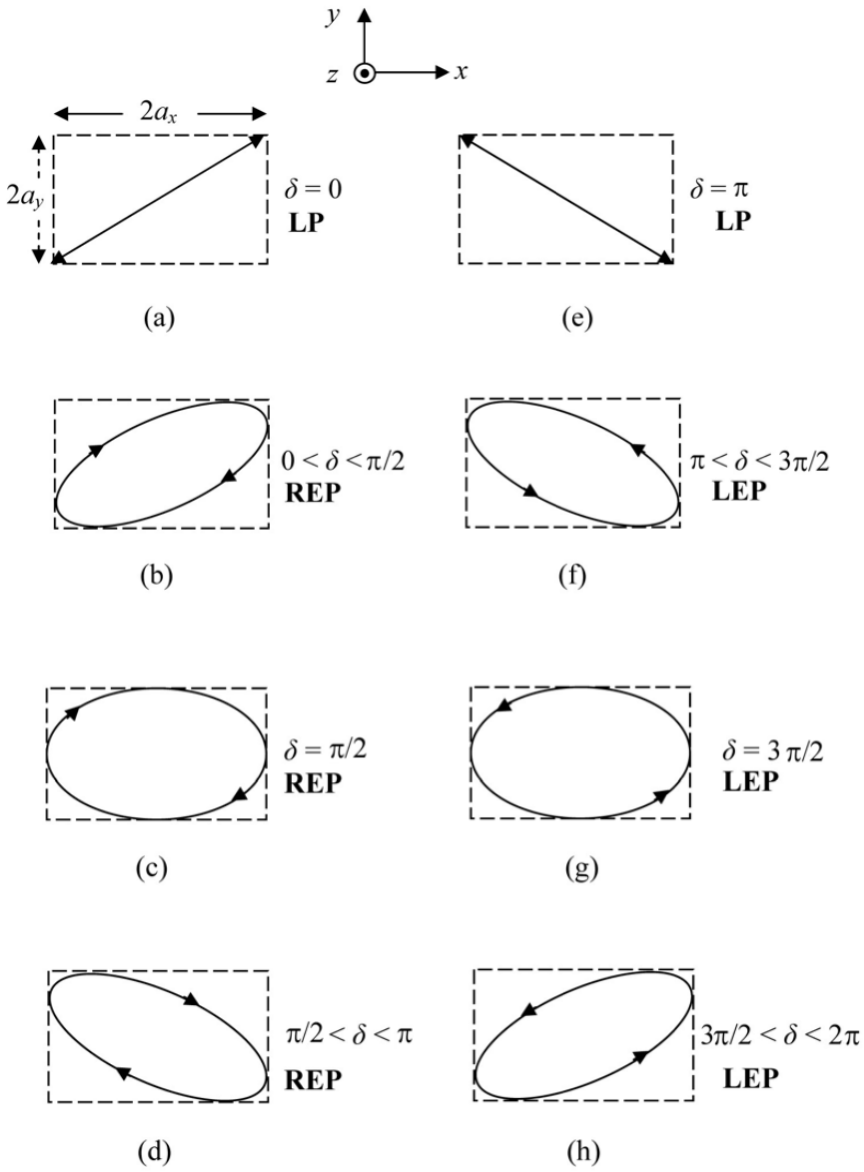

Figure 3.2 polarization states described by equation (3.22) for various values of δ [227].

Thus the *state of polarization* (SOP) of an electromagnetic wave propagating along the z-axis may be ascertained from the path traced by the tip of the electric field vector E in the xy-plane. Three states of polarization can be defined: linear, circular, and elliptical. Figure 3.2 shows polarization states described by equation (3.22) for various values of δ. The wave propagation is along the +z direction [227]. The light is linearly polarized (LP) when $\delta = 0, \pi$, (figure 3.2 (a),(b)), also,when $0 < \delta < \pi/2$ or $\delta = \pi/2$ or $\pi/2 < \delta < 3\pi/2$ the light is Right Elliptical Polarized (REP) (figure 3.2(b),(c) and (d)) and is Left Elliptical Polarized (LEP) when $\pi < \delta < 3\pi/2$ or $\delta = 3\pi/2$ or $3\pi/2 < \delta < 2\pi$ (figure 3-2(f), (g) and (h)). It is obvious that if $E_x = E_y$ the elliptical polarizations convert to circular polarizations

3.3 Light propagating in optical fibres

The wave description of light propagation inside an optical fibre is quite complicated which requires solving equation (3.10) in cylindrical coordinates, as fibres are cylindrical. However as most optical fibres are considered to be weakly guiding ($n_1 - n_2 \ll 1$), the vectorial relationship of the wave equations can be derived directly from the Helmoltz equation below [228]

$$\boldsymbol{\nabla}^2\boldsymbol{\psi}_{r\phi z} + k^2 n^2 \boldsymbol{\psi}_{r\phi z} = 0 \tag{3.24}$$

where r is the radial position, ϕ is the azimuthal position, z is the longitudinal position, $k = \frac{2\pi}{\lambda}$, propagation constant, and $\psi_{r\phi z}$is the wave function in cylindrical coordinates and can be $\mathbf{E}_{r\phi z}$ or $H_{r\phi z}$

With substitute ($\boldsymbol{\nabla}^2 = \frac{\partial^2}{\partial r^2} + \frac{1}{r}\frac{\partial}{\partial r} + \frac{\partial^2}{r^2\,\partial\phi^2} + \frac{\partial^2}{\partial z^2}$) in equation (3.24)

$$\left[\frac{\partial^2}{\partial r^2} + \frac{1}{r}\frac{\partial}{\partial r} + \frac{\partial^2}{r^2\,\partial\phi^2} + \frac{\partial^2}{\partial z^2} + k^2 n^2\right]\psi_{r\phi z} = 0 \tag{3.25}$$

Equation (3.25) is a Bessel a function and can be transformed into Bessel's equation by making the substitution as

$$\boldsymbol{\psi}_{r\phi z} = \boldsymbol{\psi}_r \boldsymbol{\psi}_\phi \boldsymbol{\psi}_z \tag{3.26}$$

or

$$\boldsymbol{\psi}_{r\phi z} = \psi_r e^{-i\upsilon\phi} e^{-i\beta z} \qquad \upsilon = 0, \pm 1, \pm 2, \ldots \tag{3.27}$$

where υ represents the azimuthal mode. The wave function components are illustrated

schematically in Figure 3.6.

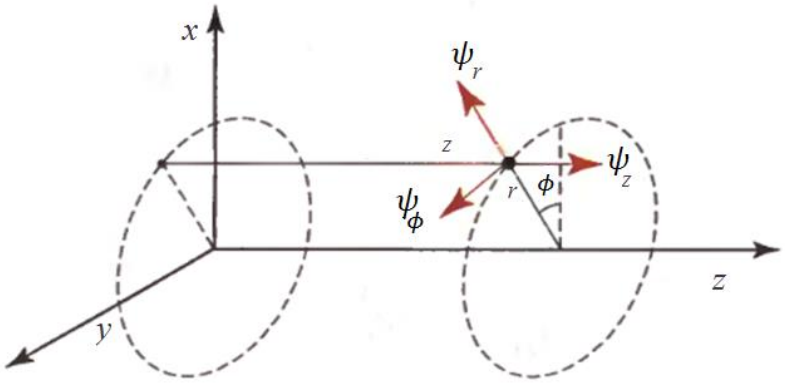

Figure 3.6 schematical diagram of wave function components

Combining equations (3.27) and equation (3.25) leads to the equation below

$$\left[\frac{\partial^2}{\partial r^2}+\frac{1}{r}\frac{\partial}{\partial r}+k^2n^2-\beta^2-\frac{\upsilon^2}{r^2}\right]\psi_r=0 \tag{3.28}$$

The electric field solutions for the core and cladding are Bessel functions with arguments related to the phase constants or wave vector magnitudes of the optical fibre given by [229][230]

$$E_r = AJ_\upsilon(k_1 r)e^{i\upsilon\phi} \qquad r < R \quad (Core) \tag{3.29}$$

$$E_r = BK_\upsilon(k_2 r)e^{i\upsilon\phi} \qquad r > R \quad (Cladding) \tag{3.30}$$

where A and B are constant values, and J_υ and K_υ are the first (ordinary) and second (hyperbolic or modified) Bessel functions of the υth order, and the core and cladding wavevectors k_1 and k_2 are given by

$$k_1 = (k^2n_1^2-\beta^2)^2 \qquad r < R \quad (Core) \tag{3.31}$$

$$k_2 = (\beta^2-n_2^2k^2)^{1/2} \qquad r > R \quad (Cladding) \tag{3.32}$$

k_1 and k_2 determine the rate of change of ψ_r in the core and the cladding respectively

3.4 Modes of optical fibres

The mode of an optical fibre is used to describe the distribution of light energy across the fibre. The precise energy distribution is dependent both on the wavelength of light transmitted and on the core refractive index profile. The exact description of the modes propagating in a fibre is complicated, since it involves six hybrid-field components, i.e. three electrical field components and three magnetic field components, showing a great mathematical complexity [230]. However modes in fibres can be categorized into two major groups considering the difference between electric and magnetic field energy.

The modes with a stronger electric E_z field compared to the magnetic H_z field along the direction of propagation (z-axis) are designated as EH modes [230]. Similarly, those with a stronger H_z field are called HE modes.

The propagating modes are discrete and require identification by two indexes (υ, p) where $(\upsilon = 0, 1, 2, \dots)$ separates the variables in the scalar wave equation, whereas the $(p = 1, 2, 3, \dots.)$ indicates the p_{th} roots of the Bessel function of the first kind J_υ and the modified Bessel function K_υ [227]. So modes can be shown as $HE_{\upsilon p}$ and $EH_{\upsilon p}$

For $\upsilon = 0$, the hybrid modes are analogous to the transverse-electric (TE) and the transverse-magnetic (TM) modes of planar waveguides, and two linearly polarized sets of modes exist that are circularly symmetric with those when either E or H longitudinal field component is zero, i.e. $TE_{0p}(E_z = 0)$ or $TM_{0p}(H_z = 0)$. The lowest-order transverse modes TE_{01} and TM_{01} have cutoff frequencies, $V = V_c = 2.405$ [230]

where V is the normalized frequency and is defined as

$$V = \frac{2\pi}{\lambda} a\sqrt{n_1^2 - n_2^2} \tag{3.33}$$

where a is the core radius, λ the free space wavelength, n_1/n_2 the refractive index of the fibre core/cladding, $\sqrt{n_1^2 - n_2^2} = NA$ the numerical aperture of the fibre used in optics to express the ability of the system to couple light in.

The lowest-order mode of a cylindrical waveguide is the HE_{11} mode, which has zero cutoff frequency [231]. This is the fundamental mode of an optical fibre and is also the only mode propagating in the region at frequencies $< V < 2.405$. Hence, in this region a fibre is considered to be single-mode.

The field distribution E(r, t) corresponding to the HE_{11} mode, has three non-zero components E_x, E_y and E_z (in Cartesian coordinates), among which either E_x or E_y dominates. Even a single-mode fibre is not truly single-mode however, since the electric field of the HE_{11} mode has two polarizations orthogonal to each other that constitute two polarization modes of a single-spatial-mode fibre.

A significant simplification in the description of these modes can be made based on the fact that most of the fibres used for practical applications have core refractive index being slightly higher than that of the surrounding cladding. This corresponds to the weakly guiding approximation, in which a simplified four-component field, instead of six, can be considered [230]. For a weakly guiding fibre ($n_{co} - n_{cl}$), approximate mode solutions are defined as linearly polarized $LP_{\upsilon p}$ modes of different azimuthal υ and radial p mode numbers.

3.5 Birefringence

Normal optical fibres have a cylindrical core and cladding and made of isotopic material so ideally they have no birefringence, therefore polarization state of light will be unchanged during light travelling inside the fibre, as there is no specific direction for a polarization state,

However, real fibres possess a small level of birefringence because in practice there is always a certain amount of mechanical stress or defects arising from manufacturing process which induces a partial loss of circular symmetry of the core cross-section. As a consequence, the polarization of light propagating in the fibre gradually changes in an uncontrolled way. However, in polarization dependent sensors it is important to ensure that the polarization state of the propagating wave is preserved and this can be realized by using anisotropic fibres, i.e. polarization-maintaining (PM) fibres.

Birefringent fibres possess two distinct refractive indices which are dependent on the electric field orientation of the input light into these fibres. The two orthogonal principal axes of these birefringent fibres are described as the fast and slow axes, referring to their respective phase velocity of the light travelling within them. A beam guided in the axis with the higher index (slow axis) will have a lower velocity than a beam at the orthogonal axis (the fast axis) [232]. In these fibres the polarization of light launched into the fibre is aligned with one of the birefringent axes and its polarization state is preserved even if the fibre is bent.

There are two major methods which can be used to introduce permanent birefringence into optical fibres: 1) core modification; 2) the cladding structure modification. In the first method, the core

region characteristics are modified by altering its geometry and this type of birefringence fibres is commonly known as elliptical core fibres. A cross-section of an elliptical core fibre is shown in Figure 3.7 (a) [233].

And in the second method, birefringence can be introduced into the fibre by applying asymmetric stress to the core, which modifies the core refractive index profile. The stress can be introduced by changing the cladding isotropic, making hole/holes or including material(s) with different thermal expansion coefficient in the cladding, thus to change the stress distribution across the core and the cladding. Figure 3.7 shows various types of cross-sectional structures of standard Hi-Bi fibres, either with (a) Elliptical Core; (b) Elliptical Cladding; (c) Elliptical Jacket or cross-sections in the shape of (d) bow-tie; (e) PANDA or (f) D-type.

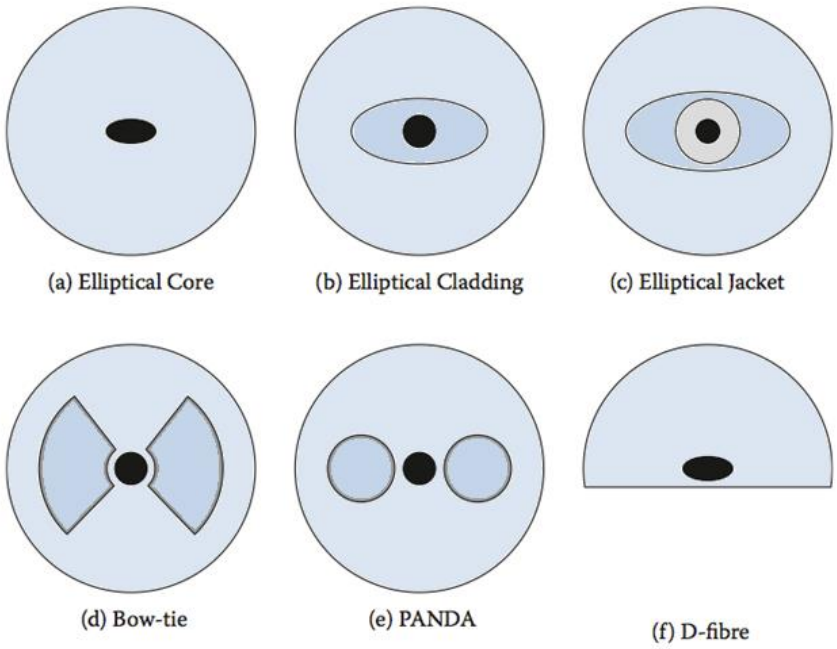

Figure 3.7. Cross sections of conventional polarization maintaining fibres with (a) Elliptical Core;(b) Elliptical Cladding;(c) Elliptical Jacket; cross-sections of (d) bow-tie; (e) PANDA and (f) D-type [233]

Both methods are aimed to ‘disturb’ the circular symmetry of an isotropic fibre, thus inducing the anisotropic refractive index distribution in the core region.

The birefringence of the fibre can be shown as:

$$B = n_s - n_f \tag{3.34}$$

Where n_s and n_f are the refractive index of the slow and fast axis, respectively. Birefringence is usually defined in relation to the fibre beat length L_B, the length of fibre over which the difference in phase shift between the orthogonal polarizations amounts to 2π at a certain wavelength λ [233]:

$$L_B = \frac{\lambda}{B} \tag{3.35}$$

Figure 3.8 shows the beat length, L_B, with the optical phase difference between the two orthogonal polarization states.

If a fibre is subjected to a mechanical perturbation with a period comparable to L_B, a strong power coupling between the two orthogonal polarizations will occur. Therefore, the value of L_B should be smaller than that of the perturbation periods introduced [233].

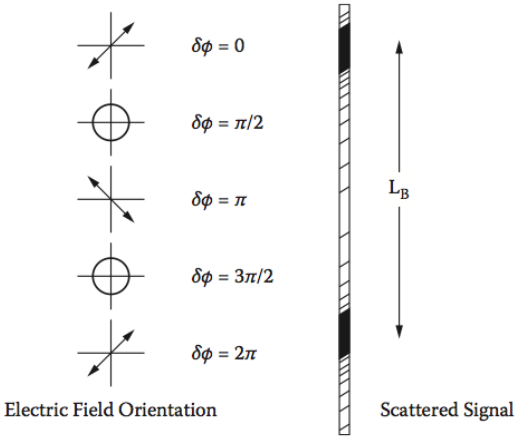

Figure 3.8 Visual determination of the beat length, L_B, with the optical phase difference between the two orthogonal polarization states[233].

3.6 Analysis of the birefringence in a non-symmetric side-hole fibre with one hole

In this section an analytical method is proposed to analyse the birefringence characteristics of one specialist polarization maintaining (PM) fibre containing one side-hole in the fibre cladding. To do so, a Poisson equation is used to determine the stress distribution over the fibre cross-section by using cylindrical coordinates and a displacement potential formulation.

Using this approach, the total stress in the fibre can be obtained through the superposition of the displacement potentials derived from each section of the fibre structure, as the potential is a scalar. When the length of a fibre is sufficiently long (when compared to the fibre diameter), the calculation quantity of stress in the fibre can be considered to be based on an infinite length of cylinder and therefore the three-dimensional strain measurements can be converted into two-dimensional measurements in polar coordinates either by superposing axial axis or by considering the axial strain to be zero if the external force is applied in a direction perpendicular to the fibre axis.

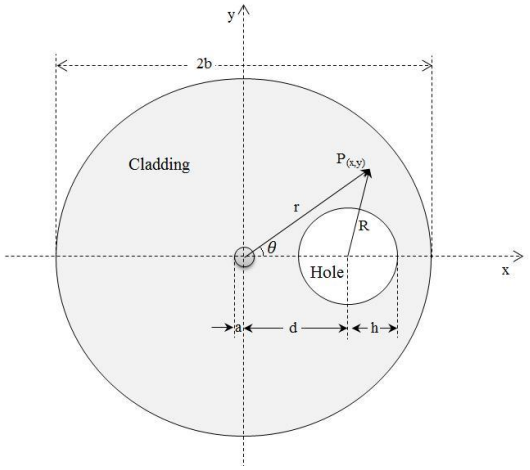

Figure 3.9: One-hole PM fibre which has a core diameter 2a of 8.7 µm and hole diameter 2h of 30 µm. The distance between the right edge of the core to the left edge of the hole, d-a-h, is 9 µm

Figure 3.9 shows a schematic diagram of a PM fibre with one side-hole included in the fibre cladding and the birefringence of the fibre, B, can be determined from [59]

$$B = C(\sigma_x - \sigma_y) \tag{3.36}$$

$$B = C(\sigma_r - \sigma_\theta)\cos 2\theta - 2C\sigma_{r\theta}\sin 2\theta \tag{3.37}$$

where $C = 3.36 \times 10^{-5}$ mm^2/kg is the stress-optic coefficient of fibre, σ_r and σ_θ are stress components in polar coordinates respectively and $\sigma_{r\theta}$ is a shear stress and these parameters can be given by [59]

$$\sigma_r = \frac{-E}{1+\nu}\ \frac{1}{r}\left[\frac{\partial \xi}{\partial r} + \frac{\partial^2 \xi}{r\,\partial \theta^2}\right] \tag{3.38}$$

$$\sigma_\theta = \frac{-E}{1+\nu}\ \frac{\partial^2 \xi}{\partial r^2} \tag{3.39}$$

$$\sigma_{r\theta} = \frac{E}{1+\nu}\ \frac{\partial}{\partial r}\left(\frac{\partial \xi}{r\,\partial \theta}\right) \tag{3.40}$$

where $E = 7830\ kg/mm^2$ and $\upsilon = 0.186$ are Young's modulus and Poisson's ratio respectively. ξ represents a sum of a total thermo-elastic displacement potential φ and Airy stress function A and is given by:

$$\xi = \varphi + A \tag{3.41}$$

The total thermo-elastic displacement potential φ is dependent on the fibre material and shape and is also related to the product $\propto T$ across the fibre cross-section expressed by the Poisson equation [231]

$$\boldsymbol{\nabla}^2\varphi = \gamma_j T\ , \qquad \gamma_j = \frac{1+\nu}{1-\nu}(\alpha_j - \alpha_2)\ \ , j = 1,2,3 \tag{3.42}$$

where index j refers to the region in the fibre, j=1 refers to the fibre core and j=2 and j=3 refer to the fibre cladding and hole respectively. ν is Poisson's ratio and α is thermal expansion coefficient and T= 1650 °C is glass melting temperature.

Through the calculation of Poisson equation (3.42) for each section of the fibre, i.e. fibre core, cladding and hole respectively, each sectional thermo-elastic displacement potential, φ_j, with j referring to the same sectional regions in the fibre as shown in equation (3.42), can thus be described as

$$\varphi_1(r) = \frac{\gamma_1 T}{4} r^2 + K_1 \qquad \text{"inside core"} \quad r \leq a \tag{3.43}$$

$$\Phi_1(r) = \frac{\gamma_1 a^2 T}{2} \ln r + K_2 \quad \text{"outside core"} \quad r > a \tag{3.44}$$

$$\varphi_3(r) = \frac{\gamma_3 a^2}{4} R^2 + K_1' = \frac{\gamma_3 T}{4}(r^2 - 2rd\cos\theta + d^2) + K_1' \qquad \text{"inside hole"} \quad R \leq h \tag{3.45}$$

$$\varphi_3(r) = \frac{\gamma_3 h^2 T}{2} \ln R + K_2' = \frac{\gamma_3 h^2 T}{4} \ln(r^2 - 2rd\cos\theta + d^2) + K_2' \quad \text{"outside hole"} \quad R > h \tag{3.46}$$

where K_1, K_2, K_1' and K_2' are constant values and d is the distance between the centres of the fibre and of the hole and also φ_2 has a constant value.

In this work the Airy function is used to calculate the ξ as expressed in equation (3.41) and it is given by [59]

$$A(r,\theta) = b_0 r^2 + \sum_{n=1}^{\infty}(a_n r^n + b_n r^{n+2}) \cos(n\theta) \tag{3.47}$$

Where Σ denotes summation over all of n ranging from 1 to ∞ and the coefficients a_n and b_n will be determined by using boundary conditions, which can be expressed as

$$\sigma_r = \sigma_{r\theta} = 0 \quad \text{when} \quad r = b \tag{3.48}$$

Based on the boundary conditions in (3.48) and taking into account of the superposed sectional thermo-elastic displacement potentials ($\varphi = \varphi_1 + \varphi_2 + \varphi_3$) illustrated in equations (3.44) and (3.46) and the Airy stress function A, ξ can be expressed as

$$\xi = \frac{\gamma_1 a^2 T}{2} \ln r - \frac{\gamma_3 h^2 T}{2} [\ln \frac{1}{r} + \sum_{n=1}^{\infty} \frac{1}{n} \left(\frac{d}{r}\right)^n \cos(n\theta)] \tag{3.49}$$

In order to obtain the equation (3.49) a Green function is used:

$$\ln\frac{1}{\sqrt{\rho^2+\rho'^2-2\rho\rho'\cos(\omega-\omega')}} = \ln\frac{1}{\rho_<} + \sum_{m=1}^{\infty}\frac{1}{m}\left(\frac{\rho_<}{\rho_>}\right)^m \cos[m(\omega-\omega'] \tag{3.50}$$

$\rho_> = r\,,\ \rho_< = d$

Then

$$\ln(r^2 - 2rd\cos\theta + d^2)^{-1/2} = \quad \ln\frac{1}{r} + \sum_{n=1}^{\infty}\frac{1}{n}\left(\frac{d}{r}\right)^n \cos(n\theta) \tag{3.51}$$

Thus the constant parameters shown in equation (3.47) can be given by

$$b_o = -\frac{T}{4b^2}(a^2\gamma_1 + h^2\gamma_3) \tag{3.52}$$

$$a_n = \frac{\gamma_3 h^2 T}{2}\frac{(n+1)}{n}\left(\frac{d}{b^2}\right)^n \tag{3.53}$$

$$b_n = -\frac{\gamma_3 h^2 T}{2b^2}\left(\frac{d}{b^2}\right)^n \tag{3.54}$$

As a result all the stress equations can be derived, by substituting equations (3.52), (3.53) and (3.54) into (3.47).

As illustrated in equation (3.41), the Airy stress function A and the total thermo-elastic displacement potential φ are independent parameters therefore their respective calculations can be done separately. This indicates that their associated fibre stress components can be calculated separately before being combined to form a total fibre stress. Following this, equations (3.38), (3.39) and (3.40) can be further expanded as follows for the Airy function:

$$\sigma_r^A = \frac{ET}{1+v}\left\{\frac{a^2\gamma_1}{2b^2} + \frac{h^2\gamma_3}{2b^2} + \frac{h^2\gamma_3}{2}\sum_{n=1}^{\infty}\left[(n+1)(n-1)\left(\frac{d}{b^2}\right)^n r^{n-2} - (n+1)(n-2)\left(\frac{d}{b}\right)^n \frac{1}{b^2} r^n\right]\cos n\theta\right\} \tag{3.55}$$

$$\sigma_\theta^A = \frac{ET}{1+v}\left\{\frac{a^2\gamma_1}{2b^2} + \frac{h^2\gamma_3}{2b^2} - \frac{h^2\gamma_3}{2}\sum_{n=1}^{\infty}\left[(n+1)(n-1)\left(\frac{d}{b^2}\right)^n r^{n-2} + (n+1)(n+2)\left(\frac{d}{b^2}\right)^n \frac{1}{b^2} r^n\right]\cos n\theta\right\} \tag{3.56}$$

$$\sigma_{r\theta}^{A} = -\frac{ET}{1+v}\left\{\frac{h^2\gamma_3}{2}\left[\sum_{n=1}^{\infty}(n-1)(n+1)\left(\frac{d}{b^2}\right)^n r^{n-2} - n(n+1)\left(\frac{d}{b^2}\right)^n \frac{r^n}{b^2}\right]\sin\theta\right\} \quad (3.57)$$

Where superscript 'A' refers to Airy function.

Further, results obtained for inside the core are as follows:

$$\sigma_r^{core} = -\frac{ET}{2(1+v)}\left\{\gamma_1 + h^2\gamma_3 \frac{r^2-d^2\cos 2\theta - 2rd\cos\theta}{(r^2-2rd\cos\theta+d^2)^2}\right\} \quad (3.58)$$

$$\sigma_\theta^{core} = -\frac{ET}{2(1+v)}\left\{\gamma_1 - h^2\gamma_3 \frac{r^2+d^2\cos 2\theta - 2rd\cos\theta}{(r^2-2rd\cos\theta+d^2)^2}\right\} \quad (3.59)$$

$$\sigma_{r\theta}^{core} = \frac{ET}{1+v}h^2\gamma_3 d\frac{(r-d\cos\theta)\sin\theta}{(r^2-2rd\cos\theta+d^2)^2} \quad (3.60)$$

And the results obtained for the cladding are as shown:

$$\sigma_r^{Cladding} = -\frac{ET}{2(1+v)}\left\{\frac{a^2\beta_1}{r^2} + \frac{r^2-d^2\cos 2\theta - 2rd\cos\theta}{(r^2-2rd\cos\theta+d^2)^2}\right\} \quad (3.61)$$

$$\sigma_\theta^{Cladding} = -\frac{ET}{2(1+v)}\left\{-\frac{a^2\beta_1}{r^2} + \frac{r^2+d^2\cos 2\theta - 2rd\cos\theta}{(r^2-2rd\cos\theta+d^2)^2}\right\} \quad (3.62)$$

$$\sigma_{r\theta}^{Cladding} = h^2\beta_3 d\sin\theta\frac{(r-d\cos\theta)}{(r^2-2rd\cos\theta+d^2)^2} \quad (3.63)$$

The total stress of the fibre can be obtained by adding all the related stress components together, i.e. σ_r^A and σ_r^{Core} or $\sigma_r^{Cladding}$ for the core or the cladding respectively.

As a result, equations (3.38)-(3.40) can be modified accordingly to be as follows:

$$\sigma_r = \sigma_r^A + \sigma_r^{Core/Cladding} \quad (3.64)$$

$$\sigma_\theta = \sigma_\theta^A + \sigma_\theta^{Core/Cladding} \quad (3.65)$$

$$\sigma_{r\theta} = \sigma_{r\theta}^A + \sigma_{r\theta}^{Core/Cladding} \quad (3.66)$$

Finally the fibre birefringence will be obtained by substitute (3.64), (3.65) and (3.66) into the equation (3.37). The above detailed calculation has been aimed to determine the relationship between the birefringence of a one-hole fibre and several key parameters of the fibre structure, including the size of the hole, the fibre materials, the hole position and the filling material inside the hole.

The fibre design shown in Figure 3.9 was specially chosen for this case study as it has been successfully fabricated by colleagues at ACREO, Sweden. The fibre has a hole diameter (2h) of 30 μm and the distance between the right edge of the core to the left edge of the hole, d-a-h, is 9 μm. The fibre core diameter (2a) is 8.7 μm and the cladding diameter (2b) is 125 μm. $\alpha_1 = 2.125 \times 10^{-6}\ ℃^{-1}$ and $\alpha_3 = 5.4 \times 10^{-7}\ ℃^{-1}$ are core and cladding thermal expansion coefficients respectively. The hole in the fibre is empty i.e. there is no specific material being filled in.

Equations (3.64) and (3.65) are used to calculate the variation of radial stress (σ_r) and circumferential stress (σ_θ) respectively as a function of r with different angle θ and the simulation results obtained are shown in Figures 3.10 and 3.11. Figure 3.10(a) illustrates the stress distribution in a fibre section where the hole is included, i.e. when θ varies from 0° to 30°. Figure 3.10(b) shows the stress condition outside the hole region. Under both circumstances, it is noticed that the radial stress varies with the increase of r but reach smoothly to zero as the radial distance moves towards the fibre boundary.

Figure 3.10 shows the radial stress distribution over the cross section of the fibre. It can be seen the radial stress across the core is slightly different at different angles although the variation is very small from the centre of the core to the edge of core. Figure 3.10 (a) shows that the radial stress decreases with the increase of r until when r is approaching the cladding boundary with the hole where a minimum stress has been observed. The stress profile inside the hole region in Figure 3.10(a) is not shown as, under the simulation conditions, there is no material filling and therefore the stress is zero.

At the cladding/hole boundary, some negative stress has been shown, indicating the region is under compression. In Figure 3.10(b), the radial stress has shown the decrease with the increase of r apart from the region which is affected by the existence of the hole when r scans from θ=30° to θ=45°.

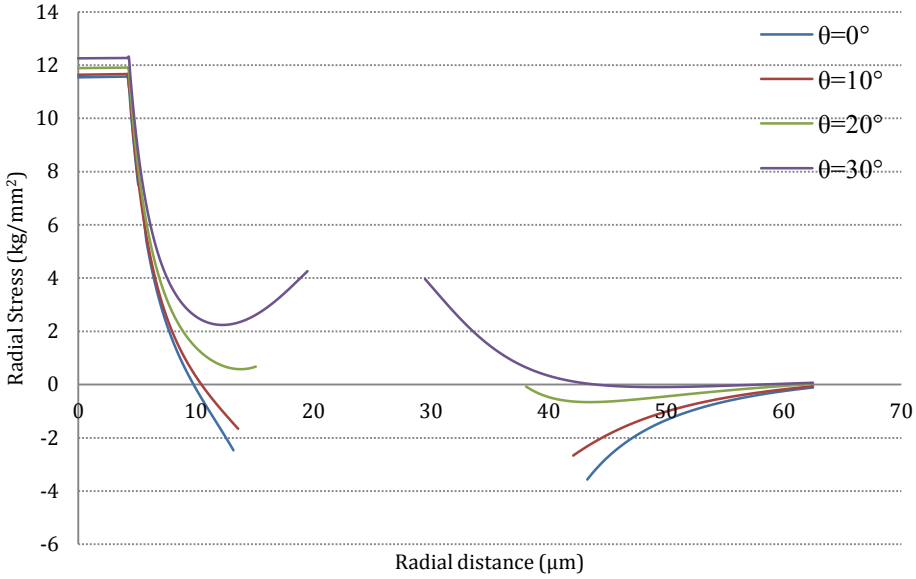

(a)

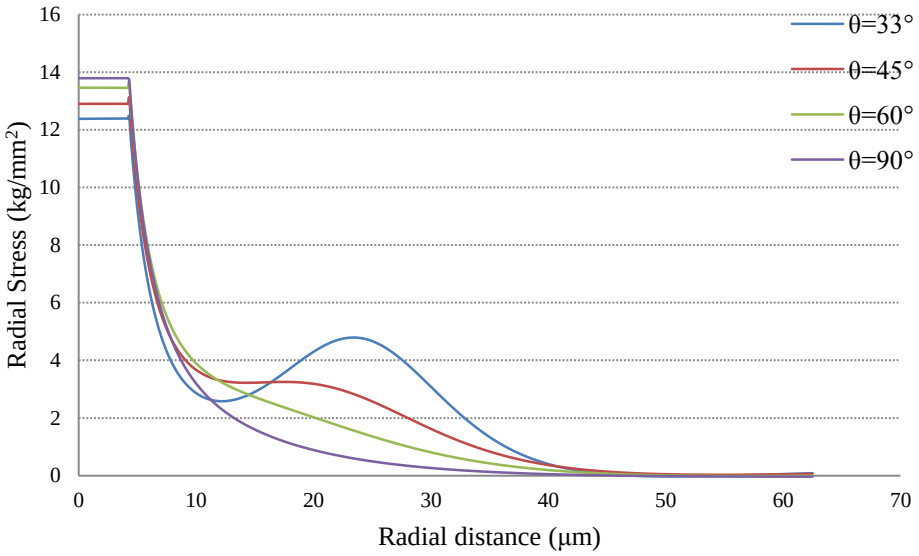

(b)

Figure 3.10. Radial stress distribution in one-hole fibre as a function of radial distance r; (a) radial stress distribution within the fibre cross-section with a hole, i.e. when θ varies from 0° to 30° (b) radial stress distribution within the fibre cross-section outside the hole region when θ varies from 30° to 90°

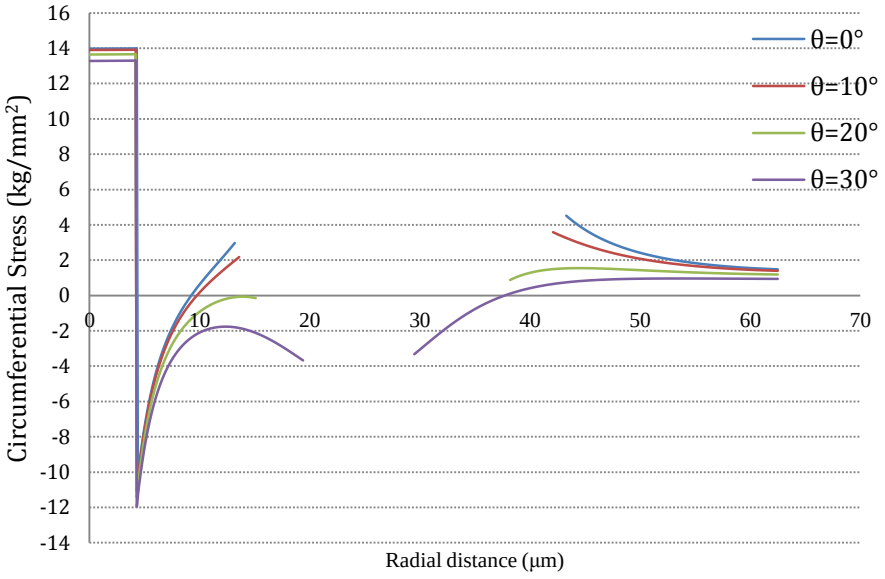

(a)

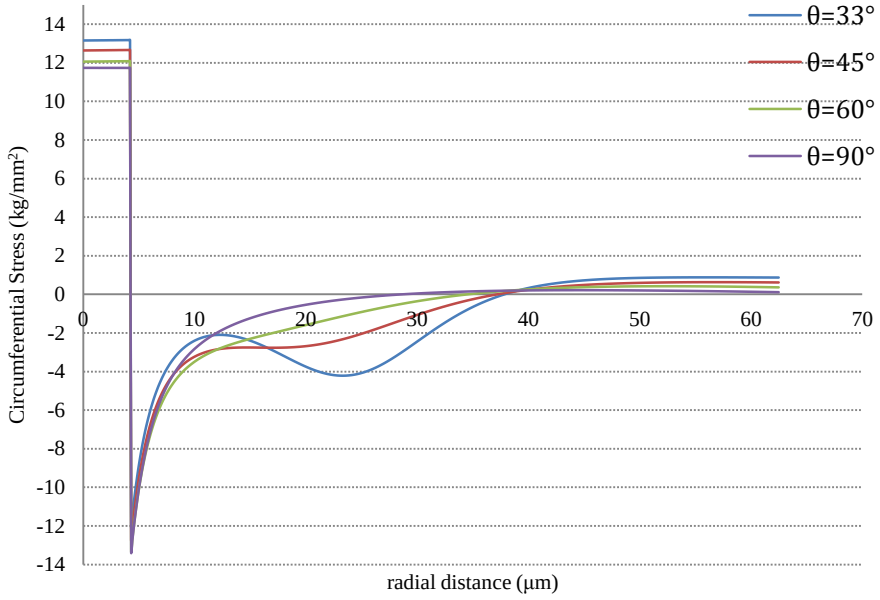

(b)

Figure 3.11. Circumferential stress distribution in a one-hole fibre as a function of radial distance. (a) circumferential stress distribution within the fibre cross-section with a hole, i.e. when θ varies from 0° to 30° (b) circumferential stress distribution within the fibre cross-section outside the hole region when θ varies from 33° to 90°

Figure 3.11 shows the circumferential stress distribution over the cross section of the fibre. It can be seen that the circumferential stress across the core is positive and slightly different at different angles and the change in circumferential stress is small from core centre toward the edge of core. In Figure 3.11(a), it shows the circumferential stress respectively as a function of r with different angles, θ. It is noticeable that all the circumferential stress inside the fibre has been demonstrated to be negative, indicating the compression condition of the fibre. Again in Figure 3.11 (a) a discontinuous profile is demonstrated due to the existence of the hole and the circumferential stress inside the hole is zero.

In Figure 3.11 (b) a decrease of the compression has been observed with the increase of r apart from the region affected by the hole when r scans from θ=33° to θ=45°. As shown in Figure 3.11 (b), in the region where there is no hole, a zero stress can be eventually reached at the edge of the fibre cladding, which is realistic.

Figure 3.12 shows an expanded view of the radial and circumferential stress in the core region for different angles. It is seen that the stresses are fairly constant for different angles.

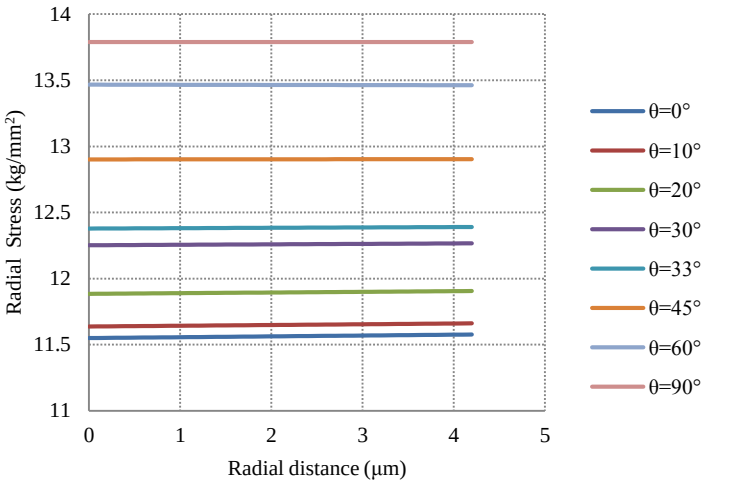

(a)

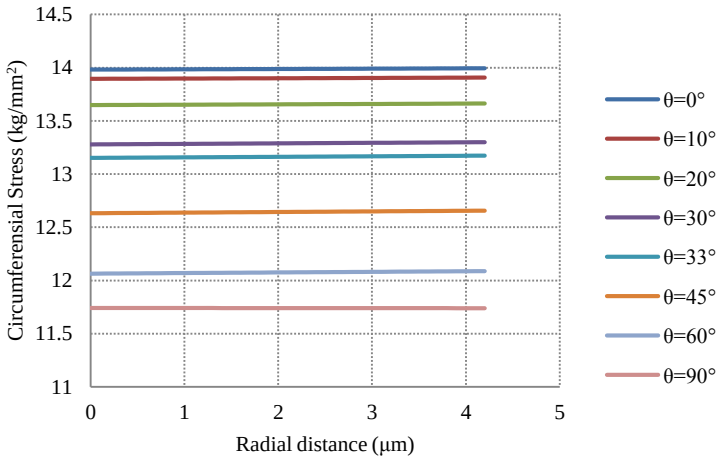

(b)

Figure 3.12 Expanded view of (a) Radial (b) Circumferential stress in core region of Figures 3.10 and 3.11.

Figure 3.13 shows a contour graph indicating the stress distribution across the fibre cladding. It is noticeable that the existence of the hole has changed the stress distribution profile within the fibre cladding. The stress is shown to be negative in some parts (dark blue colour) and positive (light blue) in others, with the maximum stress being near the fibre core.

In this graph stress inside the hole is considered to be zero.

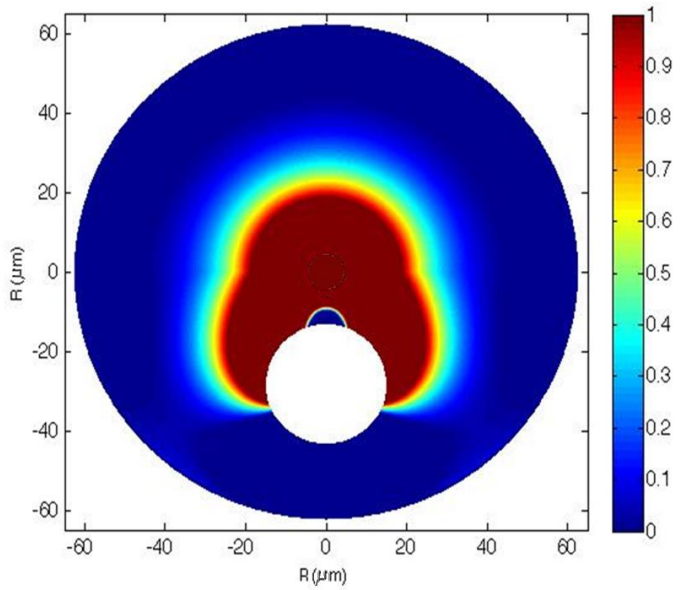

Figure 3.13.Stress distribution across the cladding

Equations (3.64) is used to calculate the variation of radial stress (σ_r) as a function of r with different angle θ in fibre cross section and the simulation results inside the core region is shown in Figures 3.14.

Figure 3.14 shows a contour graph indicating the stress distribution across the fibre core. It is noticeable that the existence of the hole has changed the stress distribution profile within the fibre core.

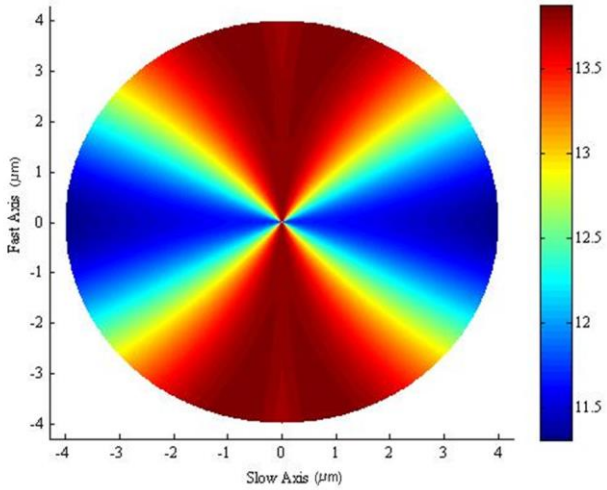

Figure 3.14.Stress distribution across the core

Based upon the above, the fibre birefringence, as shown in equation (3.37), can be obtained. Figure 3.15 (a) and (b) show an expanded view of the birefringence in different directions (a) edge of the core and (b) in the cross section of the core. The stress-induced material birefringence of the fibre core shows birefringence at $\theta = 0^{\circ}$ is maximum (8.2×10^{-5}) then birefringence sinusoidal decrease until it reach to a minimum at $\theta = 180^{\circ}$.

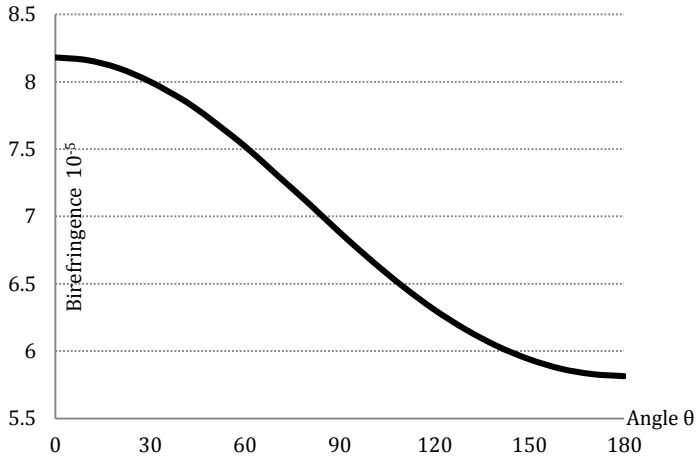

(a)

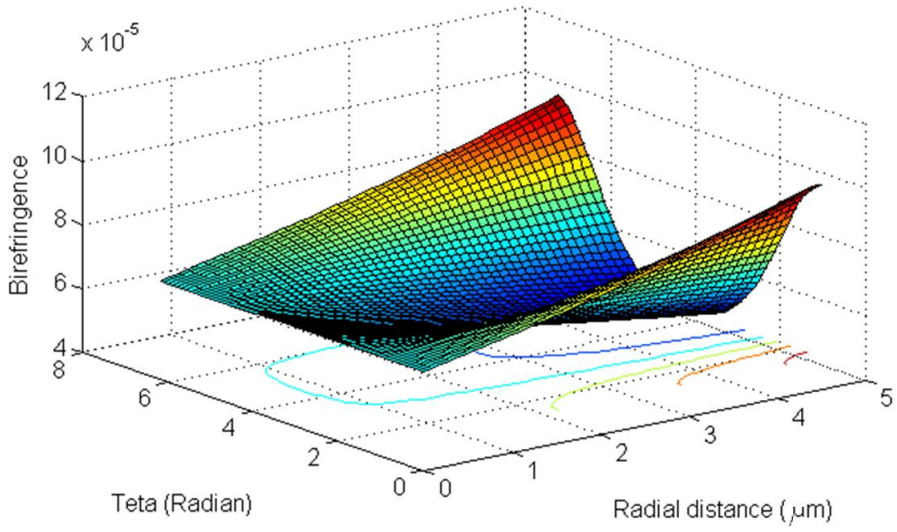

(b)

Figure 3.15.Birefringence distribution in a one-hole fibre core as a function of angles θ . (a) Edge of the core. (b) Cross section of the core

3.7 Mode coupling in Hi-Bi fibres

The dielectric constant ε in equation (3.5) is a tensor. When a polarimetric optical fibre such as that discussed in section 3.7 with a side-hole, suffers from perturbations, the dielectric constant tensor can be split into two parts:

$$[\varepsilon] = [\varepsilon_i] + [\delta\varepsilon] \tag{3.67}$$

where

$[\delta\varepsilon]$ denotes the perturbation tensor in relation to any deformations caused by external perturbation, including force, which is discussed in more detail in the next section. $[\varepsilon_i]$ is a dielectric tensor in an unperturbed system and can be represented by [60]:

$$[\varepsilon_i] = \begin{pmatrix} n_i^2 & 0 & 0 \\ 0 & n_i^2 & 0 \\ 0 & 0 & n_i^2 \end{pmatrix} \tag{3.68}$$

where, n_i denotes the refractive index in an unperturbed system. The deformation can cause coupling modes between two fundamental modes in an anisotropic single mode fibre. So the electromagnetic fields in perturbed systems can be represented as a linear combination of unperturbed system fields by

$$\begin{pmatrix} E \\ H \end{pmatrix} = \begin{pmatrix} e_x & e_y \\ h_x & h_y \end{pmatrix} \begin{pmatrix} A_z e^{i\omega t} \\ B_z e^{i\omega t} \end{pmatrix} \tag{3.69}$$

or

$$\begin{pmatrix} E \\ H \end{pmatrix} = \chi \begin{pmatrix} A_z e^{i\omega t} \\ B_z e^{i\omega t} \end{pmatrix} \tag{3.70}$$

where χ is an eigenfunction in the unperturbed fibre

Both A_z and B_z are field amplitudes and their behaviour can be represented by the simple coupled-mode relationship [234]:

$$\frac{d}{dz}\begin{pmatrix}A_z\\B_z\end{pmatrix} = -i\begin{pmatrix}N_{11} & N_{12}\\N_{21} & N_{22}\end{pmatrix}\begin{pmatrix}A_z\\B_z\end{pmatrix} \quad , \quad i = \sqrt{-1} \tag{3.71}$$

where

$$N_{ii} = \beta_0 + \omega\varepsilon_0 \int e_i^*[\delta\varepsilon]e_j ds \qquad (i = 1,2) \tag{3.72}$$

$$N_{ij} = \omega\varepsilon_0 \int e_i^*[\delta\varepsilon]e_i ds \qquad (i = 1,2; j = 1,2) \tag{3.73}$$

The asterisk indicates complex conjugation, ε_0 is the electric permittivity in vacuum, and ω is the angular frequency. The integrals are performed over the entire fibre cross section and N_{ii} is a Hermitian coupling coefficient matrix.

When a uniform perturbation is applied on to the fibre which is perpendicular to the z direction, e.g. a uniform lateral pressure applied on the PM fibre, N_{ij} is thus independent of z. Equation (3.71) can then be solved by setting $A_z = A_0 e^{-i\beta z}$ and $B_z = B_0 e^{-i\beta_i z}$ where A_0 , B_0 and β are constants independent of z:

$$\frac{d(A_0 e^{-i\beta z})}{dz} = -i(N_{11}A_0 e^{-i\beta z} + N_{12}B_0 e^{-i\beta z}) \tag{3.74}$$

$$\frac{d(B_0 e^{-i\beta z})}{dz} = -i(N_{21}A_0 e^{-i\beta z} + N_{22}B_0 e^{-i\beta z}) \tag{3.75}$$

or

$$A_0\beta = N_{11}A_0 + N_{12}B_0 \tag{3.76}$$

$$B_0\beta = N_{21}A_0 + N_{22}B_0 \tag{3.77}$$

after simplification, the following can be obtained.

$$\Delta\beta = \frac{1}{2}\left((N_{11} - N_{22}) \pm \sqrt{(N_{11} - N_{22})^2 + |2N_{12}|^2}\right) \qquad i = 1,2 \tag{3.78}$$

and

$$\frac{B_0}{A_0} = \frac{2N_{12}}{\left((N_{11}-N_{22}) \pm \sqrt{(N_{11}-N_{22})^2+|2N_{12}|^2}\right)} \tag{3.79}$$

where $\pm$ refers to two different polarization modes and β stands for the propagation constant in the perturbed system [234]. Equation (3.78) shows that the two modes have different propagation constants and equation (3.79) indicates the field amplitude ratio between these two modes.

The propagation constant difference $\delta\beta$ between the two modes as described in equation (3.78) can be further modified to be

$$\delta\beta = \beta_2 - \beta_1 = \frac{1}{2}\left((N_{11}-N_{22}) + \sqrt{(N_{11}-N_{22})^2+|2N_{12}|^2}\right) - \frac{1}{2}\left((N_{11}-N_{22}) - \sqrt{(N_{11}-N_{22})^2+|2N_{12}|^2}\right) \tag{3.80}$$

Or

$$\delta\beta = \sqrt{(N_{11}-N_{22})^2+|2N_{12}|^2} \tag{3.81}$$

In general when the polarization, e.g. elliptically polarized light, is represented by $A_z(z=0) = A_{0z}$ and $B_z(z=0) = B_{0z}$, the polarization state at z can be described as [234]

$$\begin{pmatrix} A_z \\ B_z \end{pmatrix} = \begin{pmatrix} m_{11} & m_{12} \\ m_{21} & m_{22} \end{pmatrix} \begin{pmatrix} A_{0z} \\ B_{0z} \end{pmatrix} e^{-i(\frac{N_{11}+N_{22}}{2})z} \tag{3.82}$$

where

$$m_{11} = \cos\left(\frac{\Delta\beta.z}{2}\right) - i\left(\frac{N_{11}-N_{22}}{\Delta\beta}\right)\sin(\frac{\Delta\beta.z}{2}) \tag{3.83}$$

$$m_{21} = -i\left(\frac{2N_{12}}{\Delta\beta}\right)\sin(\frac{\Delta\beta.z}{2}) \tag{3.84}$$

And

$$m_{12} = m_{21}^* \tag{3.85}$$

$$m_{22} = m_{11}^* \tag{3.86}$$

Both A_{0z} and B_{0z} can be assumed to be complex values. The coefficient matrix m_{ii} is called the

polarization propagation matrix. Also it is unitary because

$$|m_{11}|^2 + |m_{21}|^2 = 1 \tag{3.87}$$

When all the coupling coefficients N_{ii} are real, eigenpolarization modes are linearly polarized with polarization angles [60][234]

$$\gamma = \arctan\left(\frac{2N_{12}}{\left((N_{11}-N_{22})\pm\sqrt{(N_{11}-N_{22})^2+|2N_{12}|^2}\right)}\right) \tag{3.88}$$

with respect to the x axis. Using Cartesian Coordinate representation, eigenpolarization modes become linearly polarized along the x and y directions.

Consider linear polarization incidence with polarization orientation θ_i that is, $A_0 = E_{0x}\cos\theta_i$ and $B_0 = E_{0y}\sin\theta_i$ and when all the values of N_{ii} are real, (3.82) can be reduced to

$$E_x = E_{0x}\left(\cos\theta_i \cos(\delta\beta.\, z/2) - i\cos(\theta_i + \gamma)\sin(\delta\beta.\, z/2)\right)e^{-i\left(\frac{N_{11}+N_{22}}{2}\right)z} \tag{3.89}$$

$$E_y = E_{0y}\left(\sin\theta_i \cos(\delta\beta.\, z/2) + i\sin(\theta_i + \gamma)\sin(\delta\beta.\, z/2)\right)e^{-i\left(\frac{N_{11}+N_{22}}{2}\right)z} \tag{3.90}$$

where $A_z = E_x$ and $B_z = E_y$

And the general form of the output electric can be shown in the matrix form as:

$$\begin{pmatrix} E_x \\ E_y \end{pmatrix} = \begin{pmatrix} \cos\left(\delta\beta.\frac{z}{2}\right) - i\cos\gamma\sin(\delta\beta.\frac{z}{2}) & i\sin\gamma\sin(\delta\beta.\frac{z}{2}) \\ i\sin\gamma\sin(\delta\beta.\frac{z}{2}) & \cos\left(\delta\beta.\frac{z}{2}\right) + i\cos\gamma\sin(\delta\beta.\frac{z}{2}) \end{pmatrix}\begin{pmatrix} E_{0x} \\ E_{0y} \end{pmatrix} e^{-i\left(\frac{N_{11}+N_{22}}{2}\right)z} \tag{3.91}$$

Or

$$\begin{pmatrix} E_x \\ E_y \end{pmatrix} = T_1 \begin{pmatrix} E_{0x} \\ E_{0y} \end{pmatrix} \tag{3.92}$$

Where

$$T_1 = \begin{pmatrix} \cos\left(\delta\beta.\frac{z}{2}\right) - i\cos\gamma\sin\left(\delta\beta.\frac{z}{2}\right) & i\sin\gamma\sin(\delta\beta.\frac{l}{2}) \\ i\sin\gamma\sin(\delta\beta.\frac{z}{2}) & \cos\left(\delta\beta.\frac{z}{2}\right) + i\cos\gamma\sin(\delta\beta.\frac{z}{2}) \end{pmatrix} e^{-i(\frac{N_{11}+N_{22}}{2})z} \quad (3.93)$$

Then coupling coefficient will be:

$$h_{x\to y} = \left|\left((i\sin(\gamma)\sin\left(\delta\beta.\frac{z}{2}\right)e^{-i(\frac{N_{11}+N_{22}}{2})z}) \times (-i\sin(\gamma)\sin\left(\delta\beta.\frac{z}{2}\right)e^{i(\frac{N_{11}+N_{22}}{2})z})\right)\right| \quad (3.94)$$

After the simplification:

$$h_{x\to y} = \sin^2(\gamma)\sin^2\left(\delta\beta.\frac{z}{2}\right) \quad (3.95)$$

3.8 Lateral pressure effect on Hi-Bi fibres

Figure 3.16 shows a single mode side-hole fibre with two equal and transverse forces being applied uniformly in opposite directions and at an angle θ_F with respect to the x axis over the region d, with respect to the x axis.

Assume a Cartesian coordinate system, as shown in figure 3.16, is considered with x (fast axis) and y (slow axis) corresponding to the internal birefringent axes of a polarization-maintaining fibre.

When a linear polarized light (with HE_{11}^{x} and HE_{11}^{y} modes) pass through the perturbed region, the polarization state will be changed.

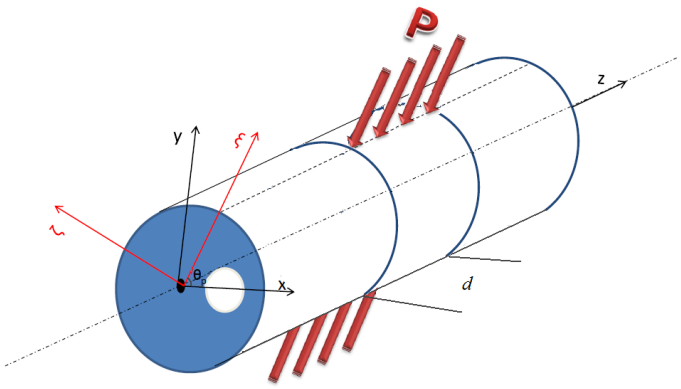

Figure 3.16 a non-symmetric side-hole fibre under pressure

According to equations (3.72) and (3.73), the N_{ii} components, which represent the coupling matrix elements, are related to the deviation of dielectric constant tensor. With the change of the applied pressure, the birefringence, as a sum of initial and external birefringence, of the polarization maintaining fibre changes accordingly. This also leads to the change of slow and fast axes, making the new fast axis being in the applied force direction and the slow axis being perpendicular to the fast axis.

Both the fast and slow axes from x and y directions are rotated by θ_F degrees with respect to the x axis, when they are considered in a $\xi - \zeta$ coordinate system. Therefore the perturbed dielectric constant tensor near the core region can be expressed using the principal stress components induced by the external force [235]:

$$[\delta\varepsilon] = \begin{pmatrix} \delta\varepsilon_\xi & 0 & 0 \\ 0 & \delta\varepsilon_\zeta & 0 \\ 0 & 0 & \delta\varepsilon_z \end{pmatrix} \tag{3.96}$$

where

$$\delta\varepsilon_\xi = 2n_{co}[C_1\sigma_\xi + C_2(\sigma_\zeta + \sigma_z)] \tag{3.97}$$

$$\delta\varepsilon_\zeta = 2n_{co}[C_1\sigma_\zeta + C_2(\sigma_\xi + \sigma_z)] \tag{3.98}$$

$$\delta\varepsilon_z = 2n_{co}[C_1\sigma_z + C_2(\sigma_\xi + \sigma_\zeta)] \tag{3.99}$$

where, n_{co} is the core refractive index, C_1 and C_2 are direct and lateral photoelastic constants. σ_ξ,and σ_ζ, are stress components in the fibre cross section and in the centre of a fibre cross section of radius b, they can be expressed as follows [235]:

$$\sigma_\xi = -3\frac{f}{\pi b} \tag{3.100}$$

$$\sigma_\zeta = \frac{f}{\pi b} \tag{3.101}$$

$$\sigma_z = 0 \tag{3.102}$$

where f is normalized applied force, indicating the amount of force applied in a direction which is vertical to the fiber axis per unit length of fiber.

In the x-y coordinate system, the dielectric tensor is rewritten as

$$[\delta\varepsilon]_{xyz} = R^{-1}[\delta\varepsilon]_{\xi\zeta z}R \tag{3.103}$$

where

$$R = \begin{pmatrix} \cos\theta_F & \sin\theta_F & 0 \\ -\sin\theta_F & \cos\theta_F & 0 \\ 0 & 0 & 1 \end{pmatrix} \tag{3.104}$$

is rotation matrix, so, with substitute (3.104) into (3.103) the dielectric tensor is rewritten as

$$[\delta\varepsilon]_{xyz} = \begin{pmatrix} \delta\varepsilon_x & \delta\varepsilon_{xy} & 0 \\ \delta\varepsilon_{yx} & \delta\varepsilon_y & 0 \\ 0 & 0 & 0 \end{pmatrix} = \begin{pmatrix} \cos\theta_F & -\sin\theta_F & 0 \\ \sin\theta_F & \cos\theta_F & 0 \\ 0 & 0 & 1 \end{pmatrix}\begin{pmatrix} \delta\varepsilon_\xi & 0 & 0 \\ 0 & \delta\varepsilon_\zeta & 0 \\ 0 & 0 & \delta\varepsilon_z \end{pmatrix}\begin{pmatrix} \cos\theta_F & \sin\theta_F & 0 \\ -\sin\theta_F & \cos\theta_F & 0 \\ 0 & 0 & 1 \end{pmatrix} \tag{3.105}$$

thus

$$\delta\varepsilon_x = \delta\varepsilon_\xi\cos^2\theta_F + \delta\varepsilon_\zeta\sin^2\theta_F \tag{3.106}$$

$$\delta\varepsilon_y = \delta\varepsilon_\xi\sin^2\theta_F + \delta\varepsilon_\zeta\cos^2\theta_F \tag{3.107}$$

$$\delta\varepsilon_{xy} = \delta\varepsilon_{\xi}\cos^2\theta_F + \delta\varepsilon_{\zeta}\sin^2\theta_F \quad (3.108)$$

After the brief calculation and substitution equations (3.106)-(3.108) into (3.72)

$$N_{11} - N_{22} = \frac{2\pi}{\lambda}\left[B_i - C\left(\frac{4f}{\pi r}\right)\cos(2\theta)\right] \quad (3.109)$$

$$N_{12} = N_{21} = -\frac{\pi}{\lambda}C\left(\frac{4f}{\pi r}\right)\sin(2\theta) \quad (3.110)$$

so the equation (3.81) can be rewritten by:

$$\delta\beta = \frac{2\pi}{\lambda}\sqrt{\left(B_i - C\left(\frac{4f}{\pi r}\right)\cos(2\theta)\right)^2 + \left|-C\left(\frac{4f}{\pi r}\right)\sin(2\theta)\right|^2} \quad (3.111)$$

When there is no force (f=0) then equation (3.111) will be

$$\delta\beta = \frac{2\pi}{\lambda}B_i \quad (3.112)$$

3.9 *Evaluation of a high birefringence single mode optical fibre as a pressure sensor*

This section is focused on a detailed investigation of the potential of using birefringent optical fibres for pressure monitoring. The approach builds on a theoretical analysis of the birefringence change, i.e. polarization coupling between the two polarization modes inside the PM fibre, as a function of the applied force or pressure.

To interrogate the birefringence variation, the fibre loop mirror (FLM) approach, which is one of the most widely accepted schemes for the interrogation of the changes in the fibre birefringence [164][236], is used in this work. It possesses unique advantages offered, such as low insertion loss, polarization independence to input light, broad spectral bandwidth and high resistance to environmental changes, due to the fact that the two optical waves propagate through identical paths. In addition, the extinction ratio of the system can be controlled using a polarization controller (PC) within the loop.

To make the analysis more generic, the Hi-Bi fibre configured using a FLM is divided into two sections, with one being free from force/pressure (section 1 as shown in Figure 3.17) and the other under force/pressure (section 2 in Figure 3.17). Thus the analysis of each section can be considered separately. This approach can be extended and used for a situation where two different fibres with different birefringence are connected together.

The experimental setup, as illustrated in Figure 3.17, comprises, a broadband light source (SLED) and a 3dB coupler, which splits the input signal into two waves that counter-propagate along completely identical paths. The interference pattern generated as a result could then be monitored using an Optical Spectrum Analyser (OSA) and the pressure sensitivity of the fibre used can be analyzed using Jones matrix algebra.

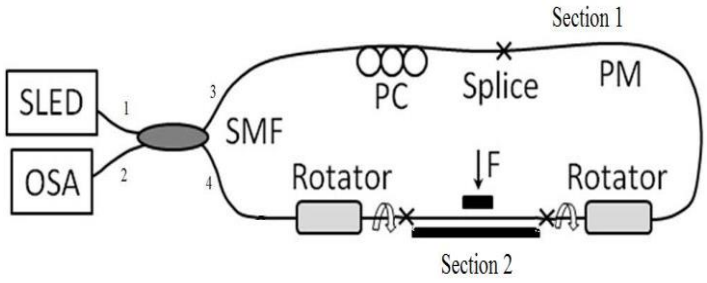

Figure. 3.17 Schematic of the experimental setup used in this investigation.

In the analysis it is assumed that the electric field of the input light at port 1 (as shown in figure 3.17) of the coupler is given by:

$$E_{in} = \begin{pmatrix} E_{xin} \\ E_{yin} \end{pmatrix} \tag{3.113}$$

where E_{in} is electric field of input light signal and E_{xin} and E_{yin} are its components in the x and y directions respectively.

As a result, the electric field component of the light in ports 3 and 4 (E_3 and E_4) of the coupler shown in figure 3.17 is be given as follows, making the reasonable assumption that the coupling ratio between ports 3 and 4 is 50:50, then

$$E_3 = \frac{1}{\sqrt{2}} E_{in} \quad \text{and} \qquad E_4 = \frac{1}{\sqrt{2}} H E_{in} \tag{3.114}$$

where H is the phase delay matrix introduced when the light propagates along the cross arm of the coupler from port 1 to port 4 and this can be given by:

$$H = \begin{pmatrix} e^{i\pi/2} & 0 \\ 0 & e^{i\pi/2} \end{pmatrix} \tag{3.115}$$

The transfer matrices of the clockwise, M_c, and anticlockwise, M_a, beams when they propagate during a round trip before recombining at the coupler, can be written as [237]

$$M_c = R_3 T_2 R_2 T_1 R_1 \quad \text{and} \quad M_a = R_1^{-1} T_1 R_2^{-1} T_2 R_3^{-1} \tag{3.116}$$

where, the term R_i and R_i^{-1} in the equation denote the rotation matrices of the polarization state in each section where the rotation is through an angle φ_i (where i = 1, 2 or 3), when the clockwise and anticlockwise propagating light passes through from one return to another, thus.

$$R_i = \begin{pmatrix} \cos\varphi_i & -\sin\varphi_i \\ \sin\varphi_i & \cos\varphi_i \end{pmatrix}, \qquad i = 1,2,3 \tag{3.117}$$

$$R_i^{-1} = \begin{pmatrix} \cos\varphi_i & \sin\varphi_i \\ -\sin\varphi_i & \cos\varphi_i \end{pmatrix} \qquad i = 1,2,3 \tag{3.118}$$

and T_1 (which has been calculated and shown in equation (3.93)) and T_2 denote the phase delay matrices in first and second sections respectively.

Further T_2 indicates the phase delay matrix induced by the second section of the Hi-Bi fibre, which is under the influence of a pressure or force and T_1 indicates the phase delay in the first section and can be calculated by considering f=0 in equation (3.93)

$$T_2 = \begin{pmatrix} \cos\left(\delta\beta.\frac{L_2}{2}\right) - i\,\sin\left(\delta\beta.\frac{L_2}{2}\right) & 0 \\ 0 & \cos\left(\delta\beta.\frac{L_2}{2}\right) + i\sin(\delta\beta.\frac{L_2}{2}) \end{pmatrix} e^{-i(\frac{N_{11}+N_{22}}{2})L_2} \tag{3.119}$$

$$T_2 = \begin{pmatrix} e^{-i\frac{2\pi}{\lambda}B_i\frac{L_2}{2}} & 0 \\ 0 & e^{i\frac{2\pi}{\lambda}B_i\frac{L_2}{2}} \end{pmatrix} e^{-i(\frac{N_{11}+N_{22}}{2})L_2} \tag{3.120}$$

$$T_2 = A\begin{pmatrix} 1 & 0 \\ 0 & e^{i\frac{2\pi}{\lambda}B_i L_2} \end{pmatrix} \tag{3.121}$$

where $A = e^{-i\left[\left(\frac{N_{11}+N_{22}}{2}\right)-\frac{\pi}{\lambda}B_i\right]}$, B_i is initial Hi-Bi fibre birefringence and L_2 is the length of this part of Hi-Bi fibre (the first section), n_s and n_f are the refractive indices of slow (s) and fast (f) light propagation, respectively and λ is the wavelength used.

After the clockwise and anticlockwise beams interfere at the coupler, the amplitude of the electrical field component light at ports 1 and 2 may be written as [237]

$$P_{1out} = \frac{1}{2}(HR_3T_2R_2T_1R_1 + R_1^{-1}T_1R_2^{-1}T_2R_3^{-1}H)E_{in} \tag{3.122}$$

$$P_{2out} = \frac{1}{2}(R_3T_2R_2T_1R_1 + HR_1^{-1}T_1R_2^{-1}T_2R_3^{-1}H)E_{in} \tag{3.123}$$

Here the transmitted light intensity detected at ports 1 and 2 is then given respectively by

$$I_{1out} = P_{1out}^{*}.P_{1out} \tag{3.124}$$

$$I_{2out} = P_{2out}^{*}.P_{2out} \tag{3.125}$$

and the transmission spectrum at port 1 and port 2 will be given by

$$T_1 = \frac{I_{1out}}{I_{in}} \tag{3.126}$$

$$T_2 = \frac{I_{2out}}{I_{in}} \tag{3.127}$$

Thus T (the transmission equation 3.127) can be calculated by combining equations (3.111), (3.123) and (3.125):

$$T = -4\sin(\varphi_1 + \varphi_3)^2\left(\sin\frac{2\pi}{\lambda}\left(\frac{L_1B}{2} - L_2[B - C\left(\frac{4f}{\pi r}\right)\cos(2\theta)]\right)^2 - 1\right) \tag{3.128}$$

where the angle φ_2 is considered to be zero, which means that two sections of fibres are connected along the same birefringence direction. However, when a joint fibre with two different PM

fibres being connected together, a polarization controller is required to be used to eliminate the angle with π shift.

Equation (3.128) describes clearly the relationship between the output signal from the sensor (Section 2 of the PM fibre) obtained by using the FLM technique and the pressure applied to the section. This arises because the perturbation, f, can cause a polarization mode coupling variation, leading to a change in the phase difference of the polarization modes, which can be monitored using an Optical Spectrum Analyser (OSA).

Figure 3.18 shows the transmission spectra as a function of applied force, calculated based on equation (3.128) and assuming the following parameters: $\lambda = 1550\ \text{nm}, \theta = \pi/4$, $L_1 = 400\ \text{mm}, L_2 = 45\ \text{mm}, \varphi_1 = \varphi_2 = \pi/4$ and the typical value of photoelastic constant for fused silica is considered to be $C = 3.44 \times 10^{-12}\ \text{m}^2/\text{N}$ [60]. The force applied on section 2 is increased in steps over the range from 0 to 10 N. Equation (3.128) also indicates that the light transmitted at port 4 of the FLM is dependent on both the magnitude and direction of the force and the birefringence of the fibre.

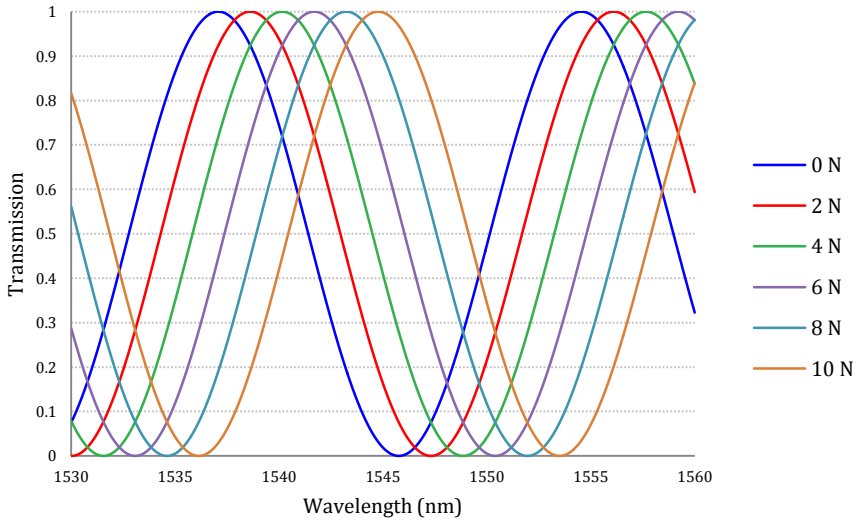

Figure 3.18 Transmission spectra of the fibre when it is exposed to a different transverse force ranging from 0 to 10 N

Figure 3.19 shows the wavelength shift from the initial situation, at a wavelength around 1550nm, as a function of the fibre length when a constant force of 2 N is applied over a length of 45 mm on to two different types of fibres used, i.e. Hi-Bi PCF and Panda fibres, with B $= 3.80 \times 10^{-4}$ and B $= 1.45 \times 10^{-3}$ respectively. The overall fibre length is varied over the range from 0 to 50 m.

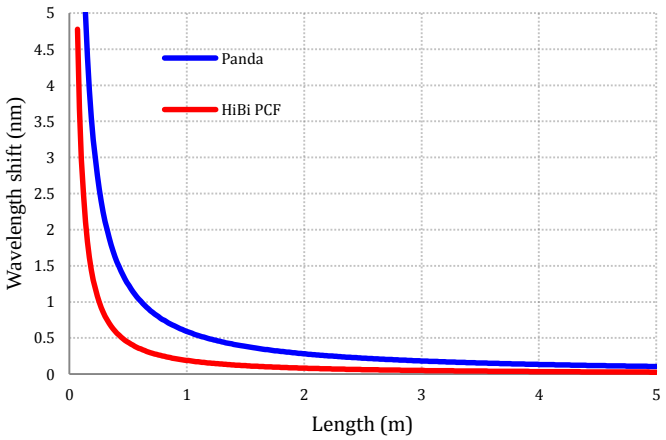

Figure 3.19. Wavelength shifts from a base wavelength around 1550nm as a function of fibre length when a constant load is applied on to two different types of Hi-Bi PCF and Panda fibres with $B = 3.80 \times 10^{-4}$ and $B = 1.45 \times 10^{-3}$ respectively and the overall PM fibre length is varied from 0 to 5 m. The applied weight was 2N over a fibre length of 45 mm

3.10 Summary

The simulation results obtained have shown both a stress distribution inside the asymmetrical fibre (one hole) as well as birefringence in the fibre core. In most cases asymmetric fibres may demonstrate similar characteristics to symmetrical fibres when there is no external perturbation, in this case the birefringence of the fibre calculated to be 8.2×10^{-5} for the single mode with one hole.

This was followed by a theoretical of transverse pressure sensors in birefringent fibres based on a mode coupling theory. A new approach of fibre loop mirror as a technique of phase modulation for

measuring the lateral pressure and potentially for joint fibre is expanded. To underpin the design process, the sensitivity of several different Hi-Bi fibres to transverse pressure has been analysed theoretically using a fibre loop mirror (FLM) configuration and using mode-coupling theory in high birefringence fibres. The theory has enabled a description of the transmitted light intensity of the FLM when a lateral pressure is applied to selected fibres of different type and length with the key sensor parameters being fibre length, fibre birefringence (and thus fibre type) and the effect of the direction of lateral pressure.

The analysis has shown that the relation between the length and sensitivity is downward quasi-hyperbolic so shorter fibre length can increase the sensitivity dramatically, and that fibres with higher birefringence have lower sensitivity.

CHAPTER 4

Experimental evaluation of polarization maintaining fibres for stress/force measurement

4.1 *Transverse force sensitivity of one and two side hole(s) fibres*

This section is focused on the evaluation of the lateral pressure sensitivity of two types of side-hole(s) fibres, shown in Figure 4.1, as a function of the angle and magnitude of the external transverse force applied. Based on the cross-comparison of the results obtained from these two different structured side-hole fibres, discussions and conclusions are made in terms of their respective sensing potential.

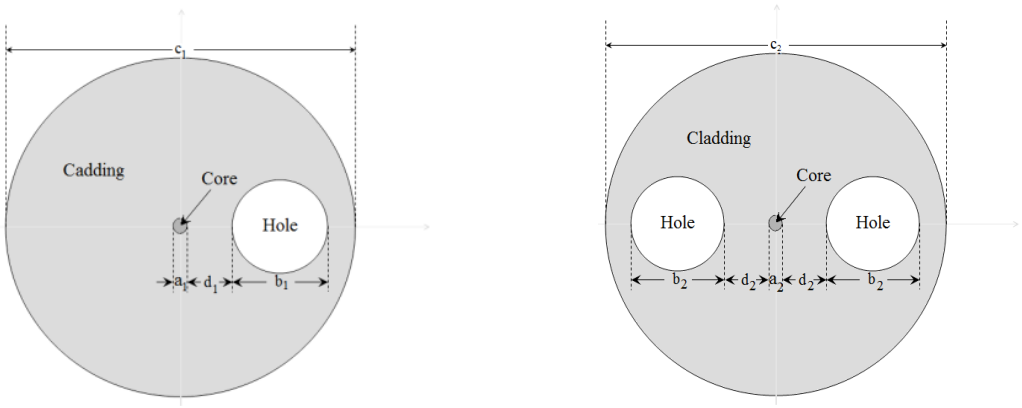

Figure 4.1 (a) One-hole high-birefringence fibre that has a hole diameter of 30 μm and the distance between the right edge of the core to the left edge of the hole d d_1 is 9 μm. (b) Two-hole high-birefringence fibre that has two holes with the same diameter of 27 μm and the distance between the right edge of the core to the left edge of the hole on the right d_2 is 14 μm.

These two specialist fibres have been designed, fabricated, and supplied by Acreo AB in Sweden. Both types of fibres have the cladding diameters of 125 μm (μm) and core diameters of 8.7 μm ($a_1 = a_2 = 8.7$ μm). The one-hole fibre as shown in Figure 4.1(a) has a hole diameter b_1 of 30 μm and the distance between the right edge of the core to the left edge of the hole d_1 is 9 μm. The two-hole fibre shown in Figure 4.1(b) has a hole diameter b_2 of 27 μm and the distance between the right edge of the core to the left edge of the hole on the right d_2 is 14 μm. Table 4.1 shows the summary of the fibres parameters.

Fibre type	One-Hole	Two-Hole
Supplier	Acreo AB, Sweden	
Image	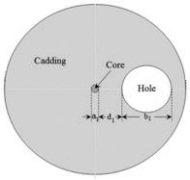	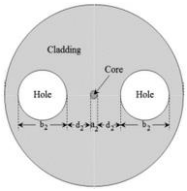
∅fibre [μm]	125	125
∅core [μm]	8.7	8.7
Hole diameter [μm]	30	27
Distance between the right edge of the core to the left edge of the hole	9	14
B (1550 nm)	8×10^{-5}	2.8×10^{-5}

Table 4.1 Summary of fibres parameters

As analyzed in detail in Chapter 3, the inclusion of holes in the fibre structures is able to change the stress distribution inside the fibres; therefore, these side-hole fibres are expected to exhibit high sensitivity to the external perturbation, which may arise from variations in temperature, twist, strain, stress, or pressure.

4.1.1 Sensor configuration

Figure 4.2 shows a schematic diagram of the experimental set-up used in this work for pressure measurement using a PM fibre. The light source used is a single mode laser with an output power of 10 mW at a wavelength of 1550 nm. The light is launched into a PM fibre after passing through a polarization controller (PC) and a polarizer, which are used to achieve azimuthally control of the polarization of the light before entering the PM fibre. The polarization state of the light entering the fibre was adjusted to give equal intensity of light in each eigenmode of the sensing fibre. An in-line polarizer fusion-spliced in front of a high birefringent sensing fibre can be used to replace the discrete component as shown in the diagram.

In order to apply pressure/force in different directions, two fibre rotators were used to allow a resolution of 5 degree in the change of rotation. As illustrated in Figure 4.2, a PM side-hole fibre was

sandwiched between two parallel plates with two additional 'dummy' fibres (physically the same size carrying an optical signal) used as well to allow the plates to remain parallel when the force is applied, preventing the sensor fibre from twisting and the top plate from rocking.

The sensing length *l* used was 45 mm and the PM fibre was loaded by applying a calibrated mass on the lever and measurements were undertaken, showing the intensity of the signal as a function of rotation angle of the fibre and the magnitude of the force applied.

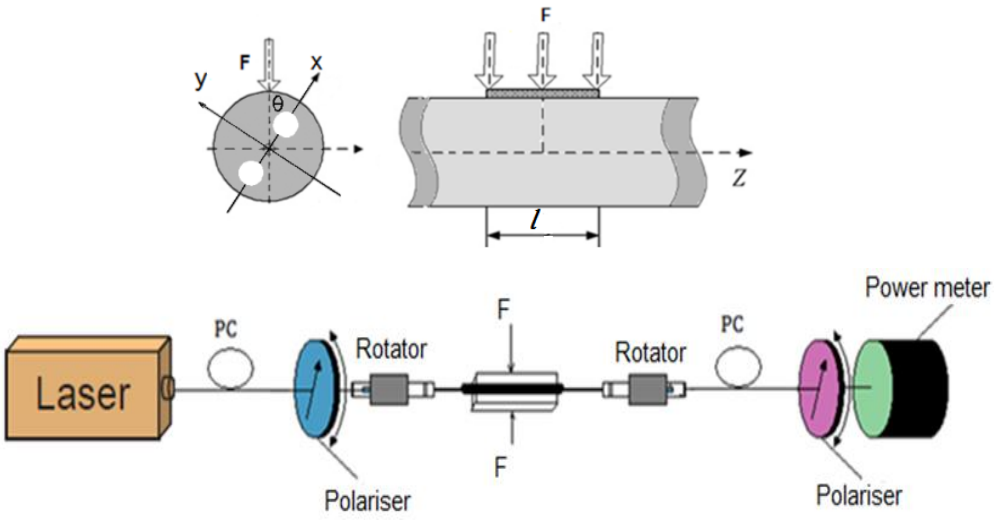

Figure 4.2 Schematic diagram of the experimental set-up of the PM fibre with force applied (θ) is the angle between the applied force and the slow axis x of the fibre)

The intensity of the light, after travelling through the birefringent section of the fibre and the polarizing analyser at the fibre output, is measured by a digital power meter.

The output intensity can be readily analysed using the Jones matrix algebra as follows. As we assumed that the input beam is linearly polarized and both orthogonal polarization modes of the high-birefringence fibre were equally excited.

In that case, using the Jones matrix notation, the electric field of the light E_{in} can be expressed as [233]

$$E_{in} = \frac{1}{\sqrt{2}}\begin{pmatrix}1\\1\end{pmatrix} E_0 \tag{4.1}$$

where E_0 is the magnitude of electrical field of input beam light and the matrix $\begin{pmatrix}1\\1\end{pmatrix}$ show the light polarization state direction at an angle of 45° with the axes of the fibre,

The electric field of the light after travelling through the birefringent section of fibre and the polarizing analyzer at the fibre output E_{out} can be calculated as

$$E_{out} = ATE_{in} \tag{4.2}$$

where A is the Jones matrices of the polarization analyzer and for the case of a polarization analyzer positioned with its axis at an angle of 45° with the axes of the fibre, A is given by [233]

$$\mathrm{A} = \frac{1}{2}\begin{pmatrix}1 & 1\\1 & 1\end{pmatrix} \tag{4.3}$$

and T is the transmission matrix (equation 3.96)

The intensity detected after the polarization analyzer will be

$$\mathrm{I} = \mathrm{E}^2 = \frac{\mathrm{I}_0}{2}[1 + \cos(\Delta\varphi)] \tag{4.4}$$

where I_0 is the total output power. Therefore, the change in polarization will be observed as a change of intensity after the analyzer, producing a sinusoidal signal.

In the other word applying a lateral pressure cause the phase difference between the two polarization modes HE_{11}^{x} and HE_{11}^{y} propagating in a birefringent fibre, as it can be seen in equation (3.111) $\Delta\beta$, is related to the applied pressure or transverse force through the change of differences between the propagation constants of polarization modes over a fibre length l, which can be expressed as follows.

$$\Delta\varphi = (\Delta\beta - \Delta\beta_0)\mathrm{l} \tag{4.5}$$

Where $\Delta\beta_0$ is the difference between the propagation constants of polarization modes when there is no force and $\Delta\beta$ represents the difference between the propagation constants of polarization modes when a force is applied on a fibre unit segment, and is given by equation (3.111)

When the PM fibre is used for pressure measurement, the sensitivity can thus be defined as the change of phase difference per unit applying force per unit length as shown in equation (4.6)

$$S = \frac{\Delta\varphi}{\Delta f} \tag{4.6}$$

Based on equations (4.5), (4.6) and (3.111), the pressure sensitivity of the PM fibre can thus be obtained when the force is applied in different directions, this forming the basis of the sensor.

The sensitivity of a PM pressure sensor is dependent on the degree of polarization rotation angle introduced by a particular measurand and it represents the minimum detectable pressure change as a function of rotation angle.

4.1.2 Evaluation of the side-hole fibre-based sensor performance

Figure 4.3 shows the phase differences obtained over a sensing length of the fibres and a cross comparison was made between the two sets of experimental data obtained and of the theoretical data obtained by using (4.5) and (3.111), when both types of side-hole fibres were subjected to different loads at different angles. The phase differences have shown to increase with the increase of applied load and when the angle of applied force in relation to the slow axis of the fibre increases, the change of the phase differences becomes more dramatic, indicating different sensitivities when the fibres are used for pressure measurements. For both types of fibres, a maximum sensitivity can be achieved when the force is applied at 0° and 90° in relation to the fibre slow axis. The experiments have also confirmed that the sensitivity of these specialized pressure sensors is independent of the fibre length and of the axial location of the force along the fibre length compared to the other sensors [236]. This makes the sensors more suitable for distributed force measurement.

Figure 4.3 (a) shows the results obtained from the one-hole fibre, when it was respectively subjected to different loads at various angles, of 0°, 30°, 60° and 90°. It can be seen that when the applied force is lower than 50N, there is a good agreement between the experimental and theoretical data for 30°, 60° and 90° but this is not seen for 0°. When the force applied is increased, there is an increasing discrepancy between the theoretical and experimental data. This disagreement arises from the assumption in theory that the hole(s) is/are not distorted under the pressure, which is true when the applied force is within a certain range. Therefore the theory should be valid before the shape of the hole(s) and the cladding starts to change.

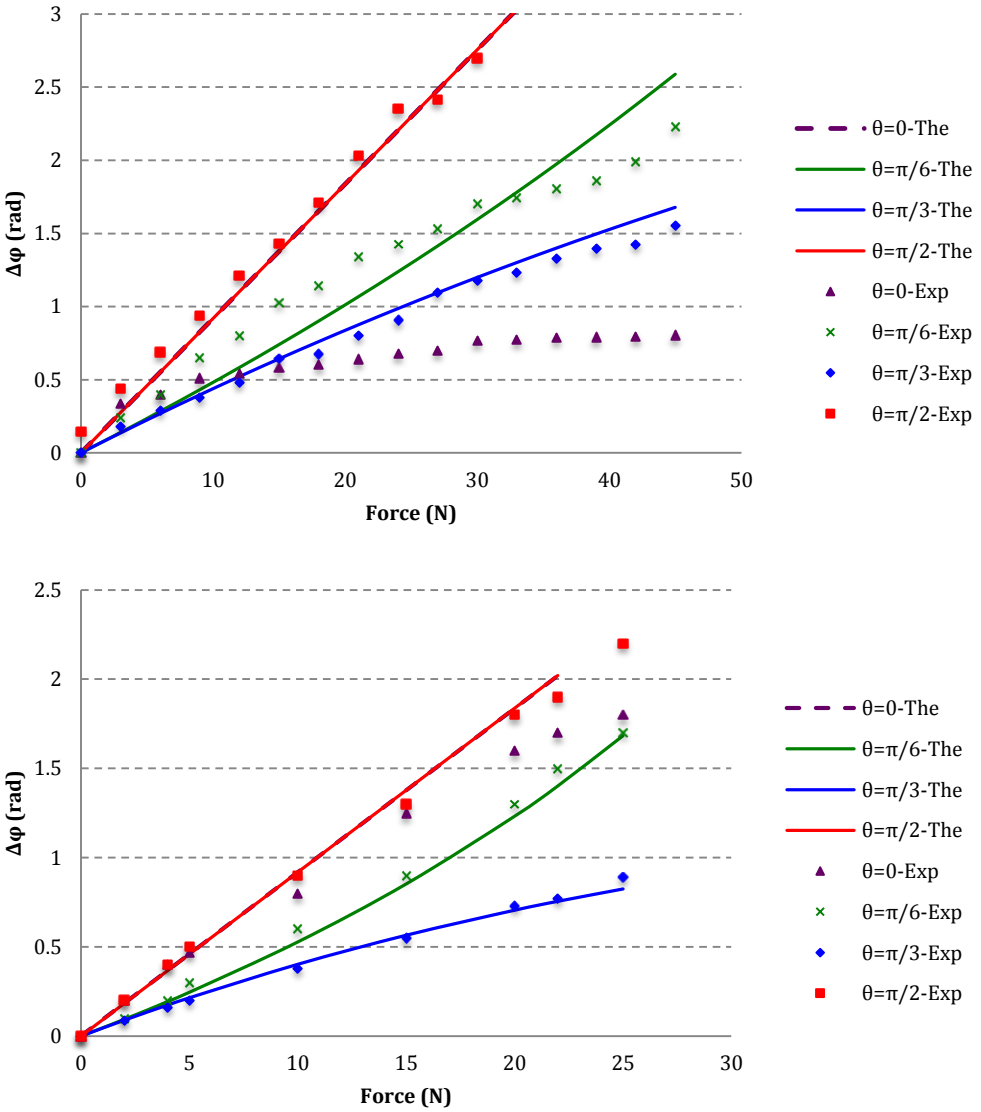

(b)

Figure 4.3 Comparison of experimental and theoretical phase differences of the PM fibres when force is applied at different angles in relation to the slow axis of the(a) one-hole fibre, (b) two-hole fibre

As a result, the assumption of the theory used in equations (4.5) and (3.111) is no longer completely valid. This phenomenon can also be seen for the situation when θ is zero, i.e. the direction of the applied force is along the fast axis. Even when a small force is applied, the assumption of a circular hole used for the theory does not hold and therefore the agreement between theory and

experimental data seen elsewhere is lost. Similar results have been observed for two-hole fibres in Figure 4.3 (b), when the force is applied at different angles and again within a limited range, there is agreement between theory and experimental data when the angels are 30°, 60° and 90°, but not at an angle of 0°. Also, for both fibres, the increase of rotation angle enables the sensing range to be shortened and compared to the situation for the two-hole fibre, revealing that the sensing range of one-hole fibre is much wider.

Figure 4.4 summarizes the sensitivity trend for one-hole and two-hole fibres respectively, when the angle of the applied force varies. The force applied was 2 N, over a distance of 45 mm. The blue cross symbols in Figure 4.4 show the sensitivities obtained from experimental data and the blue lines show the results obtained from theory. As explained above, when the force is applied along the fibre slow axis, there is a mismatch between the theory and experiments, due to the assumptions in the theory which then become invalid. However when the rotation angle is at either 30°, 60° or 90°, agreement is seen especially when the force applied is within a specific range and especially when the rotation angle approaches 90°.

In light of the above results obtained, it can be concluded that in the design of an optimized sensor device using such fibres, there is a compromise that can be struck between the sensitivity and the sensing range. Compared to the two-hole fibre, one-hole fibre has demonstrated wider sensing range, but smaller sensitivity when they are subjected to the same conditions. This will have implications for practical applications of the technique when these fibres are used for directional pressure measurements. Compared to the other phase-based techniques reported, these two sensors have demonstrated wider sensing ranges [234].

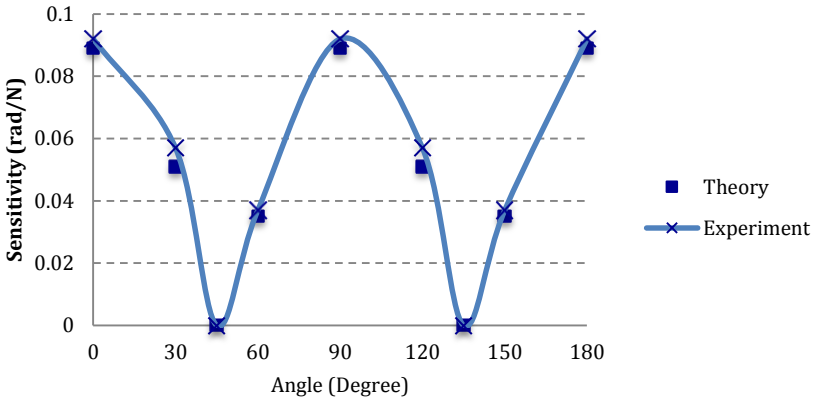

(a)

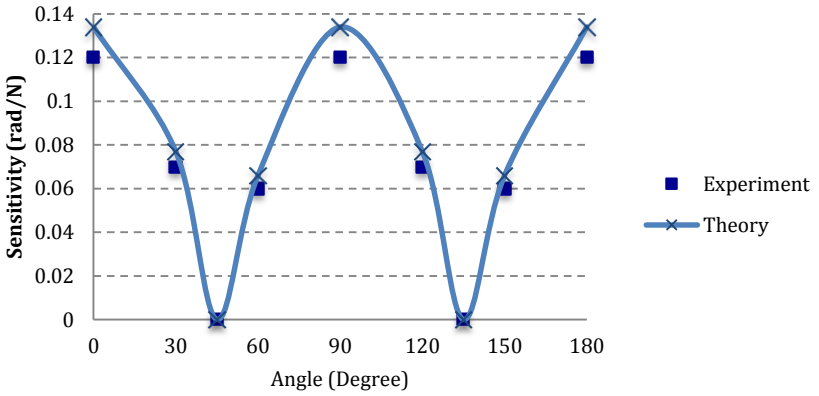

(b)

Figure 4.4: Sensitivity as a function of rotational angle for (a) one-hole and (b) two-hole fibres

4.2 Transverse force sensitivity of photonic crystal fibres

Photonic crystal fibres (PCFs) are a recent generation of fibres which are characterized by a periodic arrangement of air holes running along the entire length of the fibre, centred on a solid or hollow core. PCFs represent a diversity of interesting features as optical fibres, for example, achieved through the change or periodic modification of their geometric structures when composed of a single material, allowing access to the special properties of the fibres, which are of interest for a wide range

of different sensing applications, as shown.

Since Photonic Crystal Fibres (PCFs) were first introduced by Knight *et al.* in 1996 [66], there have been various reports which have explored the potential of using these micro-structured optical fibres as the basis of sensors for various industrial applications [67], such as strain and temperature sensors [68][69] and as hydrostatic pressure sensors [70][71].

Limited research has been undertaken on their potential as lateral force/pressure sensors using their birefringence characteristics. Zhang *et al.* [79] have investigated theoretically the birefringence properties of a Panda-type PCF and shown that there is a dependence on the direction of the force being applied.

Liu *et al.* [80] have reported a similar dependence on the direction of the applied force for a simulated 'grapefruit-structured' PCF. In order to improve the directional sensitivity of PCFs to a variation in lateral pressure, the use of several different schemes, such as employing fibre gratings [81] or an interferometric configuration [82][83] have been reported. The work published by Peng *et al.* [84] has shown that when a standard hexagonal (low birefringence) PCF was used as a transverse load sensor, an (unspecified) offset load was required to introduce the desired birefringence, which can then be measured and the highest sensitivity to a transverse load reported in literature using PCFs was approximately 0.5 nm/N mm [83][84].

Recently Yang *et al.* [238] have presented research on the development of an embedded transverse pressure sensor with negligible temperature sensitivity, which has shown transverse pressure sensitivity in different directions with respect to the birefringence axes of the PM- PCF.

The field is one where new applications of PCF in Sagnac interferometer (or termed Fibre Loop Mirror) configuration has also been reported recently. For example a fibre-optic curvature sensor based on hollow-core photonic crystal fibre (HC-PCF) Sagnac interferometer has been demonstrated by Gong *et al.* [239] in which the two ends of the 36 cm HC-PCF are spliced to the two arms of a 3 dB single-mode fibre coupler to form the Sagnac interferometer. The results obtained from an analysis of the output spectra confirmed a linear relationship between the wavelength shift and the curvature, showing a high curvature sensitivity but a low temperature sensitivity.

In addition, Cui *et al.* [240] reported the use of an optical fibre Sagnac interferometer to form a temperature sensor by using a selectively filled polarization-maintaining photonic crystal fibre (PM-PCF). Again the temperature-sensitive transmission spectrum of the interferometer was used, coupled

to an extremely low- cost process to realize the selective filling. Their results showed a high sensitivity with a 117 mm PM-PCF and an investigation of the sensitivity dependence on the infiltration length ratio was also undertaken.

Specifically the use of the FLM technique for the measurement of pressure and force has been reported previously in several published papers: however most of this reported work has been focused on the measurement of hydrostatic pressure [241], while only a few papers discussing lateral pressure sensor designs [242], for example from Gan *et al.* [243], who have reported a pressure sensor design which is orientation-free, by using a π-shifted all-single-mode-fibre (SMF) Sagnac interferometer. In addition, Kim *et al.* [244] have demonstrated a transverse load sensor designed to employ a section of highly birefringent PCF with a modified air hole distribution and thus achieved a sensitivity of 2.17 nm/N cm. Yong *et al.* [245] have demonstrated a technique which is able to convert the wavelength shift into a signal intensity variation to allow a simpler, and thus cheaper detection system to be used.

All the above work shows the 'state-of-the-art': emphasizing the importance of the field and the research in this section builds on what has been reported in the literature and describes an investigation into a lateral force measurement system, looking in detail at the performance of different types of PCF in a Sagnac interferometer configuration.

Previous experiments undertaken have been focused on the directional transverse force measurement using different side-hole fibres and this section is focussed on the experimental evaluation of photonic crystal fibres to study their respective sensitivities both to the magnitude and to the direction of an applied lateral force.

4.2.1 Sensor fabrication

Herein four different types of PCFs have been investigated to study their respective sensitivities both to the magnitude and to the direction of an applied lateral force. In addition, the birefringence characteristics of a pair of joined PCFs were investigated, using PCFs designed, fabricated and supplied by IPHT, Jena, in Germany and UMCS, Lublin, in Poland.

Table 4.2 shows the details of the four PCFs evaluated in this work, which includes two standard hexagonal PCFs (Types 391b3 and 090329P), a Hi-Bi PCF (Type 070107P2), a six-hole PCF (Type 478b2) and also a Panda (PM1550-HP) fibre for cross-comparison.

Fibre type	PCF 478b2	PCF 391b3	PCF 070107P2	PCF 090329P	Panda PM1550-HP
Supplier	IPHT, Jena, Germany		UMCS, Lublin, Poland		Thorlabs
Image		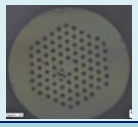	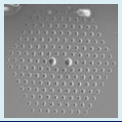	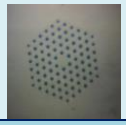	
Cladding [μm]	125.1	125.3	96	119	125
MFD [μm]	11.6	14-2	-	-	10.5 ± 0.8
d [μm]	13.8	3.3	1.4	2.5	-
Λ [μm]	15.0	8.4	3.1	5.6	-
D [μm]	-	-	2.7	-	-
Length [m]	9	9	0.4 (0.7)	9	0.4 (0.7)
B(1550)	1.815e-5	4-02e-6	1.446e-3	4-1e-6	3.8e-4

Table 4.2 Parameters of the photonic crystal fibres used in these experiments. In the table, MFD is the Mode Field Diameter, d the small hole diameter, D the large hole diameter in the case of the Hi-Bi fibre, Λ the distance between adjacent holes, B(1550) the birefringence at 1550 nm, and S the sensitivity around 1550 nm at the most-sensitive direction.

The sensitivity of the polarization maintaining fibres to a known force, for different lengths and birefringence values of the fibres (under a fixed applied force) has been investigated, theoretically in Chapter 3. The theoretical analysis shows that the pressure/force sensitivity is not a linear function of the fibre length and birefringence value of the fibre. It also indicates that using a shorter fibre length can increase the fibre pressure/force sensitivity.

4.2.2 Sensor configuration

In order to investigate the effect of the birefringence variation of the PCFs selected, as a

function of applied force, a similar fibre loop mirror (FLM) was configured as shown in Fig. 4.5. The setup consists of a superluminescent light emitting diode (SLED) with its emitting wavelength being centred at 1550 nm and a 3 dB coupler which splits the input signal into two waves that counter-propagate along completely identical paths and thus experience the same loss. Hence, the condition for achieving optical interference in the fibre is satisfied. In addition, the FLM configuration has shown a low insertion loss, polarization independence to the input light, a broad spectral bandwidth and a high resistance to environmental changes as the two waves propagate through identical paths. The extinction ratio of the system can be maximized using a polarization controller (PC) within the loop (Fig. 4.5) where the interference patterns were monitored using an Optical Spectrum Analyser (OSA).

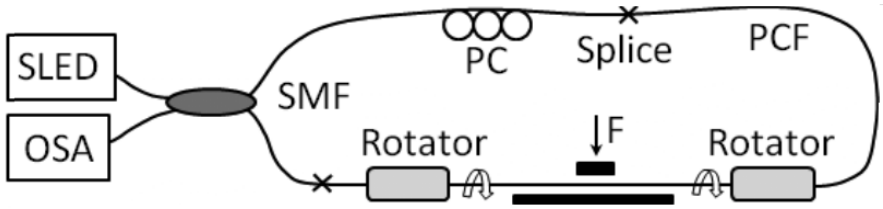

Figure 4.5. Schematic of the experimental setup used in this investigation. PCF is the photonic crystal fibre used and PC is the polarization controller. SLED is the superluminescent LED source and OSA is the Optical Spectrum Analyzer used. The force, F, is applied as shown.

The PCFs used were fusion-spliced to standard single-mode fibres at both ends for ease of setting up the FLM used for the evaluation planned and the losses arising were observed to be approximately 10 dB and 4.0/8.7 for two hexagonal PCFs (Types 391b3a and 090329Pb), 15 dB for the Hi-Bi PCF (Type 070107P2) and 3.0 dB for the six-hole PCF (Type 478b2).

A lower insertion loss can be achieved by including an intermediate fibre or by optimizing the parameters for fusion splicing. However, the sensing accuracy and reproducibility of the sensors created on the PCFs should not be affected by the relatively high splicing loss.

Table 4.3 shows the photos of splices and also summarizes the information in relation to the fusion-splices between various types of PCFs and single mode fibres, where d λ/dT represents the wavelength shift dependence on temperature variation.

	Image	Fibre	Splice image	Length (m)	Loss (dB)	Birefringence ($\times 10^{-4}$)	d λ/dT (nm/K)
Thorlabs		PM1550-HP	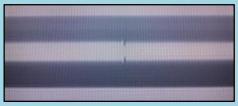	0.4, 0.7	2.0 / 2.7	0.8	-1.7
UMCS	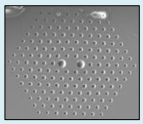	070107P2		0.4, 0.7	12.5 / 17.8	14-5	-0.05
		090329P		9	4-0 / 8.7	0.04	--
IPHT		478b2		9	2.8 / 3.0	0.18	--
	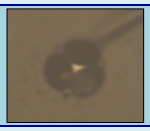	441b2	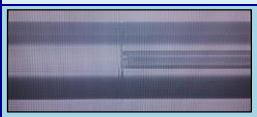	9	27.5 / 27.7		--
		391b3		9	10.0 / 10.1	0.04	-

Table 4.3 shows the pictures of fusion splices of various types of PCFs to single mode fibres

4.2.3 Evaluation of the PCF-based sensor performance

Figure 4.6 shows a photo of an experimental set-up. The length of the Hi-Bi PCF was chosen to be approximately 0.4 and 0.7 m while the low birefringent fibres were required to be much longer (9 m) in order to ensure the spacing between interference fringes is observable within an OSA. In order to apply stress/force from different directions, two fibre rotators were used (Figure 4.6) and the PCFs were sandwiched between two parallel plates of 45 mm in length. The applied force was increased in steps of 2 N, over the range from 0 to 10 N.

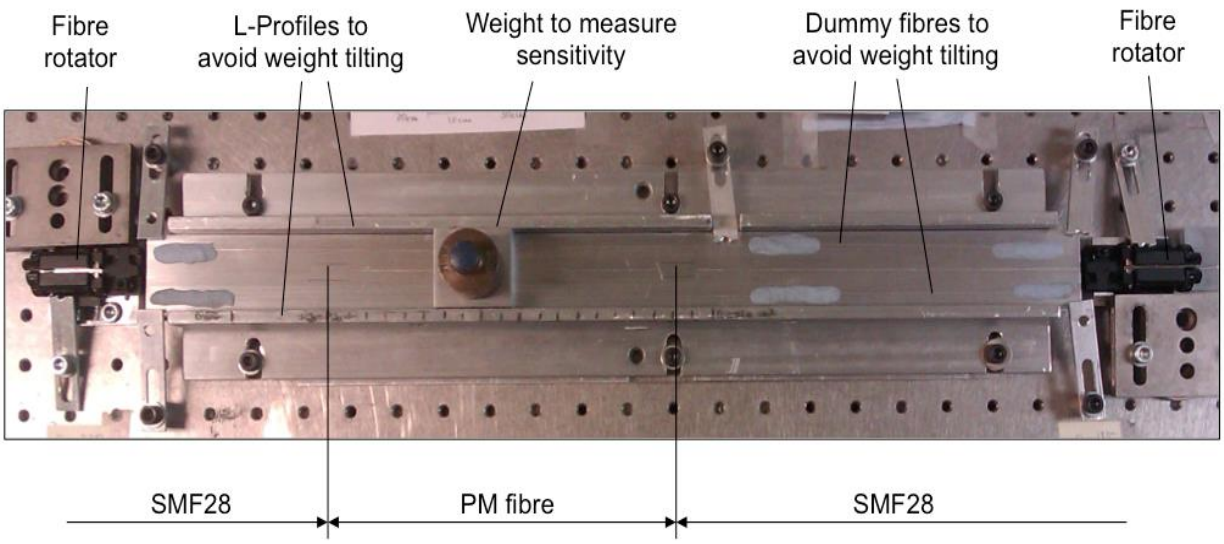

Figure 4.6 Experimental set-up for the evaluation of PCF-based pressure/force sensors

As shown in equation 3.130, the lateral pressure sensitivity of PM fibres using FLM is dependent on the fibre length and the initial birefringence of the Hi-Bi fibres.

Figure 4.7 shows the wavelength shift as a function of the force applied to two different lengths (the length of second part, length L_2 in equation (3.130)) of the Panda and the Hi-Bi PCF, of lengths 0.40 m and 0.70 m respectively. The applied force was increased in steps of 2 N, over the range from 0 to 10 N.

A cross-comparison was made between the experimental data obtained (Exp) and the results of the theoretical analysis using equation (3.128), when both types of fibres were subjected to the same loading. As can be seen from figure 4.7, the wavelength shift shows a linear relationship with the transverse pressure. Good agreement is seen between the theoretical and experimental results, this being less evident in the case of Panda fibre of length 0.40 m where the theoretical prediction is a little higher than the experimental results obtained. This discrepancy is likely due to the assumption made in the theoretical analysis that there is a minimum contact surface area of fibre with the applied force, which is difficult to realize in practice.

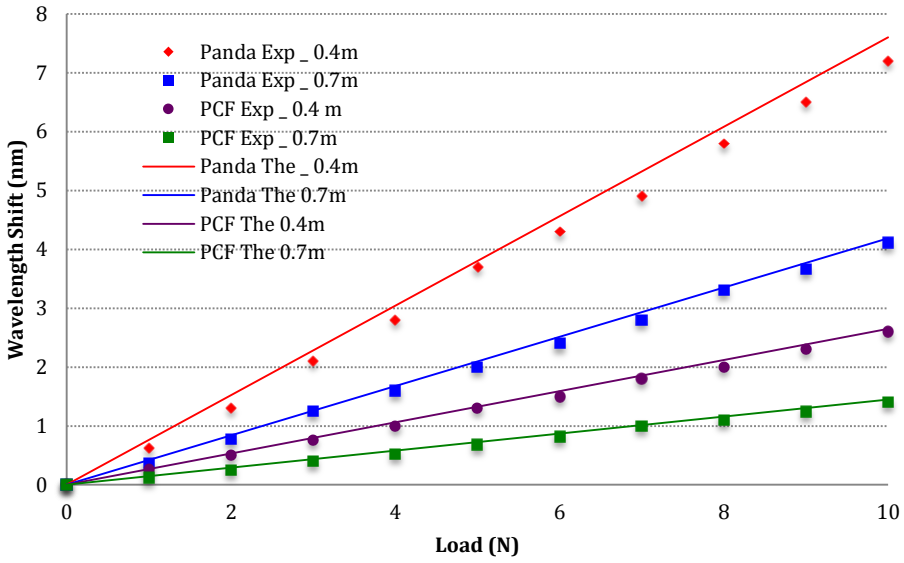

Figure 4.7: Wavelength shift versus external load for force up to 10N, in steps of 2N. Points represent the experimental results (Exp) and the solid lines the results of the theoretical analysis (The)

The results obtained show that the fibres with the same birefringence but with different lengths have demonstrated different sensitivities to force. For example, for the Panda fibre, the sensitivity observed is 0.72 nm/N mm and 0.41 nm/N.mm respectively for 0.40 and 0.70 m: here the fibre with the shorter length demonstrates a higher sensitivity to the applied lateral force. A similar conclusion is made for Hi-Bi PCF with the pressure sensitivity of being 0.26 nm/N.mm and 0.14 nm/N.mm respectively for the 0.40 m and 0.70 m lengths of fibres respectively.

Fibre type	Fibre length (m)	Experimentally measured sensitivity (nm/N.mm)	Theoretically predicted sensitivity (nm/N.mm)
HiBi PCF	0.40	0.26	0.27
HiBi PCF	0.70	0.14	0.15
Panda	0.40	0.72	0.76
Panda	0.70	0.41	0.42

Table 4.4 Experimental data showing the sensitivity dependence of PM fibres on the fibre length, with reference to the theoretical prediction

The experimental results obtained also confirm that the pressure sensitivity of the fibre is dependent on the birefringence as well as the length and these results obtained are summarized in Table 4.4. This shows that the higher birefringence is associated with a higher pressure sensitivity.

Figure 4.8 summarises the spectral wavelength shifts (at around 1550 nm) when a constant load is applied to the two types of fibres used, Panda and Hi-Bi PCF, along different directions over the range from $\theta = 0^{\circ}$ to 180°, where θ is the angle between the applied force and the slow axis of the fibre. In this experiment, the applied force used was 2 N applied over a distance of 45 mm.

Figure 4.8 confirms that at θ=90º, the wavelength shift reaches the peak expected from the theoretical prediction. This shift is predicted to be 1.54 nm and 0.53 nm respectively for the Panda and the Hi-Bi PCF fibres: experimentally these wavelength shifts were measured to be 1.28 nm and 0.40 nm respectively, also demonstrating a smaller wavelength shift for both fibres. At θ=0º and θ=180º, wavelength shifts were observed and predicted by the theoretical analysis to be -1.54 nm and -0.53 nm for the Panda and Hi-Bi PCF respectively, where the experimental data confirm again smaller wavelength shifts: there being -1.12 nm and -0.40 nm respectively. The results are tabulated in Table 4.5. The discrepancy between the theoretical and experimental data observed in Figure 4.8 again is expected to result from the assumption made in the theoretical analysis that there is a minimum contact surface area with the applied force and this is difficult to realize in practice.

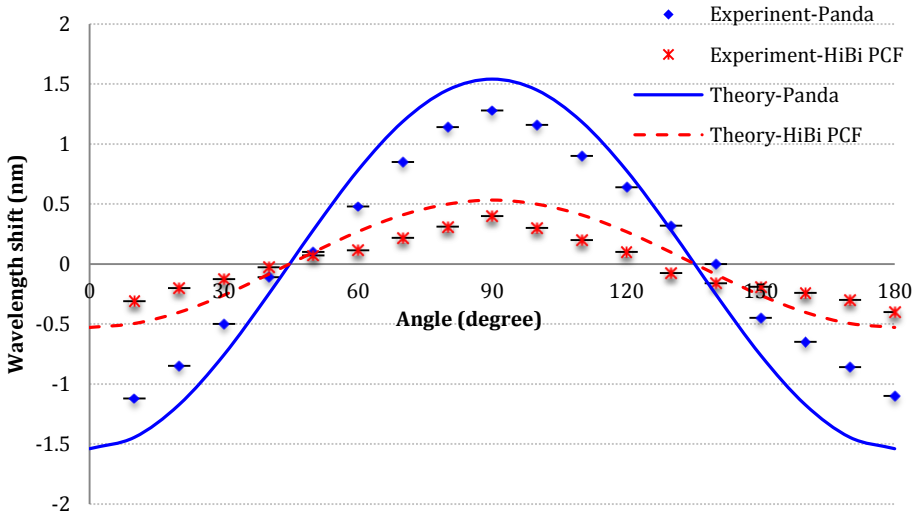

Figure 4.8 Wavelength shift versus fibre orientation (force direction) for angles from 0° to 180°. Points are obtained from the experimental work and the solid line results from the theoretical analysis

Fibre type	Fibre orientation, θ (Degrees)	Experimentally measured wavelength shift (nm)	Theoretically predicted wavelength shift (nm)
HiBi PCF	90	0.40	0.53
HiBi PCF	0 or 180	-0.40	-0.53
Panda	90	1.28	1.54
Panda	0 or 180	-1.12	-1.54

Table 4.5 Experimental data showing the sensitivity dependence of PM fibres on the fibre orientation, with reference to the theoretical prediction

Figure 4.9 summarizes the normalized spectral wavelength shifts seen at wavelengths of around 1550nm when a constant load is applied to the four types of PCFs, i.e. 9 m lengths for Types 391b3a, 090329Pb and 478b2a and 0.7 m for Type 070107P2b, with different orientations from 0 to 180 deg. The force applied was 2 N, over a distance of 45 mm and the results were normalized to the maximum value for each fibre.

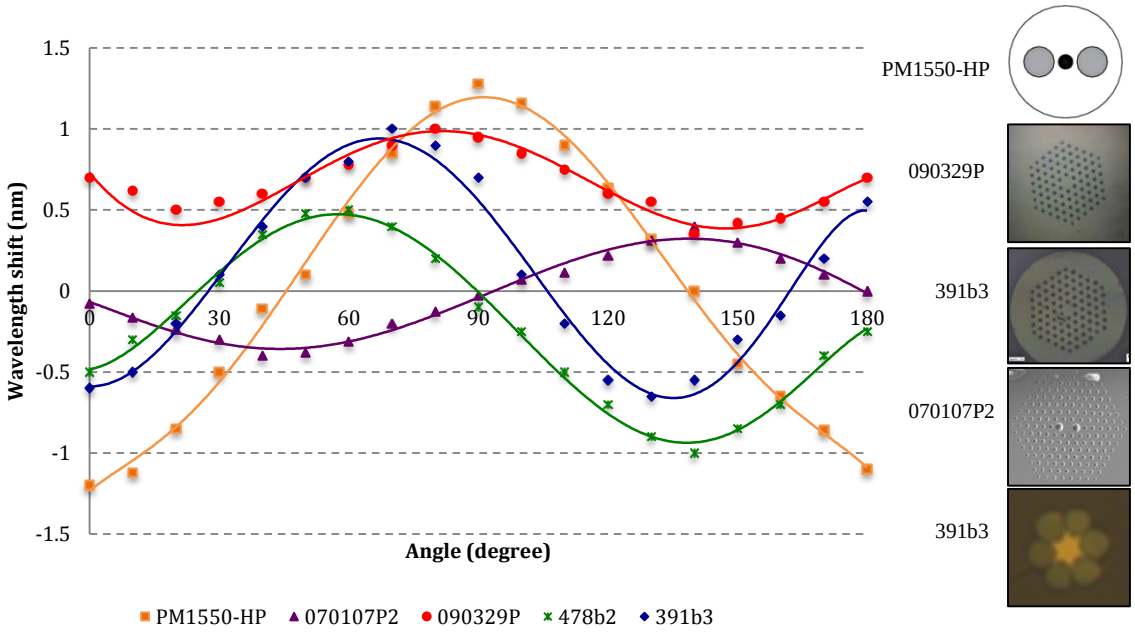

Figure 4.9. Wavelength shift versus fibre orientation (force direction) for angles from 0 to 180 deg for the four fibre types considered.

It is clear from Figure 4.9 that the force sensitivity of all the PCFs tested is dependent on both the direction of the applied force and on the geometrical structures of the fibres themselves. For example, for hexagonal PCFs (Types 391b3a and 090329Pb), a period of 120 deg. is observed and for the higher birefringent structures (Types 070107P2b and 478b2a), a period of 180 deg. is observed. As a result, in the following applied force measurements considered, the orientation of each PCF was specifically chosen according to the highest sensitivity actually achieved.

Figure 4.10 shows the wavelength shift as a function of the applied force for each of the PCFs evaluated, changing the load in steps of 1 N, for forces applied of up to 10 N. The results obtained show that the PCFs with lower birefringence demonstrate a higher sensitivity to the applied lateral force. Thus the sensitivities obtained for the Hi-Bi PCF (Type 070107P2), six-hole fibre (Type 478b2) and two Low-Bi PCFs (Types 391b3 and 090329P), over an interaction length of 45 mm, are 0.298, 0.837, 3.580 and 4.07 nm/N. However, it is more convenient to express the sensitivity per unit length. Thus to represent these measurements in that way, the data given are divided by the length of fibre used and which is under stress (but also divided by a multiple by two as any direct force will be experienced twice because of the reflection of the light along the fibre). Thus the normalized sensitivity of these fibres can be reported as 0.014, 0.038, 0.162 and 0.185, nm/N mm respectively.

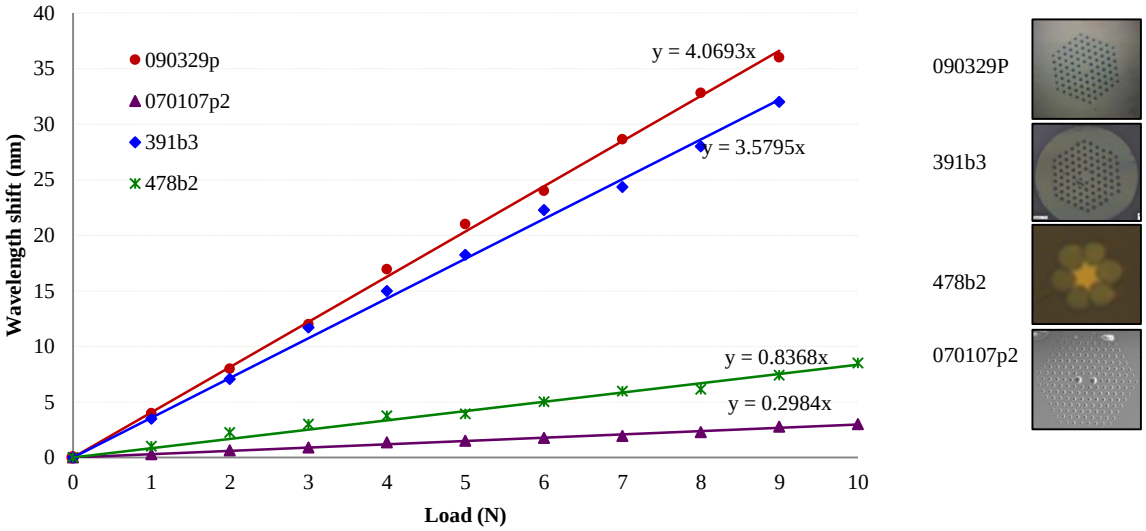

Figure 4.10. Wavelength shift versus external load for applied forces of up to 10 N, in steps of 1N for four different fibres (Type numbers shown and described in detail in the text)

These results obtained are summarized in Table 4.6. This shows that the lower birefringence is associated with a higher pressure sensitivity.

	Image	Fibre	Length (m)	Birefringence ($\times 10^{-4}$)	$d\lambda/df$ (nm/N mm)
UMCS	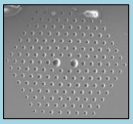	070107P2	0.4	14-5	0.015
		090329P	9	0.04	0.194
IPHT		478b2	9	0.18	0.036
	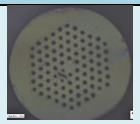	391b3	9	0.04	0.186

Table 4.6 Experimental data showing the sensitivity dependence of PM fibres on the birefringence of the fibres, with reference to the theoretical prediction

As can be seen from Figure 4.10, low birefringence PCFs demonstrates a higher sensitivity to the applied lateral force, but such fibres require a longer sensing length, typically 9m for a PCF with $B = 4.1 \times 10^{-6}$, compared to the 0.7m length required for a high birefringence PCF, as illustrated in Fig. 4.10, to ensure that the interference peak shift is sufficiently well identified using an interrogator. One possible solution to address the issue of adequate sensitivity over a reasonable length coupled to the higher sensitivity demonstrated by a low birefringence PCF is to consider the effect of joint PCFs and their potential for sensor applications.

4.3 Transverse force sensitivity of Joint PCFs

The experimental configuration discussed extensively in previous sections is suitable for force measurement using a short length Hi-Bi fibre but might not for the Low-Bi fibres. This is due to the fact that the birefringence and fibre lengths are inversely proportional, as described in equation (4.7), where the wavelength separation, $\Delta\lambda_{p2p}$ between the two output transmission peaks using FLM [162], is given by:

$$\Delta\lambda_{p2p} = \frac{\lambda^2}{LB} \tag{4.7}$$

when a polarization maintaining fibre experiences a lateral pressure/force, the visibility of at least one peak or dip is required, allowing for the tracking of the wavelength shift. Therefore the length of the Low-Bi PCF fibres must be long enough to allow the peak or dip to be 'visible' within the detection range of an Optical Spectrum Analyser (OSA) or a Micron Optics tracking system (e.g. Type sm130).

In this work, the length of the Hi-Bi PCF was chosen to be approximately 0.7m, while the length of the low birefringent fibres is required to be longer, e.g. 9 m in this work, in order to ensure the spacing between interference fringes is observable using the OSA or Micron Optics system.

Figure 4.11 shows the interference pattern obtained using an OSA showing the effects observed from the Low birefringence PCF (Type 090329Pb) and the High Birefringence PCF (Type 070107P20), illustrating the comparative wavelength spacing between the peaks.

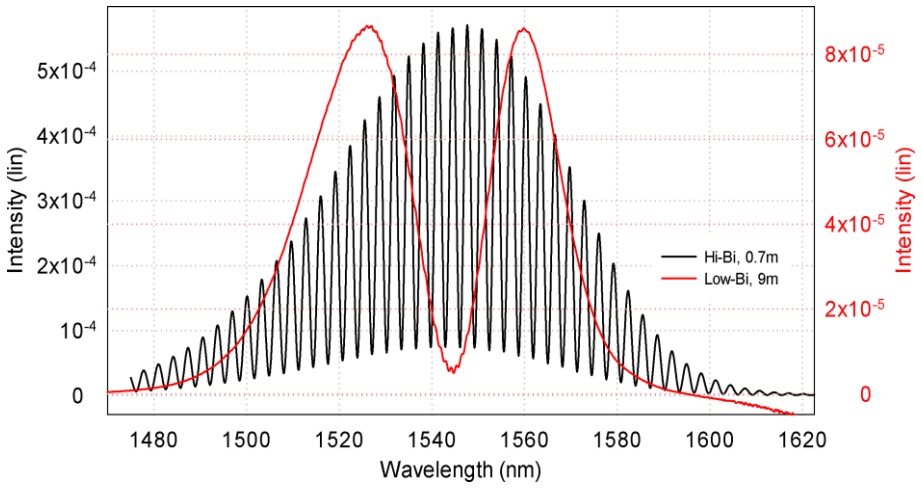

Figure. 4.11. Interference pattern obtained using the OSA showing the effects seen from the Low birefringence PCF (Type 090329Pb) and the High Birefringence PCF (Type 070107P20), illustrating the comparative wavelength spacing between the peaks. (In each case the vertical axis is an arbitrary intensity and the horizontal axis shows the wavelength range from 1450 to 1650 nm)

The use of a long length of a fibre is not only costly but also problematic in practical applications. On one hand, using a shorter fibre length is more economic, but the sensitivity depends strongly on the direction of the applied force direction. On the other hand the lower birefringence fibre has a higher sensitivity to the applied force but a greater length is needed to show a significant effect.

Figure 4.12 shows the snapshots of Interference patterns of Low and high Birefringence PCFs.

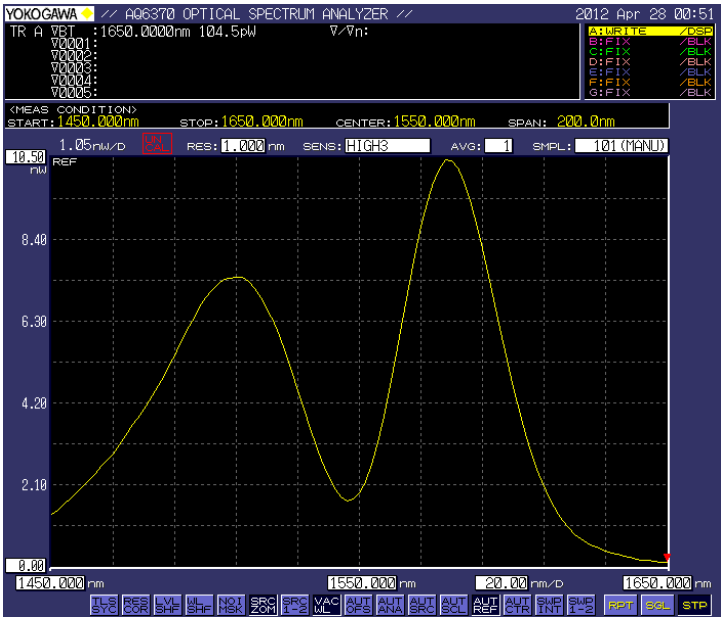

(a)

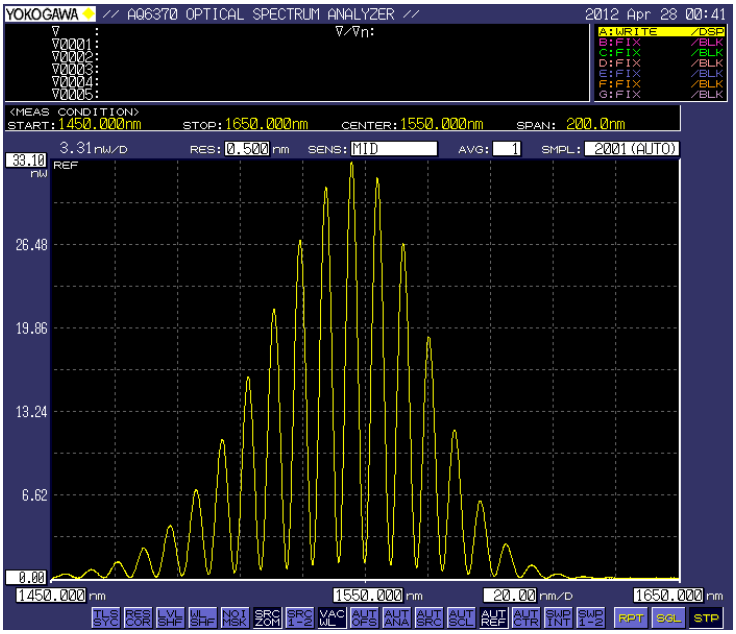

(b)

Figure 4.12: Interference pattern snapshots of (a) Low birefringence and (b) High Birefringence PCFs

4.3.1 Sensor configuration

A modified configuration system of the FLM allows the use of a short fibre length, emphasizing the advantages of Hi-Bi PCFs and low directional sensitivity of Low-Bi PCFs. To achieve this modified FLM, a configuration in which two different types of PCFs were used is shown in figure 4.13.

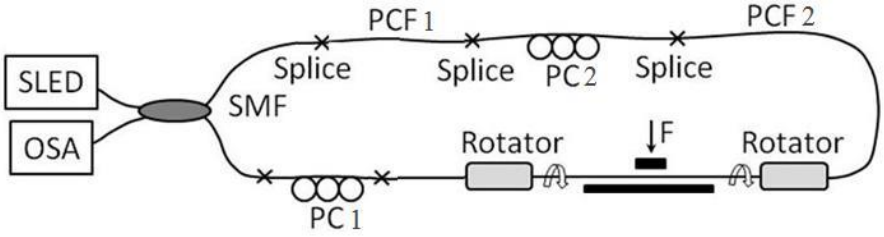

Figure 4.13. Schematic of the experimental setup used in this investigation. PCF1 and PCF2 are photonic crystal fibres and PC1 and PC2 are polarization controllers. SLED is the superluminescent LED source and OSA is the Optical Spectrum Analyzer used. The force, F, is applied as shown.

Figure 4.13 thus shows a modified setup for the configuration in which a joined piece of fibre is used. As can be seen (by comparison to figure 4.5), a second piece of fibre (PCF2) as well as a second polarization controller have been added to the setup and in this modified setup the extinction ratio of the system can be maximized using a polarization controller (PC1) within the loop (as shown in figure 4.5). The PCFs used were fusion-spliced to single-mode fibres at both ends and then connected together via a polarization controller (PC2).

When two different types of polarization maintaining fibres are connected together using a single mode fibre, their fast/slow axes will not necessarily match, and thus the excitation ratio will decrease. Therefore in this configuration PC2 is used to control and align the polarization-state between the fast/slow axes of the two PCFs, when the output light from PCF1 enters PCF2 after passing though the single mode fibre (SMF), and the interference patterns obtained were monitored using an Optical Spectrum Analyser (OSA). The PCF and the SMF were fusion-spliced using an arc fusion splicer and due to the structural and mode-field mismatch between the PCFs and SMFs, the splicing loss is relatively high, at 10.0 dB and 4.0/8.7 dB for two standard hexagonal PCFs (Types 391b3a and

090329Pb) joined to the SMFs. For Hi-Bi PCF Type 070107P2b and six-hole PCF Type 478b2a, the splicing losses were measured to be 12.5/17.8dB and 2.8/3.0dB respectively. A lower insertion loss can be achieved by applying an intermediate fibre or by optimizing the parameters for fusion splicing. However, the performance and reproducibility of the sensors thus created with the spliced PCFs should not be affected by the relatively high splicing loss.

In order to apply the force in different yet known directions, two mechanical fibre rotators were used to allow a resolution of 5° in the change of rotation when the sensing PCF fibre is sandwiched between the two parallel plates used. The sensing length of the PCF used was 45mm and the fibre was loaded by applying standard, known weights.

The transmission spectrum, *T*, of an optical FLM is described by [237]

$$T = [sin\ (\varphi/2)\ sin\ (\theta_1 + \theta_2)]^{\,2} \tag{4.8}$$

where θ_1 and θ_2 denote the angles of rotation of polarization state when propagating light enters the PM fibre and $\varphi = 2\pi LB/\lambda$ is the phase difference. λ is the guided wavelength, L the sensor fibre length, $B = n_x(\lambda) - n_y(\lambda)$ the birefringence, and $n_x(\lambda)$ and $n_y(\lambda)$ are the effective refractive indices of the fast and slow fibre axis, respectively.

The phase difference φ in equation (4.8) changes in response to the change in the fibre length and the birefringence, both of which are affected by mechanical load variation and the temperature. Therefore, the wavelength shift, $\Delta\lambda$, in the transmission spectrum due to the temperature and the transverse mechanical load variations can be written as

$$\Delta\lambda \approx \left(L\frac{\partial B}{\partial T} + B\frac{\partial L}{\partial T}\right)\Delta T + (L\frac{\partial B}{\partial F} + B\frac{\partial L}{\partial F})\Delta \mathrm{F} \tag{4.9}$$

where ΔT is the temperature variation and ΔF is the variation of the mechanical load. $\partial L/\partial T$ and $\partial L/\partial F$ describe the elongations of the fibre due to the temperature and mechanical load variation, respectively. These parameters are, however, negligible [162] compared to the birefringence change under the force. As the PCFs are insensitive to any temperature variation, equation (4.9) can thus be re-written as

$$\Delta\lambda \approx L_{\mathrm{f}}\frac{\partial B_{\mathrm{f}}}{\partial F}\Delta F \tag{4.10}$$

where $\partial B_F/\partial F$ is the birefringence variation coefficient introduced by the measured lateral

mechanical load. This parameter is a constant depending on the material properties, including the photoelastic coefficients, Young's modulus and Poisson's coefficient. It is clear from equation (4.10) that the wavelength shift is directly proportional to the transverse mechanical load.

4.3.2 Evaluation of the joint PCF-based sensor performance

Figure 4.14 shows the wavelength shift, as a function of force, applied in steps of 1N up to 10 N, for a series of joined PCFs tested (where the second code represents the sensing PCF). The length of the PCFs was chosen to be approximately 0.7 m for consistency.

The results obtained show that the combination of PCFs with the lowest (Type 090329p) and the medium level of (Type 478b2) birefringence demonstrates a higher sensitivity to the applied lateral force, with a sensitivity of 0.021(nm/N.mm) when the lower birefringence fibre was used as the sensor. By varying the sensing PCF fibres used, the lowest sensitivity that has been achieved was 0.002 (nm/N.mm). The sensitivities obtained for the other fibre combinations were found to lie between these two values.

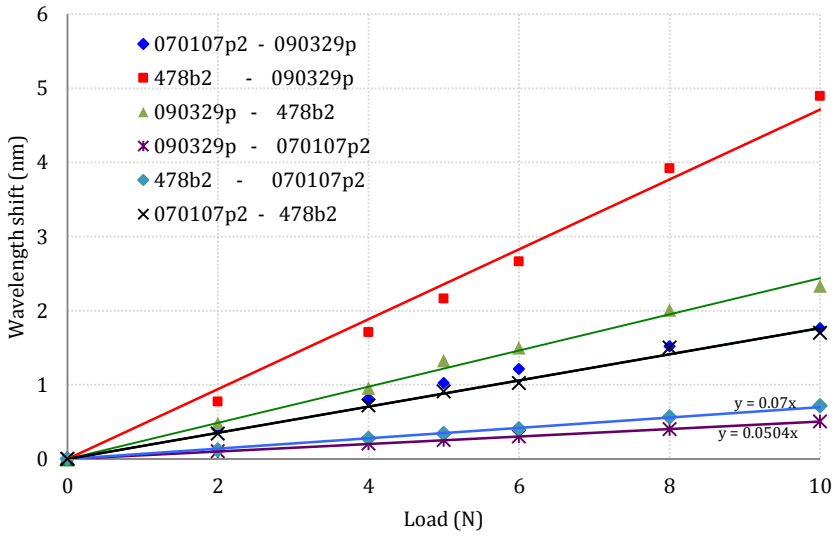

Figure 4.14. Wavelength shift versus external load for different combinations of PCFs for forces (loads) up to 10 N. The direction of the load applied to each PCF fibre combination used corresponds to the maximum sensitivity, as shown in Fig. 2. (Fibre types making up the combinations are shown in the inset.)

Fig. 4.15 summarizes the measured wavelength shifts as a function of the applied force for

different PCFs, both individually and in fusion spliced combination and the results show that the sensitivity to force of the joint PCFs evaluated, a combination of PCFs with a medium and a low birefringence, is 0.044 (nm/N.mm). The total length of the combination was chosen to be approximately 9 m. This sensitivity is lower than that of the low and medium birefringence PCFs alone (being 0.185 and 0.162 nm/N.mm respectively) but more sensitive than that of high birefringence PCF (with a sensitivity of 0.014 (nm/N.mm)).

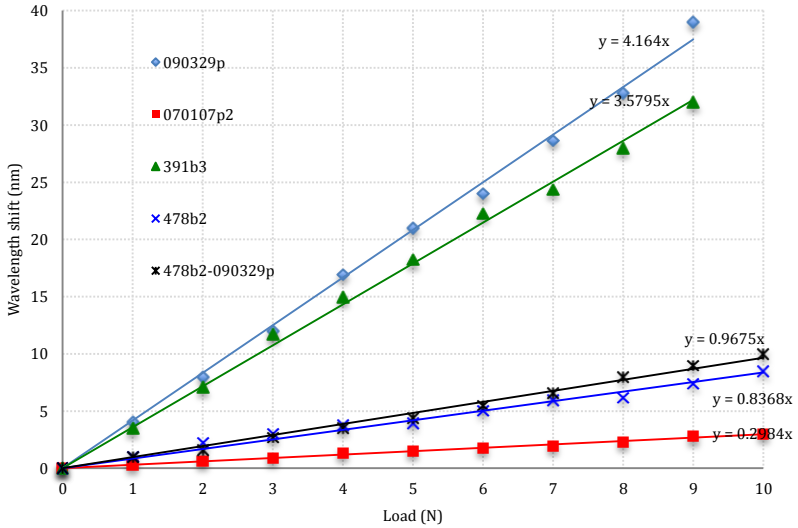

Figure 4.15. Wavelength shift versus external load for different individual fibres shown: types 090329p, 070107p2, 391b3, 478b2 and the combination 478b2 and 090329p, for applied forces (loads) of up to 10N. The direction the load was applied on each PCF corresponds to the maximum sensitivity illustrated in Figure 4.13.

The investigation confirms that when the length of the sensing fibre available is limited (for example in the case where the lateral force extends over a limited area of length of fibre), the use of a spliced PCF combination gives the best sensitivity for good lateral force or pressure measurement, over the use of either PCF alone.

Table 4.14 summarizes the sensitivity of the fibres when they are joint together

Fibre	Sensitivity (Individual)	Sensitivity (Joint)
070107P2	0.15	0.07
090329P	0.194	
478b2	0.036	0.47
090329P	0.194	
090329P	0.194	0.244
478b2	0.036	
090329P	0.194	0.05
070107P2	0.15	
478b2	0.036	0.176
070107P2	0.15	
070107P2	0.15	0.176
478b2	0.036	

Table 4.7summarizes the sensitivity of the fibres when they are joint together

4.4 Summary

In this chapter a series of experimental tests has been undertaken to evaluate the performance of two types of side-hole fibres when they are subjected to various loads at different orientations with a view to designing an optimized sensor system. The detailed theoretical analysis, which has been carried out in chapter three, supports this. As a result it has been shown that the lateral pressure sensitivity of both one and two-hole fibres has been successfully obtained and cross-compared with the results from the theory, from which it was confirmed that to optimize the design of a device based on this effect in these fibres, a 'trade-off' between the sensing range and sensitivity is observed. Thus different designs can be proposed for different situations. The results further have shown that there is good agreement between the experimental data and the theoretical analysis when the applied force lies within a certain

specific range and when the direction of applied force is further away from the slow axis. This is due to the fact that in the theory an assumption has been made that the holes in the fibres remain fully circular, even when the force is applied to the fibres, and experimentally it is known that this does not hold. An important conclusion is that these theoretical and experimental results obtained can form an effective foundation for employing these side-hole fibres as optical fibre sensors for real-time pressure measurements.

Following the design evaluation of a high birefringence single mode optical fibre-based sensor for pressure monitoring applications in chapter three, a series of experiments has been implemented on two different Hi-Bi fibres (Hi-Bi fibres Panda and PCF) to measure the fibres sensitivity to transverse pressure and angle dependency using a fibre loop mirror (FLM) configuration. The experiment results have shown that using a shorter fibre length can increase the fibre sensitivity and that fibres with higher birefringence have lower sensitivity as they were expected from theory. Also the experiment results have been revealed that sensitivity of Hi-Bi fibres are strongly dependent on the applied pressure angle. An experimental trial of a sensor system was also undertaken based on these design parameters and, in general, the results were found to be in good agreement with the theoretical analysis where discrepancies were found, a suitable explanation was considered.

Following this, then four different types of solid core PCFs were experimentally investigated for their suitability as transverse force sensor elements in a fibre loop mirror (FLM) configuration. It was shown that not only specifically designed Hi-Bi fibres are suitable for that purpose but also standard hexagonal ones with low birefringence, offered even higher sensitivity and less dependence on the fibre orientation.

The work undertaken has thus demonstrated the potential of fibres of this type in force/pressure measurement, taking the advantage of these fibres being insensitive to temperature variations and the flexibility in the design of the cross-sectional micro-structures.

Also it was shown that these fibres offering acceptable sensitivity for short length low birefringence fibres when they join together.

Chapter 5

Application

5.1 Introduction

In this chapter, the analysed sensing technique in chapters three and four have been used for the in situ detection of steel corrosion distributed in reinforced concrete structures.

Over the past century, reinforced concrete has become the most widely used construction material in the built environment [246]. One of the key challenges facing the industry is to design reinforced concrete that will stand the test of time while retaining its integrity during the expected lifespan. One of the main pitfalls of concrete as a construction material is its inability to fully prevent corrosion of the reinforcing steel.

While much advancement has been made in terms of protecting against corrosion (i.e., improvements in concrete durability), there is always the risk that corrosion may occur. As a result, corrosion monitoring in concrete structures has now become a major component of the design process. The importance of this was properly recognized in the late 1970 s [247], after the degradation of reinforced concrete structures by corrosion was seen as a reality.

At present, a number of techniques are available to assess the likelihood of reinforcement corrosion in concrete structures [248]–[250]. These include electrochemical techniques which, under normal working conditions, can give reasonably accurate information relating to parameters such as the steel corrosion rate and the chloride ion concentration. However, with each of these techniques it is difficult to achieve continuous measurement and in most cases rigorous surveys must be carried out manually, on site.

Optical fibre sensors (OFSs) are now becoming increasingly popular in the field of structural health monitoring (SHM). Compared to conventional electrochemical sensing techniques, OFSs have many characteristics which make them more favourable for SHM including: small size and light weight, immunity to electromagnetic interference, stability of material and good multiplexing capabilities [251]. The concept of SHM using OFSs has been recognized for some time although the industry has been very slow to implement and standardize many such proven forms of measurement. This is mainly due to the high cost of the existing OFS systems and some key issues which require to be addressed to meet industrial standards, such as durability and long term stability.

Over the past decade, the potential for using OFS techniques to monitor the corrosion of metals has been explored. The most popular method has been to replace part of a fibre cladding with the metal under study and monitor changes in transmitted power due to corrosion [251], [252]. This technique

simulates what may happen with nearby steel reinforcement, however, no information on the actual rebar corrosion is provided. In addition, the sensing principle is usually intensity-based, which is known to suffer from limitations of low signal-to-noise ratio and inaccuracy due to fluctuations of the light source. The long period grating-based technique has also been reported for monitoring the corrosion of reinforcement in concrete [253], [254] which takes full advantage of fibre sensitivity to the refractive index variation of the surrounding environment caused by the changes in ion concentrations [255], [256]. More recently, strain measurements using Fibre Bragg Gratings have been reported, in an attempt to directly monitor the corrosion at the steel-concrete interface [257]–[262].

However, the above OFS techniques can only be used to monitor corrosion at discrete locations where the sensors are installed, but the initiation of corrosion may occur at any point of the rebar, even at locations where there is no sensor installed.

Therefore, there is a real need for a monitoring system which is able to alert the onset of corrosion irrespective of its location.

This chapter aims to address this challenge by using a force sensing technique based on the polarization characteristics of a polarization-maintaining photonic crystal fibre (PCFs), which evaluated in chapter four in an attempt to accurately determine the onset and development of corrosion along embedded reinforcement bars.

5.2 Principle, fabrication and instrumentation

Corrosion is an electrochemical process involving chemical reactions and the flow of current between anodic and cathodic sites on the metal surface. When steel corrodes in concrete, rust is deposited at the anodic site (area of steel that has a more positive potential in relation to the cathode) and can occupy a volume many times the volume of the original metal [263]. The expansive forces can eventually exceed the tensile strength of the surrounding concrete, leading to cracking and degradation of the structure.

This chapter focus on the development of a fully distributed sensor system using a birefringent PCF which is able to capture the expansion force caused by this rust-forming process.

The sensitivity of birefringent PCFs to changes in applied force was evaluated in chapter three and four.

For this study, the HiBi PCF type 070107 P2 was chosen due to its higher sensitivity and sharp

interference pattern at relatively short lengths.

The setup explained in figure 4.5 has been used for aligning the sensing fibre before mounting on a steel rebar.

A HiBi PCF of L = 170 mm was fusion spliced to two lengths of SMFs and inserted into the rotators. A schematic of the alignment process is shown in figure 5.1.

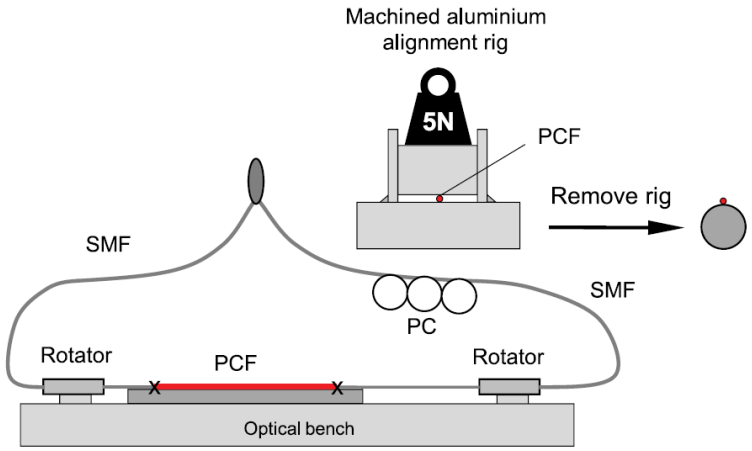

Figure 5.1 Schematic of the alignment rig used in this paper.

It was found that a 5N weight applied on a 4×4 cm produced a peak shift of 1 nm (0.125 N/mm → 1 nm). Figure 5.2 (a) shows the wavelength shift of the sensor when a fixed load of 5 N is positioned at any point along the length of the sensing fibre. It is noted that the force sensitivity of this distributed sensor is constant irrespective of the location of the force.

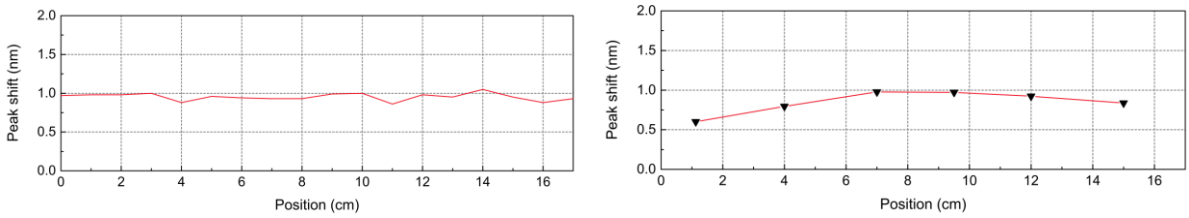

Figure 5.2 (a) Sensor alignment at a constant load of 5 N before mounting on the rebar. (b) Sensor response to 5 N after mounting to rebar.

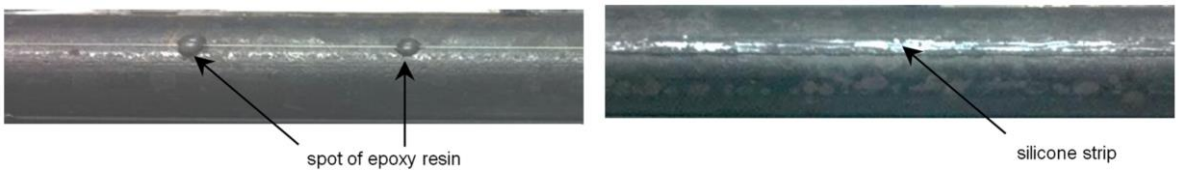

(a) (b)

Figure 5.3 (a) Instrumated rebar with unprotected sensor. (b) Instrumented rebar with sensor protected by a thin layer of silicone.

When the alignment was achieved, the rebar was gently positioned underneath the sensing fibre and spot-glued using rapid set epoxy. The sensor response after mounting on the rebar was evaluated by balancing the 5 N weight at positions between each of the epoxy points. It was found that the sensitivity had reduced slightly near the ends of the sensor as shown in figure 5.2 (b). This loss in sensitivity was likely due to an effect induced by the hardened epoxy covering the end splices. Figure 5.3 shows the rebar instrumented with a bare (unprotected) sensor and a sensor protected by a thin layer of silicone. The protected sensor did not respond to the 5 N check due to the reduced sensitivity as a result of the protection, however a positive response occurred by manually exerting additional pressure.

For each sensor, a hairpin loop was made with one of the free SMF ends, directed back to the top of the rebar and fixed into position using epoxy. Isolating heatshrink was used to confine the corroding area of the rebar to the sensing length. All splices were coated with a thin layer of epoxy and located underneath the heatshrink (outside the corroding zones).

5.3 Accelerated corrosion tests

Corrosion of steel in concrete *in situ* in many installations may take months to initiate, even if accelerated in the laboratory by exposing to either CO2 or chloride. As corrosion is an electrochemical reaction, electrical methods can be used to force corrosion [264]. This can be achieved in the laboratory by immersing a concrete-steel specimen in a solution of NaCl and connecting to a current source as shown in figure 5.4. The experimental program thus developed has been divided into two phases.

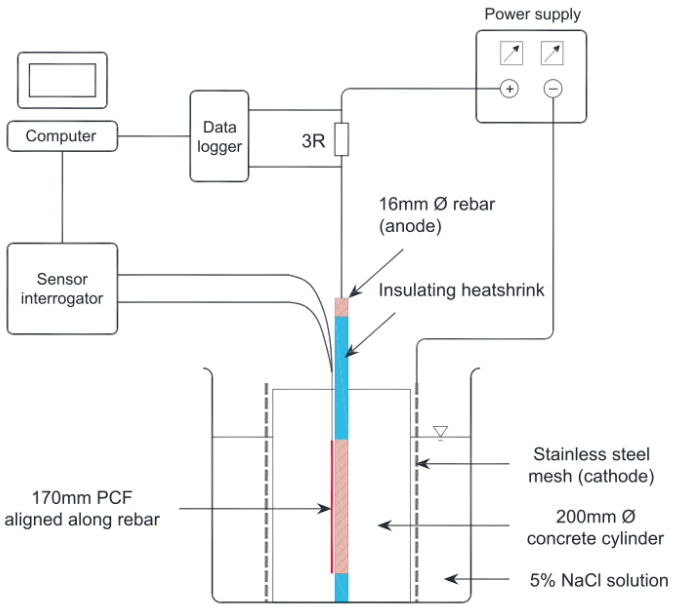

Figure 5.4 Accelerated corrosion test setup.

A. Demonstration of the Sensing Principle (Rebar 1)

The purpose of this was to transfer the sensing principle demonstrated using laboratory weights, in which a rapid accelerated corrosion trial of the bare PCF on the instrumented rebar is necessary. For this part, an accelerating current is applied, disconnected, and reapplied again to demonstrate whether peak shifts correspond to changes in corrosion rate.

B. Accelerated Corrosion on Protected and Unprotected PCFs (Rebar 2)

One of the major concerns with any sensing fibre is its durability when exposed to the wet and hardened concrete environment.

Thus in this test, by mounting two sensors on opposite sides of the rebar [(one bare, and the other protected using the approach illustrated in figure 5.3 [(a) and (b)], a direct comparison could be made between sensors to investigate the effect of using protection (thin silicone coating). The accelerating current would also be monitored throughout the experiment.

For the concrete, a typical mix was prepared with a cement: sand: gravel weight ratio of 1:2:2.25 and a water/cement ratio of 0.5 (for Rebar 2, salt was added during mixing). The concrete was poured and gently compacted into a prepared cylindrical mould with the sensor/rebar centrally positioned. Both ends of the SMF were connected to a coupler enabling connection to the sensor interrogator (Micron Optics SM125 which is used to replace the OSA and the light source shown in Fig. 1). As the SMF fibres are not polarization maintaining, it was necessary to adjust the polarization conditions observed to generate the optimum spectral interference pattern (i.e. with maximum extinction ratio so that distinct peaks/valleys can be processed by the peak/valley detection and tracking algorithm). This was achieved by forming small loops with the SMF and arbitrarily adjusting the orientation (similar to the PC in figure 5.1) before fixing in position at the optimum pattern and peak tracking was initiated in the detection system. The concrete was cured at room temperature under moist conditions for two weeks, then demoulded and immersed in water. The peaks were then observed to test the stability under saturated conditions. After the signal had stabilized, salt was added to Rebar 1 and an accelerating voltage of 30 V was applied between the rebar and the mesh, as shown in figure 5.4.

5.4 Results and discussion

A. Rebar 1

Almost immediately after the current was initiated, the peaks of the interference pattern began to shift dramatically and at a steady rate. To confirm that this was due to the corrosion acceleration effect, the current was switched off temporarily at 20 days (as can be seen from figure 5.5).

An effect was seen immediately whereby the peaks initially stabilized and then slowly shifted downwards. On the assumption that the detected pressure was from the rapid build up of hydrated ferric oxide (rust), it would be expected that the pressure would dissipate slightly as the products relax into the concrete pores. After a dormant period of 0.5 days, the accelerating current was reapplied and again positive shifts in the peak positions could be seen almost immediately. The constant pressure induced by the constant accelerating voltage was seen to lead to a linear peak shift response (as expected from 3).

B. Rebar 2

As salt was already included within the concrete mix, a significant peak shift was detected by the bare sensor during the curing stage (a gradual peak shift by 6 nm was seen) as shown in figure 5.6.

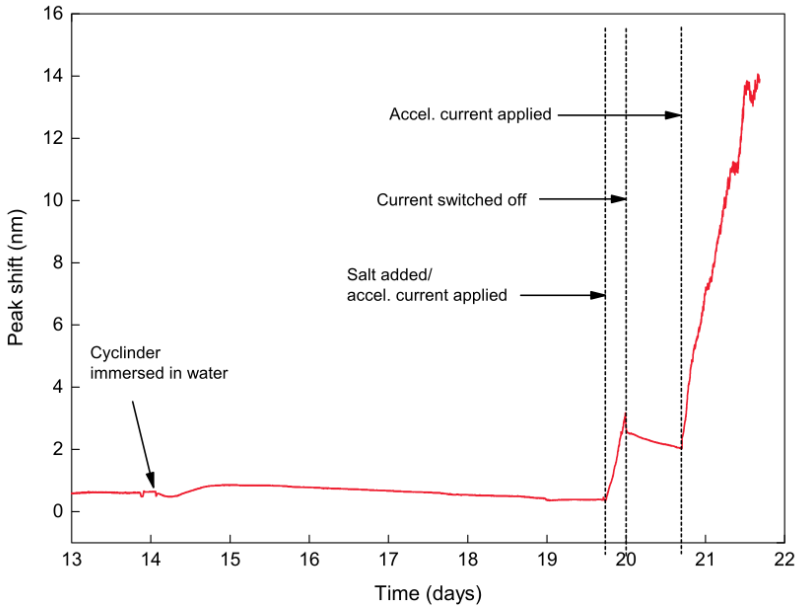

Figure 5.5. Validation of sensing concept using the accelerated corrosion test (Rebar 1).

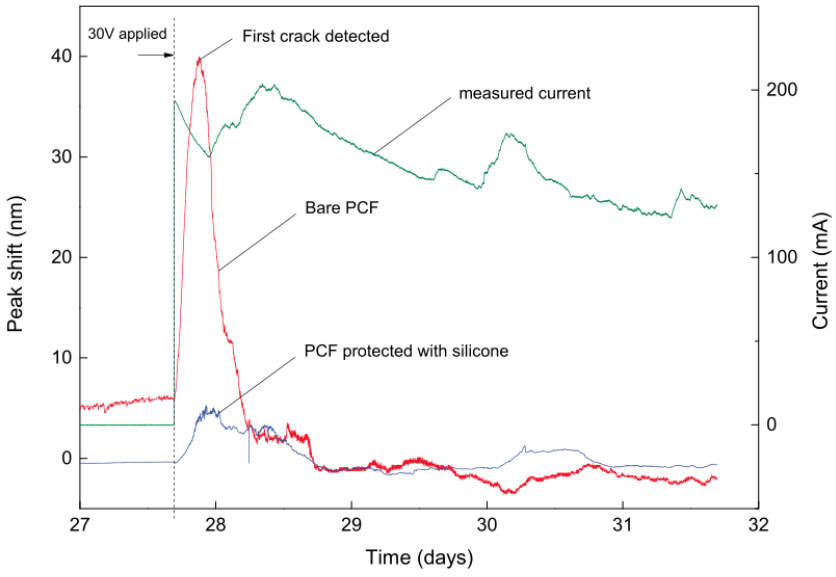

Figure 5.6. Behaviour of bare and silicone-protected PCFs under accelerated corrosion (Rebar 2).

Once the peaks began to stabilize, the accelerating current was applied. Within minutes, the peak began to shift at a rapid rate. The protected silicone PCF showed an increase in the peak shift at a lower rate compared to that seen for the bare PCF.

However, the rate of increase was much greater than in the previous trial (rebar 1) which is likely due to adding salt at the mixing phase. While the sensitivity of the protected fibre is still seen to be lower, there was no delay in the reaction time. In Fig. 7, the measured accelerating current is also shown. The peak currents correspond to where the crack openings in the concrete are observed, as shown in figure 5.7.

The opening of cracks allows more moisture/chloride to penetrate, which in turn leads to an increase in the corrosion rate.

After the first main corrosion event, the bare sensor no longer responds to changes in corrosion rate, however, the protected fibre responds to subsequent increases in the corrosion rate (the peak is seen at ~30.5 days). It was subsequently found that the bare sensor was damaged after the first crack was formed, therefore it could not respond to any further cracking events. However, the protected sensor has been able to survive over the entire testing period and retain sufficient sensitivity to detect subsequent cracking in addition to the first.

Figure 5.7. Photo of corroding cylinder.

5.5 Summary

This preliminary study has demonstrated that HiBi PCF fibres show excellent potential for effective *in situ* monitoring of the corrosion of reinforcing steel in concrete from the point where such corrosion has been initiated. Very useful information can thus be obtained from the sensors, showing a direct relationship between the measured pressure and the corrosion rate of the rebar.

This direct sensing approach not only provides information on the corrosion rate itself but also acts as an ideal sensor for crack detection. The data obtained also allows an analysis of the direct stresses induced by the expansive corrosion reaction, which enable a furtherance of the better understanding of many aspects of topical civil engineering research. With a constant sensitivity achieved over the whole length of the sensing fibre, there is significant potential to embed such sensors along an entire length of rebar at selected points to determine stresses and cracking that occurs.

CHAPTER 6

Conclusions and Future Work

6.1 Summary and Conclusions

The work carried out in this thesis aimed to develop a novel, optical pressure/force sensor using PM optical fibres, based solidly on the theoretical analysis of such fibres and their birefringence characteristics as a function of applied force/pressure. Based on the results obtained from this research and the achievements attained, the following summary of the work done and the conclusions made:

- A review of conventional sensor systems, including different optical technologies used for pressure/force measurement, was made with several essential limitations being highlighted.

This thesis has covered the theory, design, development, performance and laboratory investigation of different types of polarization-maintaining optical fibre sensors when they are subjected to external perturbation, such as transverse pressure/force. The material birefringence of an asymmetrical fibre was calculated using a thermo-elastic displacement potential method through the superposition of sectional displacement potentials. This involved the important theoretical analysis of two different types of fibre designs, i.e. Polarization-Maintaining side hole fibre(s) with one or two hole(s) located in their cladding showing the potential of using such PM fibres for pressure/force measurement based on the birefringence characteristics of the fibres exposed to a transverse force. The methodology used is generic, and thus applicable to any one-hole fibre structure, should the hole diameter or position vary in the fibre cladding, or the fibre hole be empty or filled in with any material. This enables the analysis to be applied more widely in a range of optical fibre sensor applications.

The following specific goals have been achieved with real application potential

- Direct measurement of transverse force through the interrogation of induced birefringence variation has been investigated in this thesis by using two specialist single mode Polarisation-Maintaining (PM) side-hole(s) fibres and also four different types of Hi-Bi and low-Bi PCFs.
- Variations in the pressure sensitivity of the PM fibres with different orientation and magnitudes of the applied external force have been investigated both

theoretically and experimentally and it was confirmed that they are dependent upon sseveral key parameters of the system, including the fibre structure, the magnitude and the direction of the applied external force, the fibre length used and the birefringence of the fibre.

- The theoretical data obtained have shown a good agreement with those from experiments, confirming the suitability of the use of such PM fibres for the measurement of pressure, force and mass of an object, applied in different directions, over a wide range and in real time.
- The results obtained show that PCFs of low birefringence are more sensitive than those of high birefringence (Hi-Bi) although the former require a longer length to achieve a similar level of birefringence. Compared to conventional Hi-Bi fibres (e.g. Panda and Bow-Tie fibres), PCFs have demonstrated much lower temperature sensitivity and this suggests that they are well suited to measure pressure, force, and mass in real time when temperature varies by using a fibre loop mirror (FLM) configuration. To solve the length problem in the low birefringence PCFs, a joint PCF approach was used by fusion-splicing a short length of Low-Bi with a short section of a Hi-Bi PCF and their sensitivity to lateral pressure was investigated and reported in detail in this thesis. To achieve the best results, a polarization controller was used in a fibre loop mirror to ensure that the two joint PCFs maintained the same birefringence state angle. The results obtained show that the sensitivity of the joint fibres was lower than that of a single PCF with low and medium birefringence but more sensitive than that of the single high birefringent PCF.
- A novel sensing technique has been designed and investigated for the direct, in situ detection of steel corrosion distributed in reinforced concrete structures. This new type of sensor not only determines the onset of corrosion but also allows for better monitoring along the length of a reinforcement bar.

6.2 Future work

The results obtained and reported in this thesis have shown that fibre structures play an important role in determining the sensitivity for pressure/force measurement therefore it is important to create a generic analytical model for fibre birefringence analysis, taking into account the complex fibre structures and thus the modelling results obtained would provide an important guidance for the fibre design, fabrication and optimization for various sensing purposes.

The theoretical analysis in this thesis is based on the assumption that fibre shape is considered to be unchanged while the lateral pressure/force is applied. This introduces a discrepancy between the theoretical and experimental data obtained, in particular, when the applied force is increased above a certain level. Therefore it would be useful to consider the fibre 'distortion' in the theoretical analysis when the applied force/pressure is varied and this would lead to a closer match between the theoretical and experimental

The location of the applied force and its applied direction are usually required – so it would be important to work out a strategy which allows for multi-parameter measurement

The sensor sensitivity is dependent on the orientation of the fibre, a new hallow core fibres could be a good choice to be used as a lateral pressure sensor as they have low sensitivity to temperature and high sensitivity to pressure, also they are not sensitive to direction.

Joint fibres have investigated in this thesis for few PCFs, It can be developed for different types of fibres and also evaluate the fibres behaviour in the joint area, as the cross section of PCFs are different, light could be show different response to the pressure at the junction area for different PCFs

It would be useful to see the use of PM fibres for industrial applications, for example, for structural condition monitoring, based on the success of the preliminary studies detailed in Chapter 5, where birefringent PCF fibres have been used successfully for corrosion onset monitoring. More systematic evaluations are required to allow correlations to be made between the weight loss and the measured corrosion current/pressure variation.

Other aspects of sensor development should be focused on sensor protection, corrosion location identification and determination of corrosion rate, thus creating sensor design improvements to meet industrial needs.

References

1. K.T.V. Grattan and B.T. Meggitt "Optical Fibre Sensor Technology", Kluwer Academic Publishers, The Netherlands, 2000, Page 175
2. *(Source: http://optics.org/news/3/6/27/SENSORSM*)
3. BCC Research reports, "Market Research Reports and Technical Publications Product Catalog" December 2012, (*http://www.bccresearch.com/market-research/instrumentation-and-sensors/fiber-optic-sensors-market-technology-ias002e.html)*
4. K. Simony, "A Cultural History of Physics", CRC Press, 2012, Page 237
5. J. Elliot and D. Bethun, "Life of Galileo Galilei: With Illustrations of the Advancement of, Experimental Philosophy", William Hyde &company, 1832, Page 266
6. J. Unkart, "Offshore, Rigging and Tactics by a Professional with 40 Years of Experience" Geared Up Publications, 2012, Page 200
7. K. Park and L. Daston, "The Cambridge History of Science: Volume 3, Early Modern Science", Cambridge University Press, 2006, Page 27
8. J. R. Smith, "From plane to spheroid: determining the figure of the earth from 3000 B.C. to the 18th century Lapland and Peruvian survey expeditions", Landmark Enterprises, 1986, Page 53
9. H. W. Keller, "History of Pressure and Pressure Measurement", http://www.keller-druck.es/es/info/historia_de_la_presion, 2004
10. D. Group, "The Facts on File Physics Handbook", Infobase Publishing, 2009
11. F. Close, "Nothing: A Very Short Introduction", Oxford University Press, 2009
12. J. Fraden, "Handbook of modern sensors, physics, design and application", Third edition, Springer, 2004, Page 104
13. S.S. Zumdahl and S. A. Zumdahl, "Chemistry: An Atoms First Approach", Cengage Learning, 2011, Page 321
14. F. Pavese and G. Molinar, M. Beciet, "Modern Gas-Based Temperature and Pressure Measurements", Springer, 2012, Page 8
15. J. L. Heilbron, "The Oxford Guide to the History of Physics and Astronomy", Volume 10, Oxford University Press, 2005, Page 27

16. B. Hollembeak, “Today's Technician: Advanced Automotive Electronic Systems”, Cengage Learning, 2010
17. A. K. Bewoor and V.A. Kulkarni, “Metrology & Measurement”, McGraw Hill, (2009), Page 475
18. A. Blake, “Handbook of mechanics, materials, and structures”, Wiley, 1985, Page 397
19. A.E. Kubba1, and K. Jiang, “A Comprehensive Study on Technologies of Tyre Monitoring Systems and Possible Energy Solutions”, Sensors (Basel). Jun 2014; 14(6): Pages 10306–10345.
20. Majumdar, “Oil Hydraulic Systems: Principles and Maintenance”, McGraw-Hill Education, 2000.
21. J.W. Dally, W.F Rifley, K.G McConnell, “Instrumentation for engineering measurements”, 2nd edn, John Wiley, New York. 1993
22. F.S Figliola and D.E Beasley, “Theory and design for mechanical measurements”, 3rd edition, John Wiley, New York. 2000
23. L. Finkelstein and K.T.V Grattan, “Concise encyclopaedia of measurement & instrumentation”, Pergamon Press Ltd., Oxford. 1994
24. W. Gopel, J. Hesse and J.N Zemel, “Sensors, a comprehensive survey”, VCH publishers Inc., Volume 1, New York. 1989
25. E.O. Doebellin, “Measurement systems, application and design”, 4th ed. McGraw Hill, New York. 1990
26. S.A. Sharifian, “Fibre optic pressure transducers for disturbance measurements in transient aerodynamic research facilities”, PhD Dissertation, University of Southern Queensland, 2003
27. J.W. Dally and G. L. Pertmer, “Introduction to Engineering Design: Anti-icing Systems for Highway Bridges”, College House Enterprises, LLC, 2004, Page 92
28. S.P Beeby, “Mems Mechanical Sensors”, Artech House Inc, 2004, Page 85
29. N.P. Cheremisinoff and P. N. Cheremisinoff, “Instrumentation for process flow engineering”, Technomic Pub. Co., 1987, Page.136
30. J.R Carstens, “Electrical sensors and transducers”, Regents and Prentice Hall, New Jersey, 1993, Page 252
31. C. H. Sherman and J L. Butler, “Transducers and Arrays for Underwater Sound”, Springer, 2007, Page 105

32. S.K. Singh, “Industrial Instrumentation and Control”, Tata McGraw-Hill, 2003
33. L. K. Baxter, “Capacitive Sensors: Design and Applications”, John Wiley & Sons, 1996, Page 125
34. T. Pownall,”Sensors, principles & applications”, Prentice Hall International Ltd, UK. 1993
35. T. M. Adams, R A. Layton, “Introductory MEMS Fabrication and Applications”, Springer, 2009, Page 211
36. J. Fraden, “AIP handbook of modern sensors: physics, designs, and applications”, American Institute of Physics, 1993
37. I. Sinclair, “Sensors and Transducers”, Newnes, 2000, Page 88
38. http://www.digikey.com/en/articles/techzone/2012/jun/keeping-track-of-industrial-processes-with-sensors
39. H. D. C. Smyth, “Advances In Delivery Science and Technology: Controlled Pulmonary Drug Delivery”, Springer, 2011
40. B. Eggins, “Biosensors”, Wiley and Teubner, Chichester1996.
41. J. D. Turner, “Automotive Sensors”, Momentum Press, 2009
42. L.A. Freeman, M. C. Carpenter, D. O. Rosenberry, J. P. Rousseau, R. Unger, and J. S. McLean, “Use Of Submersible Pressure Transducers In Water-Resources Investigations”, Chapter A of Book 8, Instrumentation Section A, Instruments for Measurement of Water Level, U.S. Geological Survey, Reston, Virginia, 2004
43. D. Goff, “ Fiber optic video transmission, the complet guide”, Taylor & Francis publication, 2013, Page 21
44. N.V. Jones, “Telecommunications Management”, Lightning Source Incorporated, 2004
45. D. Malacara and B. J. Tompson, “Handbook of Optical Engineering”, CRC Press, 2001, Page 775
46. J. Hecht, “City of Light: The Story of Fiber Optics”, Oxford University Press, 2004, Page 55
47. Menadier, C. Kissinger and H. Adkins, “The fotonic sensor”, Instruments and Control Systems”, Volume 40, 1967, Page 114
48. E. Snitzer, “Laser in glass technology”, American ceramic society bulletin, Volume 50 Issue: 9 1971, Page 767

49. J. H. Cole, R. L. Johnson, and P. G. Bhuta, “Fiber optic detection of sound”, J. Acoust. Soc. Am. Volume 62, Issue 5, 1977, Pages 1136-1138,
50. J.A. Bucaro, H.D. Dardy, and E.F. Carome, “Fiber-optic hydrophone”, J. Acoust. Soc. Am., Volume 52, 1977, Page 1302
51. B. Lee “Review of the present status of optical fiber sensors”, Optical Fiber Technology 9, 2003, Pages 57–79
52. K.T.V. Grattan and T. Sun, “Fiber optic sensor technology: an overview”, Sensors and Actuators A, Volume 82, 2000, Pages 40–61
53. B. Lee, “Review of the present status of optical fiber sensors, Optical Fiber Technology”, Volume 9, 2003, Pages 57–79,
54. R. Bogue, “Fibre optic sensors: a review of today's applications”, SENSOR REVIEW Volume: 31 Issue: 4, 2011, Pages 304-309
55. T.R. Wolinski, and A.W Domanski, “Polarimetric optical fiber sensors of a new generation for industrial Applications”, Bulletin of the Polish Academy of Science: Technical Sciences, Volume 56, No. 2, 2008
56. J.S Yang, C.J Lee and C.H Wei, “ Fiber-optic chemical sensors: A general review”, Journal of the Chinese chemical society, Volume: 49 Issue: 5, 2002, Pages: 677-692,
57. K. K. K. Annamdas and V. G. Annamdas, “Review on Developments in Fiber Optical Sensors and Applications”, SPIE, Volume 7677, 2010
58. N.T. Aleksandr, Y. S Oleg and A.T Nikolay “Numerical analysis of residual stresses in preform of stress applying part for PANDA-type polarization maintaining optical fibers”, Optical Fiber Technology, 2010, pages 156-161.
59. P. L. Chu and R. A. Sammut, "Analytical Method for Calculation of Stresses and Material Birefringence in Polarization-Maintaining Optical Fiber", Journal of Lightwave Technology, Volume LT- 2 No.5, 1984, pages 650-662.
60. J.I. Sakai and T Kimura,” Birefringence and Polarization Characteristics of Single-Mode Optical Fibers under Elastic Deformations”, IEEE Journal of Quantum Electronics, Volume 17, Issue: 6, 1981, Pages 1041 – 1051.
61. E. Pinet, “Pressure measurement with fiber-optic sensors: commercial technologies and applications”, SPIE, Volume 7753, 775304, 2011

62. G.B. Hocker," Fiber optic sensing of pressure and temperature", Applied Optic, Volume 18 No.9, 1979, pages 1445-1448.
63. J.N. Fields, C.K. Asawa, O.G. Rammer, and M.K Barnoski, "Fiber optic pressure sensor", J. Acoust. Soc. Am. 67(3), Mar. 1980
64. W.B. Spillman, "Multimode fiber optic pressure sensor based on the photoelastic effect", Opt. Lett.7, 388, 1982
65. H.M. Xie, P.H. Dabkeiwicz, and R. Ulrich,"Side-hole for fiber-optic pressure sensing", Opt. Lett., Volume 11, No.5, May 1986.
66. J.C. Knight, T. A. Birks, P. St. J. Russell, and D. M. Atkin, "All-silica single-mode optical fiber with photonic crystal cladding", Opt. Lett., Volume 21, pp. 1547–1549, 1996.
67. M. Yasin, S. W. Harun, and H. Arof, "Recent progress in optical fiber research", InTech publication, (2012) Pages 193-228.
68. O. Fraza, J. L. Santos, F. M. Araujo, and L. A. Ferreira, "Optical sensing with photonic crystal fibers," Laser & Photon. Rev., Volume 2, no. 6, 2008, Pages 449–459
69. Y. Jin, C. C. Chan, Y. Zhang, X. Dong, and P. Zu, "Temperature sensor based on a pressure-induced birefringent single-mode fiber loop mirror," Meas. Sci. Technol., Volume 21, (2010) Pages. 065204.
70. T. Martynkien, G. Statkiewicz-Barabach, J. Olszewski, J. Wojcik. "Highly birefringent microstructure fibers with enhanced sensitivity to hydrostatic pressure," Optics Express, Volume 18, no. 14, 2010, Pages 15113–15121.
71. H. Y. Fu, C. Wu, M. L. V. Tse, L. Zhang, K.-C. Davis Cheng, H. Y. Tam, B.-O. Guan, and C. Lu, "High pressure sensor based on photonic crystal fiber for downhole application," Appl. Opt., Volume 49, no. 14, 2010, Pages 2639–2643
72. J. R. Clowes, S. Syngellakis, and M. N. Zervas," Pressure sensitivity of side-hole optical fiber sensor", IEEE Photonics Technology Letter, Volume 10, 1998, Pages 857 -859,
73. R. Passy, A. L. Gama, N. Gisin, and J. P. Von Der Weid, "Pressure dependence of polarization mode dispersion in HiBi fiber", J. Lightwave Technol., Volume 10, 1992, Pages 1527 -1531,
74. W.J. Bock and T.A. Eftimov, "Simultaneous hydrostatic pressure and temperature measurement employing an LP_{01}-LP_{11} fiber-optic polarization-sensitive intermodal interferometer," IEEE Trans. Instrum. Meas., Volume 43, Feb 1994, Pages 337–340,

75. W.J. Bock and W. Urbanczyk, “Coherence multiplexing of fiber optic pressure and temperature sensors based on highly birefringent fiber,” IEEE Trans. Instrum. Meas., Volume 49, Feb. 2000, Pages 392–397
76. G.L. Mitchell, “Intensity based and Fabry-Perot interferometer sensors in Fiber Optics Sensors: An Introduction for Engineers and Scientists” New York: Wiley Interscience, 199,1 Page 139,
77. E. Pinet, “Fabry-Perot Fiber-Optic Sensors for Physical Parameters Measurement in Challenging Conditions” Hindawi Publishing Corporation Journal of Sensors Volume 2009, Article ID 720980, page 9
78. D. C. Abeysinghe, S. Dasgupta, J. T. Boyd, and H. E. Jackson “A novel MEMS pressure sensor fabricated on an optical fiber”, IEEE Photonic Technology Letter, Vol. 13, No. 9, Sep. 2001
79. C. Zhang, G. Kai, Z. Wang, T. Sun, Y. Liu, W. Zhang, S. Yuan and X. Dong, “Study on polarization properties of birefringent microstructure fiber with lateral pressure,” Proc. of SPIE, Volume 6019, 2005 Pages 60193B
80. H. Liu, W. Zhang, Q. Tu, M. Jiang, Z. Wang, Y. Liu, G. Kai, X. Dong, “The research of propagation constant in grapefruit microstructure optical fibers with lateral pressure”, Preceding of SPIE, Volume 6595, 65953W, 2007.
81. T. Geenaert, G. Luyckx, E. Voet, T. Nasilowski, K. Chah, M. Becker, “Transversal load sensing with fiber bragg gratings in micro structured optical fibres,” IEEE Photonics Technology Letter, Volume 21, no. 1, 2009 Pages 6–8.
82. H. M. Kim, T. H. Kim, B. Kim, and Y. Chung, “Enhanced transverse force sensitivity by using a highly birefringent photonic crystal fiber with larger air holes on one axis,” Appl. Opt., Volume 49, no. 20, 2010 Pages 3841–3845
83. S. Sonnenfeld, T. Sulejmani, S. Geernaert, E.N. Lammens, G. Luyckx, “Microstructured optical fiber sensors embedded in a laminate composite for smart material applications,” Sensors, Volume 11, no 3, 2011 Pages 2566–2579
84. P. Zu, C.C. Chan, Y. Jin, Y. Zhang, and X. Dong, “Fabrication of a temperature-insensitive transverse mechanical load sensor by using a photonic crystal fiber-based Sagnac loop,” Meas. Sci. Technol., Volume 22, no. 2, 2011.

85. I.R. Walker, “Reliability in Scientific Research: Improving the Dependability of Measurements, Calculations, Equipment, and Software”, Cambridge University Press, 2011
86. H.N. Li, D. S. Li and G. B. Song, “Recent application of fiber optic sensors to health monitoring in civil engineering”, Engineering structures, 26, 2004 Pages 1647-1657,
87. J. Wang, B. Dong, E. Lally, J. Gong, M. Han and A. Wang,” Multiplexed high temperature sensing with sapphire fiber air gap-based extrinsic Fabry–Perot interferometers”, Opt. Lett., Volume 35, No. 5, 2010
88. A.S Morris and R. Langari, “Measurement and Instrumentation: Theory and Application”, Academic Press, 2011
89. V. Kondratov and V. Redko, “Classification of Fiber-Optic Pressure Sensors with Amplitude Modulation of Optical Signal”, Sensors & Transducers Journal, Volume 100, Issue 1, 2009, Pages 146-160
90. M. Kimura and K. Toshima, “Vibration sensor using optical-fiber cantilever with bulb-lens”, Sensors and Actuators A, Volume 66, 1998, Pages 178-183,
91. P. D. Scholz, A. Schlachetzki and P. Hauptmann, “A micromachined vibration sensor based on the control of power transmitted between optical fibres”, Sensors and Actuators A, Volume 65, 1998, Pages 23-29.
92. J. Powers. “An Introduction to Fiber Optic Systems”. Homewood, IL, Richard D. Irwin, Inc. and Aksen Associates, Inc, 1993.
93. B. P. Pal, “Fundamentals of Fibre Optics In Telecommunication And Sensor Systems”, bohem press, 1992
94. US Patent No. 5005584, “Fiber optic pressure transducer”, issued Apr. 9, 1991 to R. L. Little.
95. US Patent No. 4611600, “Optical fiber pressure transducer”, issued Sep. 16, 1986 to D. M. Cohen.
96. A. Badeeva, A. G. Pivkin, V. A. Mescheryakov and T. I. Murashkina, “Fiber-optic pressure sensor of attenuation type for aircrafts”, Sensors and Systems, 4, pp. 11–14, 2003
97. A.N. Chester and S. Martellucci, “Optical Fiber Sensors” Dordrecht, Martinus Nijhoff Publishers, 1987.
98. D. A. Krohn, “Fiber optic sensors: fundamentals and applications”, ISA, 2000

99. US Patent No. 4293188, “Fiber optic small displacement sensor”, issued Oct. 6, 1981 to D. H. McMahon.
100. D.A. Krohn, “Intensity Modulated Fiber Optic Sensors Overview”, SPIE Volume 718 Fiber Optic and Laser Sensors IV, 1986
101. E. Udd. “Fiber optic smart structures.” Proceedings of the IEEE, Volume84, Iss.6, 1996 Pages 884-894
102. S. Nesson, “Miniature fiber optic pressure sensors for intervertebral disc pressure measurements in podents”, Silas Carl Nesson, 2007
103. C.M. Miller, S.C. Mettler and I.A. White, “Optical Fiber Splices and Connectors: Theory and Methods”, Marcel Dekker, Inc., ISBN 0-8247-7520- 1, 1986.
104. E. Toba, K. Riku, K. Ito and K. Taguchi, “Measurement of microscopic displacement and vibration of tympanic membranes by means of fiber optics”, Journal of Robotics and Mechatronics, Volume, 3, No. 2, 1991, pages 74-78.
105. J. Zheng and S. Albin, "Self-referenced reflective intensity modulated fiber-optic displacement sensor." Optical Engineering. Volume 38, 1999 Pages 227-232
106. G. Berkovic and E. Shafir, “Optical methods for distance and displacement measurements”, Advances in Optics and Photonics 4, 2012 Pages 441–471,
107. C.M. Davis, “Fiber optic sensors: an overview”, SPIE Volume 478 Fiber Optic and Laser Sensors II, 1984
108. K. Bergmeister, “Monitoring and Safety Evaluation of Existing Concrete Structures: State-of-art Report”, FIB - Féd. Int. du Béton, 2003
109. W.B. Spellman and D. H. McMahon, “Frustxated-total-internal- reflection multimode fiber optic hydrophone,” Appl. Opt., Volume 19, 1980 Pages 113-117,
110. K.T.V. Grattan, A. W. Palmer and D. P. S. Saini, “Frustrated-Total internal reflection, fiber optic pressure sensor”, Journal of Lightwave Technology, Volume LT-3. NO. 5, October 1985
111. T.G. Giallorenzi, J. A. Bucaro, A. Dandridge, G. H. Sigel, J. R., James H. Cole, S. C. Rkshlegh and R. G. Priest, “Optical Fiber Sensor Technology”, IEEE Journal of Quantum Electronics, volume 18 , Issue: 14 , 1982, pages 626-665
112. J.N. Fields and J. H. Cole, "Fiber Microbend Acoustic Sensor," Appi. Opt. 19, 3265, 1980, pages 3265-3267

113. US Patent No. 4918305, “Fiber optic pressure sensor using pressure sensitive fiber different from input and output fibers”, issued Apr. 17, 1990 to M. T. Wlodarczyk, M. K. Krage and D. J. Vickers.
114. N. Lagakos, W.J. Trott, and J.A. Bucaro "Microbending Fiber Optic Sensor Design Optimization," IEEE Journal of Quantum Electronics, volume 17 , Issue: 12 , 1981, page 2454.
115. US Patent No. 4459477, “Microbending of optical fibers for remote force measurement”, issued Jul. 10, 1984 to C. K. Asawa, J. W. Austin, M. K. Barnoski, S. D. Personick and S. K. Yao.
116. D. Donlagi´c and M. Zavrˇsnik, “Fiber-optic microbend sensor structure”, Opt. Lett., Volume 22, No. 11, 1997, pages 837-839
117. J.W. Berthold, “Historical review of microbend fiber optic sensors”, Journal of Lightwave Technology, Volume: 13 , Issue: 7 , 1995
118. W.H.O. Horsthuis and J. H. J. Fluitman, "Sensitivity Dependence on Number of Bends in a Fiber Optic Microbend Pressure Sensor," NTG Fachberichte 79, 147, 1982
119. H. Whg, F. Jhj, "The Development of Fibre Optic Microbend Sensors," Sensors and Actuators, Volume 3, pp.99, 1983
120. M.B.J. Diemeer and E. S. Trommel, "Fiber Optic Microbend Sensors: Sensitivity as a Function of Distortion Wavelength," Opt. Lett. Volume 9, 1984 Page. 260-262
121. N. Lagakos and J. A. Bucaro, "Optimizing Fiber Optic Microbend Sensor," Proc. SPIE 718, 12, 1987, pages 12-20
122. S.K. Yao and C. K. Asawa, "Microbending Fiber Optic Sensing," Proc. SPIE 412, Volume 9, 1983, pages 9-13
123. K. Fidanboylu, H.S Efendioğlu, “Fiber optic sensors and their applications”, 5th International Advanced Technologies Symposium (IATS’09), Karabuk, Turkey, May 13-15, 2009,
124. V.S.J. Craig, “An historical review of surface force measurement techniques”, Physicochemical and Engineering Aspects 129-130, 1997, pages 74-94.
125. G. Kodl, “Optical waveguide pressure sensor using evanescent field”, Preceding of SPIE Volume 6758, 2007
126. G. Wild, and S Hinckley, “Acousto-Ultrasonic Optical Fiber Sensors: Overview and State-of-the-Art”, IEEE Sensos Journal, Volume 8, 2008, pages 1184-1193

127. M.T. Azar, B. Sutapun and D. Glawe, “Fiber-optic MEMS pressure sensors based on evanescent field interaction”, SPIE Volume 3276, 1998
128. F.T.S. Yu, X. Yang, “Introduction to Optical Engineering”, Cambridge University Press, 1997
129. M. Ohkawa, M. Izutsu, and T. Sueta, "Integrated optic pressure sensor on silicon substrate," Appl. Opt., Volume 28, No. 23, 1989, Pages 5153-5157.
130. K. Fischer, J. Muller, R. Hoffmann, F. Wasse, and D. Salle, "Elastooptical properties of SiON Layers in an Integrated Optical Interferometer Used as a Pressure Sensor," Journal of. Lightwave Technology, Volume 12, No. 1, 1994, Pages 163-169
131. A. Vadekar, A. Nathan, and W.P. Huang, "Analysis and Design of an Integrated Silicon ARROW Mach-Zehnder Micromechanical Interferometer," Journal of. Lightwave Technology., Volume 12, No. 1, 1994, Pages 157-162
132. A. Wagner, "Optical Pressure Sensor Based on a Mach-Zehnder Interferometer Integrated with a Lateral a-Si:H p-i-n Photodiode," IEEE Photonics Technology Letter, Volume 5, No. 10, 1993, Pages 1257-1259
133. A. Nathan, Y. Bhatnagar, A. Vadekar, and W. Huang, "Fabrication of a Silicon Mach-Zehnder Interferometer for Mechanical Measurands," Integrated Optics ad Microstructures, Proc. SPIE, Volume 1793, 1992, Pages 19-26
134. J.A. Bucaro, N. Lagakos, J. H. Cole, and T. G. Giallorenzi, "Fiber optic acoustic transduction," Physical Acoustics edited by R. H. Thurston, 16, 385, 1982
135. P. M. Junghare, S. Kulkarni, R., Mulimani, “Mach-Zehnder interferometer sensor for acoustic detection with optimal performance” IOSR Journal of Electronics and Communication Engineering (IOSRJECE), Volume 2, Issue 5, 2012, Pages 29-33,
136. N. Lagakos, E. U. Schnaus, J. H. Cole, J. Jarzynski, and J. A. Bucaro, "Optimizing fiber coatings for interferometric acoustic sensors", IEEE Journal of Quantum Electronics, 18(4), 683, 1982
137. J. Jarzynski, R. Hughes, T. R. Hickman, J. A. Bucaro, "Frequency response of interferometric fiber optic coil hydrophone," Journal of Acoustical Society of America, 69(6), 1799, 1981, pages 1799-1808
138. H.Z. Huntsville, A. Bouzid, M.A.G Abushagur, “Fiber optic pressure sensors” Proceedings IEEE Southeastcon 92, Volumes 1 , 1992

139. P. Lu, Member, G. Lin, X. Wang, L. Chen, and X. Bao, “Lateral Stress Detection Using a Tapered Fiber Mach-Zehnder Interferometer”, Photonics Technology Letters, IEEE , Volume: 24, Issue: 22 , 2012, pages 2038-2041
140. Y. Choi, M. J. Kim, and B. H. Lee, "All-fiber Mach-Zehnder type interferometers formed in photonic crystal fiber," Opt. Exp., Volume 15, no. 9, 2007, Pages 5711-5720.
141. F. Ding, A. P. Zhang, L.Y. Shao, J. H. Yan, and S. He, "Fiber-taper seeded long-period grating pair as a highly sensitive refractive-index sensor," IEEE Photonics Technology Letter, Volume 17, no. 6, 2005, Pages 1247-1249
142. H. Lim, H. S. Jang, K. S. Lee, J. C. Kim, and B. H. Lee, "Mach-Zehnder interferometer formed in a photonic crystal fiber based on a pair of long-period fiber gratings," Opt. Lett., Volume 29, no. 4, 2004, Pages 346-348,
143. W. Tao, X. Lan, and H. Xiao, "Fiber in line core-cladding-mode Mach-Zehnder interferometer fabricated by two-point CO_2 laser irradiations," IEEE Photonics Technology Letter, Volume 21, no. 10, pp. 669-671, May 2009.
144. O. Frazão, R. Falate, J. L. Fabris, J. L. Santos, L. A. Ferreira, and F. M. Araújo, "Optical inclinometer based on a single long-period fiber grating combined with a fused taper," Opt. Lett., Volume 31, no. 20, 2006, Pages 2960-2962
145. Z. Tian, S. S. H. Yam, and H. -P. Loock, "Single-mode fiber refractive index sensor based on core-offset attenuators," IEEE Photonics Technology Letter, Volume 20, no. 16, 2008, Pages 1387-1389
146. Z. Tian, S. S. H. Yam, J. Barnes, W. Bock, P. Greig, J. M. Fraser, H.-P. Loock, and R. D. Oleschuk, "Refractive index sensing with Mach-Zehnder interferometer based on concatenating two single-mode fiber tapers," IEEE Photonics Technology Letter, Volume 20, no. 8, 2008, Pages 626-628
147. P. Lu, L. Men, K. Sooley, and Q. Chen, "Tapered fiber Mach-Zehnder interferometer for simultaneous measurement of refractive index and temperature," Appl. Phys. Lett., Volume 94, no. 13, 2009, 131110-1 – 131110-3
148. X. Dong, L. Su, P. Shum, Y. Chung, and C. C. Chan, "Wavelength-selective all-fiber filter based on a single long-period fiber grating and a misaligned splicing point," Opt. Commun., Volume 258, no. 2, 2006, 159-163.

149. P. Lu and Q. Chen, "Femtosecond laser microfabricated fiber Mach–Zehnder interferometer for sensing applications," Opt. Lett., Volume 36, no. 2, 2011, Pages 268-270.
150. Q. Kieu and M. Mansuripur, "Biconical fiber taper sensors," IEEE Photonics Technology Letter, Volume 18, no. 21, 2006, Pages 2239-2241
151. Y. Li, L. Chen; E. Harris, and X. Bao, "Double-pass in-line fiber taper Mach–Zehnder interferometer sensor," IEEE Photonics Technology Letter, Volume 22, no. 23, 2010, Pages 1750-1752,
152. D. Wu, T. Zhu, M. Deng, D.-W. Duan, L.-L. Shi, J. Yao, and Y.-J. Rao, "Refractive index sensing based on Mach–Zehnder interferometer formed by three cascaded single-mode fiber tapers," Applied Optics., Volume 50, no. 11, 2011, Pages 1548-1553,
153. B. Ha, " Interferometric fiber optic sensors", Sensors, 12, 2012, Pages 2467-2486,
154. R. Passy, A. L. Gama, N. Gisin, and J. P. von der Weid, "Pressure dependence of polarization mode dispersion in HiBi fiber," Journal of Lightwave Technology., Volume 10, 1992, Pages 1527–1531.
155. W. J. Bock and T. A. Eftimov, "Simultaneous hydrostic pressure and temperature measurement employing an LP_{01}-LP_{11} fiber-optic polarization-sensitive intermodal interferometer," IEEE Trans. Instrum. Meas., Volume 43, 1994, Pages 337–340
156. C.K Kirkendall and A Dandridge, "Overview of high performance fibre-optic sensing", J. Phys. D: Appl. Phys. Volume 37, 2004, pages 3727-3737
157. M.J Marrone, A.D. Kersey, C.A. Villarruel, C.K. Kirkendall and A. Dandridge, "Elimination of coherent Rayleigh backscatter induced noise in fiber Michelson interferometers", Electronics Letter. Volume 28, 1992, Pages 1803–1804,
158. B.H. Lee, Y. H. Kim, K. S. Park, J. B. Eom, M.J. Kim, B. S. Rho and H. Y. Choi, "Interferometric Fiber Optic Sensors ", Sensors, Volume 12, 2012, Pages 2467-2486.
159. J. Gan, L. Shen, Q. Ye, Z. Pan, H. Cai and R. Qu, "Orientation-free pressure sensor based on π-shifted single-mode-fiber Sagnac interferometer", Applied Optics, Volume 49, No. 27, 2010, pages 5043-5048
160. B. Culshaw, and A. Kersey, "Fiber-Optic sensing: A historical perspective ", Journal of Lightwave Technology, Volume 26, NO. 9, 2008, pages 1064-1078

161. O. Frazão, J. M. Baptista, and J. L. Santos, " Temperature-Independent Strain Sensor Based on a Hi-Bi Photonic Crystal Fiber Loop Mirror, IEEE Sensors Journal, Volume 7, No. 10, 2007, pages 1453-1455
162. O. Frazão, J. M. Baptista and J. L. Santos, "Recent Advances in High-Birefringence Fiber Loop Mirror Sensors", Sensors 2007, 7(11), Pages 2970-2983
163. H.Y. Fu, H.Y. Tam, L.Y. Shao, X. Dong, P.K.A. Wai, C. Lu and S.K. Khijwania, "Pressure sensor realized with polarization-maintaining photonic crystal fiber-based Sagnac interferometer", Applied Optics, Volume 47, Issue 15, 2008, pages 2835-2839
164. C. Zhonga, C. Shena, Y. Youb, J. Chua, X. Zoua, X. Donga, Y. Jina and J. Wanga, "A polarization-maintaining fiber loop mirror based sensor for liquid refractive index absolute measurement" Sensors and Actuators B 168, 2012, Pages 360–364,
165. D. Chen, "Highly birefringent four-hole fiber for pressure sensing", Progress In Electromagnetics Research, Volume 114, 2011, Pages 145–158,
166. J. Gan, H. Cai, and J. Geng, Z. Q. Pan, P. Qu and Z. Fang, "Optic fiber-based dynamic pressure sensor", Optical Fiber Sensors Conference, APOS '08. 1st Asia-Pacific, 2008
167. H. Liang, Y. Jin, Y. Zhao and J. Wang, "Twist sensor by using a pressure-induced birefringence single mode fiber based Sagnac Interferometer", Proc. of SPIE-OSA-IEEE Asia Communications and Photonics, Volume 8311, 2011
168. D.S. Moon, A.K. Lin, G. Sun, T.G. Han, W.T. Han, Y. Chung, "The temperature sensitivity of Sagnac loop interferometer based on polarization maintaining side-hole fiber". Opt. Express, Volume 15, 2007, Pages 7962-7967,
169. G. Kim, T. Cho, K. Hwang, K. Lee, K. S. Lee, Y.G. Han and S.B. Lee, "Strain and temperature sensitivities of an elliptical hollow-core photonic bandgap fiber based on Sagnac interferometer". Opt. Express, Volume 17, 2009, Pages 2481-2486.
170. J.M. Baptista, J.L. Santos, and A.S. Lage, "Self-referenced fibre optic intensity sensor based on a multiple beam Sagnac topology". Opt. Commun., Volume 181, 2000, Pages 287-294.
171. K. Bohnert, P. Gabus, J. Nehring and H. Brandle, "Temperature and vibration insensitive fiber-optic current sensor". Journal of. Lightwave Technology, Volume 20, 2002, Pages 267-276,

172. P. Zu, C.C. Chan, Y. Jin, T. Gong, Y. Zhang, L.H. Chen and X. Dong, "A temperature-insensitive twist sensor by using low-birefringence photonic-crystal-fiber-based sagnac interferometer", IEEE Photonics Technology Letter, Volume 23, 2011, Pages 920-922.
173. B. Dong, J. Hao, C.Y. Liaw and Z. Xu, "Cladding-mode resonance in polarization-maintaining photonic-crystal-fiber-based sagnac interferometer and its application for fiber sensor", Journal of. Lightwave Techology, Volume 29, 2011, Pages 1759-1763,
174. H.M. Kim, T.H. Kim, B. Kim and Y Chung, "Temperature-insensitive torsion sensor with enhanced sensitivity by use of a highly birefringent photonic crystal fiber", IEEE Photonics Technology Letter, 22, 2010, Pages 1539-1541.
175. D.H. Kim and J.U. Kang, "Sagnac loop interferometer based on polarization maintaining photonic crystal fiber with reduced temperature sensitivity", Opt. Express, Volume 12, 2004, Pages 4490-4495
176. Y.J. Rao, "Recent progress in fiber-optic extrinsic Fabry–Perot interferometric sensors", Optical Fiber Technology Volume 12, 2006, Pages 227–23,
177. T. Yoshino, K. Kursawa, K. Itoh, and T. Ose, "Fiber-Optic Fabry-Perot Interferometer and Its Sensor Applications", IEEE Transactions on Microwave Theory and Technologies, Volume MTT-30, No. 10, 1982, pages 1612-1621.
178. I. Padrona, A. T. Fioryb and N. M. Ravindrac, " Novel MEMS Fabry-Perot interferometric pressure sensors", Materials Science Forum Vols. 638-642, 2010, Pages 1009-1014,
179. K.K. Chin, Y. Sun, G. Feng, G. E. Georgiou K. Guo, E. Niver, H. Roman, and K. Noe, "Fabry–Perot diaphragm fiber-optic sensor", Applie Optics Volume 46, No. 31 1 November 2007
180. Y. Sun, G. Feng, G. Georgiou, I. Padron, E. Niver, K. Noe and K.K. Chin, "Fabry-Perot Diaphragm Fiber Optic Sensor (DFOS) for Acoustic Detection", NSTI Nanotech. Santa Clara, May 3-7, 2007
181. J. Han and D. P. Neikirk, "Deflection Behavior of Fabry-Perot Pressure Sensors Having Planar and Corrugated Diaphragms", SPIE's Micromachining and Microfabrication'96 Symposium. Austin, Texas, USA 14-15, 1996, Page 79,
182. S. Prasanna, S. M. Nagraja, P. Pandojirao, and J.C. Chiao, "Modeling and Design of a Fiber Optic Pressure Sensor", Tex MEMS, VII International Conference on MEMS. El Paso Texas, USA and Ciudad Juarez, Mexico, 2005

183. W.J. Wang, R. M. Lin, Y. Ren, T.T. Sun and D.G. Guo, "Fabry-Perot microcavity pressure sensor with a novel single deeply corrugated diaphragm", Microwave and Optical Technology Letters. Volume 39, No. 3, 2003, pages 240-243
184. Y. Zhu, and A. Wang, "Miniature Fiber-Optic Pressure Sensor". IEEE Photonics Technology Letters, Volume 17, No. 2, 2005
185. P.C. Beard, F. Perennes, E. Draguioti and T.N. Mills, "Optical fiber photo acoustic photo thermal probe", Opt. Lett., 23, 1998, Pages 1235-1237,
186. F.L. Pedrotti, L.M. Pedrotti and L.S. Pedrotti, "Introduction to Optics" chapter 9 Pearson International: Upper Saddle River, NJ, USA, 2007.
187. R.V. Neste, C. Belleville, D. Pronovost and A. Proulx "System and method for measuring an optical path difference in a sensing interferometer" US patent #6,842,254 B2, 2005
188. M. Chavko,W.A. Koller, W.K. Prusaczyk and R.M. McCarron "Measurement of blast wave by miniature fiber optic pressure transducer in the rat brain", J. Neurosci. Meth, Volume 159 (2), 2007, Pages 277-281
189. R.A. Bauman, G Ling, L. Tong, A. Januskiewicz, D. Agoston, N. Delanerolle, Y. Kim, D. Ritzel, R. Bell, J. Ecklund, R. Armonda, F. Bandak and S. Parks "An introductory characterization of a combat-casualty-care relevant swine model of closed head injury resulting from exposure to explosive blast", J. Neurotrauma, Volume 26, 2009, Pages 841-860,
190. W.H. Tsai and C.J. Lin, "A novel structure for the intrinsic Fabry-Perot fiber-optic temperature sensor", Journal of Lightwave Technology, Volume 19, 2001, Pages 682-686,
191. S.H. Kim, J.J. Lee, D.C. Lee and I.B. Kwon, "A study on the development of transmission-type extrinsic Fabry-Perot interferometric optical fiber sensor" Journal of Lightwave Technology, Volume 17, 1999, Pages 1869-1874,
192. J.Ran, Y. Rao, J. Zhang, Z. Liu and B. Xu, "A miniature fiber-optic refractive-index sensor based on laser-machined Fabry-Perot interferometer tip" Journal of Lightwave Techology, Volume. 27, 2009, Pages 5426-5429.
193. Y.J. Rao, M. Deng,D.W. Duan, X.C. Yang, T. Zhu and G.H. Cheng, "Micro Fabry-Perot interferometers in silica fibers machined by femtosecond laser", Opt. Express, Volume 15, 2007, Pages 14123-14128,

194. Z.L. Ran, Y.J. Rao, W.J. Liu, X. Liao and K.S. Chiang, "Laser-micromachined Fabry-Perot optical fiber tip sensor for high-resolution temperature-independent measurement of refractive index" Opt. Express, Volume 16, 2008, Pages 2252-2263,
195. T. Wei, Y. Han, H.L. Tsai and H. Xiao, "Miniaturized fiber inline Fabry-Perot interferometer fabricated with a femtosecond laser", Opt. Lett, Volume 33, 2008, Pages 536-538,
196. X. Wan and H.F. Taylor, "Intrinsic fiber Fabry-Perot temperature sensor with fiber Bragg grating mirrors", Opt. Lett, Volume 27, 2002, Pages 1388-1390,
197. Z. Wang, F. Shen, L. Song, X. Wang and A. Wang, "Multiplexed fiber Fabry-Pérot interferometer sensors based on ultrashort Bragg gratings", IEEE Photonics Technology Letter, Volume 19, 2007, Pages 622-624.
198. Y. Zhang, X. Chen, Y. Wang, K.L. Cooper and A. Wang, "Microgap multicavity Fabry-Pérot biosensor", Journal of Lightwave Technology, Volume 25, 2007, Pages 1797-1804,
199. V.R. Machavaram, R.A. Badcock and G.F. Fernando, "Fabrication of intrinsic fibre Fabry-Perot sensors in silica using hydrofluoric acid etching", Sensor Actuator. A, Volume 138, 2007, Pages 248-260.
200. J.R Zhao,X.G. Huang, W.X. He and J.H. Chen "High-resolution and temperature-insensitive fiber optic refractive index sensor based on fresnel reflection modulated by Fabry-Perot interference", Journal of Lightwave Technology, Volume 28, 2799-2803, 2010.
201. P. Morris, A. Hurrell, A. Shaw, E. Zhang and P. Beard, "A Fabry-Perot fiber optic ultrasonic hydrophone for the simultaneous measurement of temperature and acoustic pressure", J. Acoust. Soc. Am, 125, 2009, Pages 3611-3622
202. K.A. Murphy, M.F. Gunther and A.M. Vengsarkar, "Quadrature phase-shifted, extrinsic Fabry-Perot optical fiber sensors", Opt. Lett, Volume 16, Issue 4, 1991, Pages 273-275,
203. A. Méndez, "Fiber Bragg grating sensors: a market overview", Proceedings of SPIE Volume 6619, 2007, Page 661905,
204. K.O. Hill , "Photosensitivity in optical fiber waveguides: Application to reflective Filter Waveguide", Appl. Phys. Lett, Volume 32, 1978, Pages 647-649

205. G. Meltz, W.W. Morey and W.H. Glenn, "Formation of Bragg gratings in optical fiber by transverse holographic method", Opt. Lett. Volume 14 Issue 15, pages 823-825
206. M.G.Xu, L. Reekie, Y. T. Chow and J. P. Dakin, "Optical in-fiber grating high pressure sensor", Electronics Letters, Vol. 29, No. 4, 1993, pages 398-399
207. X. Shu, K. Chisholm, I. Felmeri and K. Sugden, "Highly sensitive transverse load sensing with reversible sampled fiber Bragg gratings", Applied physics Letters, Volume 83, No 15, 2003
208. G. Ming-jin and L. Lei, "A Novel Fiber Bragg Grating Pressure Sensor with the Smart Metal Structure Based on the Planar Diaphragm", Proc. of SPIE Volume 7659, 2010
209. D. Song, Z. Wei, J. Zou, S. Yang, E. Du and H.L. Cui, "Pressure Sensor Based on Fiber Bragg Grating and Carbon Fiber Ribbon-Wound Composite Cylindrical Shell", IEEE Sensors Journal, Volume 9, No. 7, 2009, pages 828-831
210. S.J. Mihailov, "Fiber Bragg Grating Sensors for Harsh Environments", Sensors, Volume 12, 2012, Pages 1898-1918
211. Q. Zhang, N. Liu, T. Fink, H. Li, W. Peng and M. Han, "Fiber-Optic pressure sensor based on π-phase-shifted fiber bragg grating on side-hole fiber", IEEE Photonics Technology Letters, Volume 24, No. 17, 2012, pages 1519-1522
212. Raman, Kashyap, " Fiber Bragg Grating", Academic Press, 1999
213. H. Ahmad, W. Y. Chong, K. Thambiratnam, M. Zamani Z, P. Poopalan, M. M. M. Thant and S. W. Harun, "High sensitivity fiber bragg grating pressure sensor using thin metal diaphragm", IEEE Sensors Journal, Volume 9, No. 12, 2009, pages 1654-1659
214. A. Méndez, "Overview of fiber optic sensors for NDT applications", IV NDT Panamerican Conference, 1-11, 2007.
215. K. Gustafsson and B. Hok, "A fiber optic pressure sensor in silicon based on fluorescence decay", Sensors and Actuators, Volume 19, 1989, Pages 327 – 332,
216. J. A. Dziuban, A. Gorecka-Drzazga and U. Lipowicz, "Silicon optical pressure sensor", Sensorsand Actuators A, Volume 32, 1992, Pages 628-631,
217. I.P. Giles, S. McNeill, and B. Culshaw, "A stable remote intensity based fiber sensor," Journal of physics, 18, 1985, Pages 1124-1126.
218. J.I. Giles and T. Kimura, "Polarization Behavior in Multiply Perturbed Single-Mode Fibers', IEEE Journal of Quantum electronics, Volume QE-18, NO. 1, January 1982, pages 59-65

219. P. V. P. Yupapin, K. Weir, K.T.V. Grattan and A.W. Palme," An optical pressure sensor using a low coherence light source with a highly birefringent fibre", SPIE Volume 1712 14th Symposium on Photonic Measurements, Janos Schanada, Tivadar Lippeni Soporon, Hungary, 1992, pages 160-165
220. M. Karimi, F. Surre, T. Sun, K.T.V. Grattan, W. Margulis and P. Fonjallaz,"Directional force measurement using specialized single-mode polarization-maintaining fibers", Journal of Lightwave Technology, Volume 29, Issue: 24, 2011, Pages 3611 – 3615,
221. W.B. Spillman and D. H. Mc Mahon, "Frustrated-Total-Internal-Reflection Multimode Fiber-optic Hydrophone", Appl. Opt. Volume 19, 1980, pages 1130-1134
222. K. Rahnavardy, V. Arya, A. Wang and J. M. Weiss, "Investigation and application of the frustrated-total-internal-reflection phenomenon in optical fibers", Applied Optics, Volume 36, Issue 10, 1997, Pages 2183-2187,
223. K.K. Sharma, "Optics principle and application", Academic press is an imprint of Elsevier, 2006,
224. P. G. Hura,"Maxwell's Equations", John Wiley & Sons, Inc. 2010
225. A. Rogers, "Polarization in optical fibres", Artech house, inc, 2008, Pages 6-7
226. A. Kumar and A. Ghatak, "Polarization of light with application in optical fibers", Society of photo optical instrumentation engineers (SPIE) press, 2011, page 20.
227. R. W.Waynat and M. N. Ediger, "Electro optic handbook", McGraw Hill, inc, 2000
228. K. Okamoto, "Fundamental of optical waveguides", Academic press is an imprint of Elsevier, 2006,
229. T R. Wolinski, "Polarimetric optical fiber and sensors", Progress in optics, Volume 40, 2000, pages
230. S. P Timoshenko and J. N Goodier, "Theory of elasticity", McGraw-Hill, 1970
231. J.I. Sakai and T. Kimura, "Polarization Behaviour in Multiply Perturbed Single-Mode Fibers", IEEE Journal of Quantum Electronics, 18, No.1, 1982, Pages 59– 65
232. M. Tsubokawa, T. Higashi and Y. Negishi, "Mode couplings due to external forces distributed along a polarization-maintaining fiber: an evaluation", Applied Optics, Volume 27, Issue 1, 1988, Pages 166-173.
233. S. Yin, P.B. Raffin, F.T.S.Yu, "Fiber optic sensors", CRC press, Taylor & Francis Group, 2008, pages 72-74

234. G Rongfeng, Z. Fulong, G. Zhiyin and H. Dexiu, "Stress birefringence analysis of polarization maintaining optical fibers", Optical Fiber Technology 2005, Pages 11 240–254,
235. T. Xu, W. Jing, H. Zhang, K. Liu, D. Jia and Y. Zhang, "Influence of birefringence dispersion on a distributed stress sensor using birefringent optical fiber", Optical Fiber Technology, Volume 15, Issue 1, Pages 83-8, January 2009, pages 83-89
236. W, Pawel, K. Bogdan, "Measurement of transverse force with polarization-maintaining side-hole fibers", Proceedings of SPIE, Volume 5576, Bellingham, WA, 2004
237. Y. Liu, B. Liu, X. Feng, W. Zhang, G. Zhou, S. Yuan, G. Kai and X. Dong, "High-birefringence fiber loop mirrors and their applications as sensors", Applied Optics Volume 44, No. 12, April 2005, pages 2382-2390
238. Y. Yang, J. Li, W. Duan, X.Zhang,W.Jin and M.Yang, "An embedded pressure sensor based on polarization maintaining photonic crystal fibre", Meas. Sci. Technol. Volume 24,No. 9, 2013, Pages 1–6.
239. H. Gong, H. Song, S. Zhang and Y. Jin, Curvature sensor based on hollow-core photonic crystal fibre Sagnac interferometer, IEEE Sensors J, 99, 2013, Pages 1–3.
240. Y. Cui, P.P. Shum, D.J.J. Hu, G. Wang, G. Humbert, X. Dinh, "Temperature sensor by using selectively filled photonic Crystal Fibre Sagnac Interferometer", IEEE Photon. J. 4, 2012, Pages 1801–1808.
241. T. Martynkien, G. Statkiewicz-Barabach, J. Olszewski, J. Wojcik, P. Mergo, T. Geernaert, C. Sonnenfeld, A. Anuszkiewicz, M.K. Szczurowski, K. Tarnowski, M. Makara, K. Skorupski, J. Klimek, K. Poturaj, W. Urbanczyk, T. Nasilowski, F. Berghmans and H. Thienpont, "Highly birefringent microstructure fibres with enhanced sensitivity to hydrostatic pressure", Opt. Express 18, 14,2010, Pages 15113–15121.
242. Zhang, G. Kai, Z. Wang, T. Sun, Y. Liu, J. Liu, W. Zhang, S. Yuan and X. Dong, "Study on polarization properties of birefringent microstructure fibre with lateral pressure", Proc. SPIE 6019 (2005) 60193B.
243. J. Gan, Li Shen, Q. Ye, Z. Pan, H. Cai, and R. Qu, "Orientation-free pressure sensor based on π-shifted single-mode-fiber Sagnac interferometer", Applied Optics, Volume 49, Issue 27, 2010, pages 5043-5048
244. H. M. Kim, T. H. Kim, B. Kim and Y.Chung, "Enhanced transverse force sensitivity by using a highly birefringent photonic crystal fibre with larger air holes on one axis",

Appl. Opt. 49, 20, 2010, Pages 3841–3845.

245. Y. Zhaom, T.T. Song and Q. Wang, "Novel pressure sensor using a Hi-Bi photonic crystal fiber FLM and its demodulation method", Microwave and Optical Technology Letters, Volume 54, Issue 4, 2012, pages 915–917,
246. E. M. Gartner, "Potential improvements in cement sustainability" Proc. 31st Cement Concrete Science Conference, Imperial College London, London, U.K, 2011, p. 13.
247. L. Bertolini, B. Elsener and P. Pedeferri, "Preface," in Corrosion of Steel in Concrete: Prevention, Diagnosis, Repair. Hoboken, NJ, USA: Wiley, 2004, Pages. v–vii.
248. Ø.Vennesl, M. Raupach and C.Andrade, "Recommendation of rilem TC 154-EMC: "Electrochemical techniques for measuring corrosion in concrete", measurements with embedded probes," Mater. Structure, Volume 40, no. 8, 2007, Pages 745–758.
249. C. Andrade, C. Alonso, "Corrosion rate monitoring in the laboratory and on-site," Construction Building Mater, Volume 10, no. 5, 1996, Pages 315–328.
250. H.W.Song and V.Saraswathy, "Corrosion monitoring of reinforced concrete structures—A review," Int. J. Electrochem. Sci, Volume 2, no. 1, 2007, Pages 1– 28,
251. S. Dong, Y. Liao, and Q. Tian, "Intensity-based optical fiber sensor for monitoring corrosion of aluminum alloys," Appl. Opt, Volume 44, no. 27, 2005, Pages 5773–5777
252. M. Benounis, N. Jaffrezic-Renault, "Elaboration of an optical fibre corrosion sensor for aircraft applications," Sensors Actuators B: Chemistry, Volume 100, no. 1–2, 2004, Pages 1–8.
253. Y. Wang and H. Huang, "Optical fiber corrosion sensor based on laser light reflection," Smart Mater. Struct, Volume 20, no. 8, 2011, Pages 085003-1–085003-7,
254. W. Hu, H. Cai and M. Yang "Fe–C-coated fibre Bragg grating sensor for steel corrosion monitoring," Corrosion Science, Volume 53, no. 5, 2011, Pages 1933–1938,
255. K. R. Cooper, J. Elster, M. Jones, and R. G. Kelly, "Optical fiber-based corrosion sensor systems for health monitoring of aging aircraft," in Proc. IEEE Syst. Readiness Technol. Conf, Valley Forge, PA, USA, 2001, Pages 847–856.
256. S.K.A. Kaed, C.C.C. Lam, T. Sun and K. T. V Grattan, "Long period grating pair chloride ion sensor for early corrosion prevention," J. Phys.: Conf. Ser, Volume 85, no. 1, 2007 Pages 012022-1–012022-6
257. X. Zhao, Y. Cui and H. Wei , "Research on corrosion detection for steel reinforced concrete structures using the fiber optical white light interferometer sensing technique,"

Smart Mater. Struct, Volume 22, no. 6, 2013, Pages 065014-1–065014-8

258. R. Abu Hassan, M. H. Abu Bakar and K. Dambul , "Optical-based sensors for monitoring corrosion of reinforcement rebar via an etched cladding Bragg grating," Sens. (Basel), Volume 12, no. 11, 2012, Pages 15820–15826.
259. X. Zhao,P.Gong and G.Qiaoetal, "Brillouin corrosion expansion sensors for steel reinforced concrete structures using a fiber optic coil winding method," Sensors, Volume 11, no. 11, 2011, Pages 10798–10819
260. Z. Zheng, X. Sun and Y.Lei, "Monitoring corrosion of reinforcement in concrete structures via fiber bragg grating sensors," Frontiers Mech. Eng. China, Volume 4, no. 3, 2009, Pages 316–319.
261. S. K. T. Grattan, P. A. M. Basheer, S. E. Taylor,W. Zhao, T Sun and K.T.V. Grattan, "Corrosion induced strain monitoring through fibre optic sensors," J. Phys.: Conf. Series, Volume 85, no. 1, 2007, Pages 012017-1–012017-5
262. S. K.T. Grattan, S.E. Taylor, T. Sun, P.A.M. Basheer, and K.T.V. Grattan, "Monitoring of corrosion in structural reinforcing bars: performance comparison using fiber-optic and electric wire strain gauge systems," IEEE Sensor Journal, Volume 9, no. 11, 20 Pages 1494–1502
263. J. P. Broomfield, "Corrosion of Steel in Concrete," in Corrosion of Steel in Concrete: Understanding, Investigation and Repair. Boca Raton, FL, USA: CRC Press, 2006, Pages 7–9.
264. T. El Maaddawy and K. Soudki, "Effectiveness of impressed current tech- nique to simulate corrosion of steel reinforcement in concrete," J. Mat. Civil Eng, Volume 15, no. 1, 2003, Pages 41–47

Publications

Journal

1. **M. Karimi**, M. Fabian, K. Schuster, P. Mergo, T. Sun, K.T. V. Grattan, "Lateral force sensing system based on different photonic crystal fibres", Sensors and Actuators A 205 (2014) 86–91
2. McCague, M. Fabian, **M Karimi**, M. Bravo, L. R. Jaroszewicz, P. Mergo, T. Sun, and K. T. V. Grattan, " Novel Sensor Design Using Photonic Crystal Fibres for Monitoring the Onset of Corrosion in Reinforced Concrete Structures", JOURNAL OF LIGHTWAVE TECHNOLOGY, VOLUME 32, NO. 5, MARCH 1, 2014
3. **M. Karimi,** T. Sun and K. T. V. Grattan, "Design evaluation of a high birefringence single mode optical fibre-based sensor for pressure monitoring applications", IEEE SENSORS JOURNAL, VOLUME 13, NO. 11, NOVEMBER 2013
4. **M. Karimi,** F. Surre, T. Sun; K.T.V. Grattan, W. Margulis, P. Fonjalla, "Theoretical Analysis of a Non- Symmetric Polarization-Maintaining Single-Mode Fiber for Sensor Applications", Journal of Lightwave Technology, Volume: 30 Issue: 3, 362 – 367, Feb. 1, 2012
5. **M. Karimi**, F. Surre, T. Sun; K.T.V. Grattan, W. Margulis, P. Fonjalla,"Directional force measurement using specialist single mode polarization-maintaining fibres", Journal of Lightwave technology, Volume: 29 Issue: 24, 3611 – 3615, Dec.15, 2011

Conferences

1. T. Sun, C. McCague, M. Fabian, **M. Karimi**, K.T. V. Grattan, "Photonic Crystal Fibres for Monitoring the Onset of Corrosion in Reinforced Concrete Structures", Applied Industrial Optics: Spectroscopy, Imaging and Metrology, June 23-27, 2013
2. McCague, M. Fabian, **M. Karimi**, T. Sun, K.T. V. Grattan, "Novel distributed sensor design for corrosion monitoring using photonic crystal fibers", 6th IEEE/International Conference on Advanced Infocomm Technology (ICAIT), 2013
3. **M. Karimi**, M. Fabian, T.Sun, K.T. V. Grattan, K. Schuster, P. Mergo, "Transverse Force Sensitivity of photonic crystal fibres", IEEE Sensors Conference publications,

10.1109/ICSENS.2012.6411185, Pages: 1- 4, 2012

4. **M. Karimi**, M. Fabian, T.Sun, K.T. V. Grattan, K. Schuster, P. Mergo, "Transverse Force Sensitivity of *joint* photonic crystal fibres", IEEE Sensors Conference publications, 10.1109/ICSENS.2012.6411466, Pages: 1-4, 2012
5. **M. Karimi**, F. Surre, T. Sun; K.T.V. Grattan, P. Fonjalla, "Investigation of single mode polarization- maintaining fibres for directional transverse force measurement", Proc. SPIE 7753, 77535H, May 15, 2011